Simulation of quantum computer hardware based on superconducting circuits

von

Dennis Willsch

Masterarbeit in Physik

vorgelegt der

Fakultät für Mathematik, Informatik und Naturwissenschaften
der RWTH Aachen

im September 2016

angefertigt im

Jülich Supercomputing Center
Forschungszentrum Jülich

bei

Prof. Dr. Kristel Michielsen

Prof. Dr. David P. DiVincenzo

Contents

1. Introduction

Quantum theory is a physical theory with exceptional descriptive power [DKM14]. At the heart of it lie simple algebraic mathematical concepts, commonly referred to as *superposition* and *entanglement*. These concepts are not present in Boolean logic, i.e., the logic that conventional digital computers are based on. For a novel machine called *universal quantum computer* which inherently utilizes these algebraic concepts, however, one can devise algorithms for certain computationally hard problems that can achieve an exponential speedup over the best known algorithms for traditional computers. A significant representative of these algorithms is Shor's factoring algorithm [Sho94], which is one of the most intriguing results in the field of quantum information processing. It is formulated in terms of *quantum gates* that require precise control over the individual degrees of freedom of the underlying computational units, the so-called *qubits*. This scheme is known as *gate model quantum computation*.

Over the last decades, the requirements for a computational device working precisely as this theoretical model predicts have been laid out [DiV00], and tremendous experimental effort has gone into manufacturing such a machine. However, due to the vast variety of microscopic systems that can be successfully described by quantum theory, and the requirement of an immense level of control over the system, a sufficiently large universal quantum computer is still a long way off. So far, only small such devices of less than ten qubits have been built [KBF+15; GCS15].

Fortunately, the small size still allows a deep physical analysis of the specific implementation of quantum computer hardware. When such a study is carried out using the formalism of non-relativistic quantum theory, the state of the system containing the qubits is described by a state vector $|\Psi(t)\rangle$ which is an element of a complex Hilbert space $\mathcal{H}$. Starting from some initial state $|\Psi(0)\rangle$, the time evolution of the system is generated by its Hamiltonian $H(t)$ according to the *time-dependent Schrödinger equation* (TDSE)

$$i\hbar \frac{\partial}{\partial t} |\Psi(t)\rangle = H(t) |\Psi(t)\rangle \quad . \tag{1.1}$$

As the Hamiltonian $H(t)$ is a Hermitian operator on $\mathcal{H}$, the solution to Eq. (1.1) can be expressed in terms of a unitary time evolution operator $U(t, t_0)$ satisfying $|\Psi(t)\rangle = U(t, 0) |\Psi(0)\rangle$. In the context of quantum computation, this operator represents the quantum gate operation that is executed on the system. The specific gate can be designed by tuning external controls such as voltages or magnetic fluxes modelled by $H(t)$. If a sufficiently accurate Hamiltonian is known, all quantum-mechanical properties of the system's evolution can in principle be extracted from Eq. (1.1). Otherwise, one can still describe a reduced part of the system by replacing Eq. (1.1) with the *von Neumann equation*. In addition to this, other effective methods have been devised to describe further incoherent dynamics caused by additional environmental components that are not part of the actual quantum-theoretical description. One of these methods is based on the *Lindblad master equation* [NC11]. However, we are interested in the fundamental quantum-mechanical properties of the system emerging from Eq. (1.1).

To study the TDSE theoretically, one option is to use analytical methods and sophisticated techniques inspired by mathematical statements to extract key features about the system. However, at some points, it is inevitable to make certain approximations or idealizations in order to reveal these features and understand their potential w.r.t. quantum computing.

This is the point where the field of computational physics and computer simulation sets in: By solving the TDSE given by Eq. (1.1) without making *any* further approximations, the full quantum-mechanical nature of the system is accessible. Obviously, due to the huge amount of information contained in the TDSE, such a study is often inspired by previous analytical work. In that sense, computer simulation complements analytical work as a third pillar next to theory and experiments, as it permits a study of the quantum mechanical properties of the systems at a level that is usually inaccessible to experiments. In many fields of engineering and industry, such simulations are done to divulge potential limitations of the system before the actual experimental implementation is carried out, which is obviously also done for financial benefit. Thus, in the context of quantum computing, the advantage of using a computer simulation on the basis of the TDSE is that all sources of fundamental systematic gate errors resulting from necessary simplifications and approximations done in the theory can be individually located, singled out, analyzed, understood, and hopefully eliminated at almost no experimental or monetary cost.

Motivated by this idea, we still have to find a suitable set of fast and unconditionally stable algorithms to actually solve the TDSE. One family of such algorithms is called *product-formula algorithms*, and the mathematical framework to construct them from the form of the Hamiltonian $H(t)$ was presented in 1987 [DeR87]. A major part of this project deals with the analytical derivation of such algorithms and their implementation on a digital computer. To run these algorithms for specific physical setups, we have developed a convenient software application offering a graphical user interface and various visualization options.

The quantum computing systems that we focus on are based on superconducting circuits. This approach to quantum computer hardware is one of the most promising and successful [GCS15; BK15; Rei15]. The key element contained in the underlying superconducting qubits is the *Josephson junction* [Jos62]. Fortunately, for networks of Josephson junctions and other linear circuit elements such as capacitors and inductors, there exists a systematic method of deriving Hamiltonians using electrical network graph theory [BKD04]. This will allow us to find a generic model Hamiltonian $H(t)$ describing an arbitrary number of superconducting qubits and different sorts of couplings. The software package can then be used to analyze potential single-qubit and two-qubit gate schemes, and to test different effective coupling Hamiltonians for superconducting circuits.

In particular, the model Hamiltonian supports implementations of the so-called *transmon qubit* that has become one of the preferred technologies in the superconducting community [Rei15; SMC+16]. It does not suffer from charge fluctuations as much as the former charge qubit [KYG+07], and it can be conveniently controlled by microwave irradiation through its interaction with transmission line resonators. The disadvantage, however, lies in its reduced anharmonicity. Consequently, the presence of higher non-computational states can be detrimental to the qubit dynamics and in turn limit the speed of quantum gates. Therefore, sophisticated pulse-shaping techniques have been developed to improve the speed and the gate fidelity of single-qubit gates [MGR+09;

CDG+10; GMM+11]. It is one of our aims to study the effect of these pulses on the higher levels and to assess how they can be used to speed up high-fidelity single-qubit operations.

To make a qubit system universal for quantum computation, a universal two-qubit gate must be implemented [DiV95] at least between nearest neighbors [DBK+00]. Since the transmon qubits are often operated at fixed frequencies with static linear couplings [CSM+15; GCS15; KBF+15], a two-qubit interaction is needed that does not rely on tuning the individual transmons. The cross-resonance gate is such a two-qubit gate for systems with an untunable transverse coupling that relies only on microwave control of the qubits. Its name is due to the principle that one qubit is driven at the resonance frequency of the other. The idea was initially formulated for capacitively coupled charge qubits [Par06]. A few years later, some deeper theoretical studies were presented [RD10; GAL+12], and the principle has been tested and used in experiments [CCG+11; CGC+12; CGC+13; CGM+14; CMS+15; TCM+16; IBM16] to generate entangling gates such as the CNOT gate. To enhance the speed and the fidelity of the gate, a procedure based on Hamiltonian tomography has recently been introduced [SMC+16], where terms have been measured which were not predicted by the previous perturbative analysis. Such terms are sometimes attributed to classical or environmental effects beyond the time evolution generated by the system's Hamiltonian [CGC+13; War15]. Our aim is to understand to which degree these terms are fundamentally contained in the Hamiltonian of the two-qubit transmon setup, and which effects are due to incoherent dynamics beyond the unitary evolution. Since the system considered in our simulation is, by construction, based purely on the quantum-mechanical time evolution governed by the Schrödinger equation, we apply the same procedure to our system in order to answer this question.

This work is structured as follows: In chapter 2, we review the physical theory of superconducting qubits from a condensed-matter perspective. This includes an inspection of certain apparent mathematical paradoxes concerning the superconducting phase operator, as well as a description of the systematic rules used to construct Hamiltonians from electric circuits. This discussion is followed by applications to some specific circuits and concluded with a brief overview of the current state of the art. In chapter 3, we present the family of model Hamiltonians that our algorithms are based on. The first family models superconducting qubits with various couplings, and the second represents a system of spin qubits that can be seen as an ideal universal quantum computer. Chapter 4 then deals with the derivation of the different algorithms to solve the TDSE. For that purpose, a deep analysis of the analytical properties of our Hamiltonians is required. Subsequently, we give a short description of the visualization methods offered by the program. Finally, we present a new procedure of testing effective Hamiltonians and their effects in the reduced qubit dynamics of the system. In chapter 5, we then apply the computational tools to some proposed and implemented quantum computing systems. The first class is based on charge qubits, where we will specifically address the system forming the basis for the cross-resonance gate. The second class deals with single-qubit gates and two-qubit interactions of transmon qubits coupled via transmission line resonators. For single-qubit gates, we will find cases where certain pulse-shaping techniques can be successfully employed to achieve high-fidelity single-qubit gates. Finally, for two-qubit interactions, we will discover new properties of the driven and undriven transmon-resonator Hamiltonian in the two-level approximation, and thereby also learn about the inherent nature of such effective Hamiltonian approximations.

2. Superconducting qubits

One of the most promising realizations of quantum computer hardware relies on superconducting circuits that contain Josephson junctions as their central elements. Such a Josephson junction consists, in its most fundamental form, of two superconducting materials with a thin insulating barrier in between. In this chapter, we first review these Josephson junctions and present an effective theory to describe superconducting circuits. Next, we present a selection of specific setups used in quantum computer experiments, and finally we briefly look at the current state of the art in superconducting quantum computing.

2.1. Superconductivity and Josephson junctions

As the name suggests, superconducting circuits are based on superconductivity. However, even though this physical effect is crucial for the devices to work, its properties in condensed matter may not seem very evident in the literature on superconducting qubits (see e.g. [WS06; CCE+06; Lan13]). The reason is that usually, once the basic effects of Josephson junctions in superconducting circuits have been introduced, an effective theory in terms of Hamiltonians and simple circuit rules is employed. This theory has proven quite successful in describing experimental realizations and therefore we review it in section 2.2. Before that, however, it is instructive to look at Josephson junctions from a condensed-matter physics point of view to understand why they are so essential in superconducting circuits.

2.1.1. Description in the BCS theory

A very common and fundamental way to describe superconductivity on a microscopic level was presented by Bardeen, Cooper, and Schrieffer (BCS) in 1957 [BCS57]. Until then, the observable effects of superconductivity, such as the infinite conductance and the Meissner-Ochsenfeld effect, were often described by means of a phenomenological theory given by London and London in 1935 [LL35]. The big accomplishment of BCS was to derive these effects from a microscopic model of an interacting electron system on a lattice. They showed that the presence of an attractive interaction (mediated by phonons) between the negatively charged electrons can induce a second-order phase transition at a critical temperature. This so-called Cooper instability causes the electrons to effectively form Cooper pairs, i.e., bosonic pairs with an integer spin. These can then condense into the same single-particle ground states without violating the Pauli principle.

Note that these Cooper pairs actually only exist on very short time scales and are delocalized in position space. Furthermore, this picture of Bose-Einstein condensation differs somewhat from the original picture by BCS. Nevertheless, it serves our purpose to think of the actual charge carriers as effective particles made from two electrons, thus carrying a charge of twice the elementary charge.

The BCS ground state, which is basically the ansatz for a variational method, can be written as

$$|\varphi\rangle = \prod_{\vec{k}} \left(u_{\vec{k}} + e^{i\varphi} v_{\vec{k}} c^{\dagger}_{\vec{k}\uparrow} c^{\dagger}_{-\vec{k}\downarrow} \right) |0\rangle \quad . \tag{2.1}$$

Here, $|0\rangle$ denotes the vacuum state and the fermionic operators $c^{\dagger}_{\vec{k}\uparrow}$ ($c^{\dagger}_{-\vec{k}\downarrow}$) denote the creation of an electron with momentum $\vec{k}$ ($-\vec{k}$) and spin up (down). The coefficients $u_{\vec{k}}$ and $v_{\vec{k}}$ are real parameters for the variational method; their explicit form is not important for our purpose. What is all the more important, however, is the occurrence of a single collective phase φ that is attached to all electron pairs created in the state $|\varphi\rangle$. Although the phase can be gauged away in isolated superconductors by a global transformation of the fermionic operators, it exhibits crucial dynamics when two superconductors are put close to each other. Josephson studied a system of two such superconductors with a tunnel coupling V_T between them [Jos62]. If the two superconductors are initially prepared in the ground state from Eq. (2.1), the joint state of the system can be written as [Str04]

$$|\varphi_1, \varphi_2\rangle = \prod_{\vec{k}} \left(u_{1,\vec{k}} + e^{i\varphi_1} v_{1,\vec{k}} c^{\dagger}_{\vec{k}\uparrow} c^{\dagger}_{-\vec{k}\downarrow} \right) \otimes \left(u_{2,\vec{k}} + e^{i\varphi_2} v_{2,\vec{k}} c^{\dagger}_{\vec{k}\uparrow} c^{\dagger}_{-\vec{k}\downarrow} \right) |0\rangle \quad . \tag{2.2}$$

For these states, the global transformation of the electron operators removing the phase in Eq. (2.1) would still leave the phase difference $\varphi = \varphi_2 - \varphi_1$. This is the reason why the phase variable is so important for superconducting tunnel junctions. Therefore, we define a set of states spanning the degenerate BCS ground state manifold through

$$|\varphi\rangle := |-\tfrac{\varphi}{2}, \tfrac{\varphi}{2}\rangle \,, \quad \varphi \in [0, 2\pi) \quad , \tag{2.3}$$

together with a quantum phase operator

$$\hat{\varphi} = \int_0^{2\pi} d\varphi \, |\varphi\rangle \, \varphi \, \langle\varphi| \quad . \tag{2.4}$$

As long as the superconductors stay in the ground state manifold with a macroscopic number of Cooper pairs (i.e. the characteristic energy scales are smaller than the Bogoliubov-quasiparticle excitation energies needed to break a Cooper pair), these states are sufficient to describe the dynamics of the system. The coupling energy due to the tunnel coupling V_T then amounts to [Str04]

$$\langle\varphi|V_T|\varphi\rangle = -E_J \cos\varphi \quad . \tag{2.5}$$

The prefactor represents the strength of the tunnel coupling and is called the Josephson energy $E_J \propto \Delta^2$, where Δ is the superconducting energy gap.

Taking the formalism a bit further (see [WS65] or [Jos74]; see also the derivation based on Hamiltonian dynamics in appendix A), one can deduce two very interesting effects for the voltage V and the current I across a Josephson junction. These are the so-called AC and DC Josephson effects and have so stunning implications that they have caused quite some skepticism in the 1960s until they were measured experimentally. The basic

equations are

$$I = I_c \sin\varphi \qquad \text{(DC Josephson effect)} \tag{2.6}$$

$$V = \frac{\hbar}{2e}\dot{\varphi} \qquad \text{(AC Josephson effect)} \quad , \tag{2.7}$$

where $I_c = 2eE_J/\hbar$ is the critical current. Here, e denotes the electron charge and $\hbar$ is the reduced Planck constant. Equation (2.6) implies that a mere phase difference between the two superconductors causes a tunnel current through the insulator. This *direct current* is carried by Cooper pairs (i.e. pairs of electrons) that tunnel coherently between the superconductors and is therefore called a *supercurrent*. What is remarkable is that the current occurs without the presence of an external electromagnetic field, thus being completely dissipationless. The second effect described by Eq. (2.7) implies that a constant voltage across the junction causes a constant slope for the phase difference φ. In conjunction with Eq. (2.6), this results in an *alternating current* oscillating at a fixed frequency proportional to the voltage. In that sense, a Josephson junction acts as a perfect voltage-to-frequency converter. Apart from that, the second effect also indicates another way of interacting with superconducting circuits and, in particular, the phase: Consider a closed superconducting loop with a Josephson junction and a magnetic flux Φ_{ex} piercing the loop. Then Faraday's law of induction tells us that a change $\dot{\Phi}_{ex}$ induces a voltage across the junction which can, through Eq. (2.7), directly affect the phase φ. Thus external voltages and magnetic fields are the crucial quantities that we will use to interact with superconducting circuits from outside.

For the role that superconducting tunnel junctions usually play in applications of quantum computing, one often employs a description in terms of an effective Hamiltonian that exposes the property of a Josephson junction as a storage box for Cooper pairs. This description will be briefly summarized and discussed in the following.

2.1.2. Effective Hamiltonian for a Josephson junction

The Josephson energy E_J in Eq. (2.5) is one of two characteristic energy scales for a Josephson junction. The other characteristic energy stems from the fact that there is not only a tunnel coupling, but also an electrostatic interaction between the two superconductors. With C denoting the capacitance of the superconductor-insulator-superconductor geometry, the scale of this electrostatic interaction is given by the so-called charging energy

$$E_C = \frac{(2e)^2}{2C} \quad . \tag{2.8}$$

It physically represents the energy needed to charge the capacitor with an additional Cooper pair having a charge $2e$. In terms of the difference $n = n_2 - n_1$ in the number of Cooper pairs on both sides of the insulator, the electrostatic interaction energy is then given by $E_C n^2$.

With the two energies representing the characteristic energy scales of Josephson junctions, standard quantum theory tells us that we should now be able to derive the system's dynamics by considering a Hamiltonian of the form

$$H_{\mathrm{JJ}} = E_C \hat{n}^2 - E_J \cos\hat{\varphi} \quad . \tag{2.9}$$

Thereby, the number operator $\hat{n} = \sum_n n\,|n\rangle\langle n|$ is defined through its eigenstates

$$|n\rangle := \frac{1}{2\pi}\int_0^{2\pi} d\varphi\, e^{-in\varphi}\,|\varphi\rangle \quad . \tag{2.10}$$

This definition via the Fourier transform can be physically understood by examining its effect on the BCS ground state $|\varphi\rangle$ in Eq. (2.1): Expanding the product, we see that for every Cooper pair created by $c^\dagger_{\vec{k}\uparrow} c^\dagger_{-\vec{k}\downarrow}$, the phase is increased by $e^{i\varphi}$. Due to the orthogonality of $e^{-in\varphi}$, the integration in Eq. (2.10) then kills all terms with a phase different from $n\varphi$. Thus only states with a number of n Cooper pairs survive the integration and contribute to $|n\rangle$.

For now, we follow the usual course found in the literature (cf. [WS06], [Che07], and [Lan13]) which is to simply declare $\hat{n}$ and $\hat{\varphi}$ as conjugate variables. This implies that both are *Hermitian operators* and *Fourier transform duals* of one another, i.e.

$$\hat{n} \underset{\{|\varphi\rangle\}}{\overset{\bullet}{=}} i\frac{\partial}{\partial\varphi} \qquad \text{and} \qquad [\hat{n}, \hat{\varphi}] = i \quad . \tag{2.11}$$

If we just take this as a given rule for Eq. (2.9), the TDSE for a state

$$|\psi(t)\rangle := \int_0^{2\pi} d\varphi\, \psi(\varphi, t)\,|\varphi\rangle \tag{2.12}$$

reads

$$i\hbar\frac{\partial}{\partial t}\psi(\varphi,t) = -E_C\frac{\partial^2}{\partial\varphi^2}\psi(\varphi,t) - E_J\cos\varphi\,\psi(\varphi,t) \quad . \tag{2.13}$$

Thus the evolution of the phase difference across a Josephson junction is governed by a wave function $\psi(\varphi, t)$. Strong support for this step lies in the fact that the implied phenomena have been verified in experiments, frequently going under the name of "Macroscopic Quantum Phenomena" [Cal14].

Another argument for just taking $\hat{n}$ and $\hat{\varphi}$ as conjugate variables is the intuitive representation of the Hamiltonian Eq. (2.9) in the eigenbasis $\{|n\rangle\}$ of the number operator: Using the inverse relation to Eq. (2.10)

$$|\varphi\rangle = \sum_{n=-\infty}^{\infty} e^{in\varphi}\,|n\rangle \quad , \tag{2.14}$$

we find

$$\begin{aligned} e^{i\hat{\varphi}} |n\rangle &= \frac{1}{2\pi} \int_0^{2\pi} d\varphi \, |\varphi\rangle \, e^{i\varphi} \, \langle\varphi|n\rangle \\ &= \frac{1}{2\pi} \int_0^{2\pi} d\varphi \, e^{-i(n-1)\varphi} \, |\varphi\rangle \\ &= |n-1\rangle \quad . \end{aligned} \tag{2.15}$$

The Josephson junction Hamiltonian Eq. (2.9) can thus be written as

$$\begin{aligned} H_{\mathrm{JJ}} &= E_C \hat{n}^2 - E_J \frac{e^{i\hat{\varphi}} + e^{-i\hat{\varphi}}}{2} \\ &= \sum_{n=-\infty}^{\infty} E_C n^2 \, |n\rangle\langle n| - \sum_{n=-\infty}^{\infty} \frac{E_J}{2} \left(|n\rangle\langle n+1| + |n+1\rangle\langle n| \right) \quad . \end{aligned} \tag{2.16}$$

Hence the cosine term immediately induces Cooper pairs tunneling one by one back and forth through the junction, which agrees with the intuitive picture of a Josephson junction from the previous subsection.

2.1.3. A note on apparent paradoxes

Irrespective of how good the previous formalism including the rule of declaring $\hat{n}$ and $\hat{\varphi}$ as conjugate variables may appear, there are some difficulties that arise upon closer inspection. They can be traced back to well-known problems with pairs of conjugate variables, one of which being a periodic operator such as the phase. A collection of some affected cases in quantum mechanics has already been discussed in [CN68], with a few first suggestions on how to resolve the problems. Furthermore, a compilation of many historic and modern papers on the quantum phase problem and its solution can be found in the book by Barnett and Vaccaro [BV07]. In the following, we state the problems applying to our discussion and describe a possible solution to them.

(I) The first problem lies in the definition of the number states in Eq. (2.10). We argued that the integration kills all terms in Eq. (2.1) that do not have exactly n Cooper pairs. So n must be a non-negative integer. In the inverse relation given by Eq. (2.14), however, we naturally let n range from $-\infty$ to ∞. If we only started at $n = 0$ instead (such that $\hat{n}$ was bounded from below), the inverse Fourier transform would not work. Furthermore, the phase operator that is actually Hermitian from its definition in Eq. (2.4), would generate a *nonunitary* operator $U = e^{i\hat{\varphi}}$ since $U|0\rangle = 0$, as shown in [CN68] and [Str04]. How can we solve this inconsistency?

A physical argument is given in [Lan13], saying there is always a positive background charge due to the $\mathcal{O}(10^{23})$ nuclei of the materials. Then $n = 0$ only represents the state in which the number of Cooper pairs exactly compensates this background such that the net charge condition is neutral. So we could include negative n as a convention and approximate the lower bound by $-\infty$. However, this reasoning still leaves the mathematical part of our argument below Eq. (2.10) invalid. It can be corrected, though, by recalling that we actually treat a Josephson junction consisting of *two* superconducting reservoirs.

Thus the correct definition of $|n\rangle$ in Eq. (2.10) would need to be based on the states $|\varphi\rangle$ from Eq. (2.3), where φ refers to the phase difference across the junction. For a term in Eq. (2.2) where n_1 Cooper pairs are created in the first and n_2 in the second part of the product, the complex phase factor is then given by $e^{-in_1\varphi/2}e^{in_2\varphi/2} = e^{i(n_2-n_1)\varphi/2}$. So the integration keeps only states with a phase $e^{in\varphi}$ where $n = (n_2 - n_1)/2$ is the *relative number difference* between the superconductors, which can obviously be negative as well. Approximating the large total number of Cooper pairs $N = n_1 + n_2$ by ∞ eventually solves the problem.

(II) The second problem lies in the commutation relation given in Eq. (2.11), together with the assumption that both operators are self-adjoint on the entire Hilbert space. Using the proper representation following from Eq. (2.14)

$$\hat{n} = \int_0^{2\pi} d\varphi\, |\varphi\rangle\, i\frac{\partial}{\partial\varphi}\, \langle\varphi| \underset{\{|\varphi\rangle\}}{\bullet} i\frac{\partial}{\partial\varphi} \quad , \tag{2.17}$$

we can verify the commutation relation in the space span$\{|\varphi\rangle\}$:

$$[\hat{n}, \hat{\varphi}] \underset{\{|\varphi\rangle\}}{\bullet} \left[i\frac{\partial}{\partial\varphi}, \varphi\right] = i\left(\frac{\partial}{\partial\varphi}(\varphi\,\cdot) - \varphi\frac{\partial}{\partial\varphi}\right) = i \quad . \tag{2.18}$$

In principle, as the commutator is independent of the basis, this should hold in general. However, an evaluation of the commutator in the number states $\{|n\rangle\}$ yields

$$\langle n|(\hat{n}\hat{\varphi} - \hat{\varphi}\hat{n})|n\rangle = (n-n)\underbrace{\langle n|\hat{\varphi}|n\rangle}_{\in[0,2\pi) \text{ due to the bounded spectrum of } \hat{\varphi}} = 0 \neq i \quad . \tag{2.19}$$

There have been some suggestions in the literature on how to solve this apparent contradiction. In [CN68], it is argued that the phase operator is itself not an appropriate operator and must be replaced by periodic extensions $\sin\hat{\varphi}$ and $\cos\hat{\varphi}$. Loss and Mullen reasoned in [LM92] that this replacement (albeit possible) is not necessarily a convenient solution, as physicists are usually interested in commutation relations of conjugate variables. Therefore, they avoid the issue by defining an inner product in φ-space and compute matrix elements only through this definition. Then the calculation of $\langle n|[\hat{n}, \hat{\varphi}]|n\rangle$ effectively uses the same steps as in Eq. (2.18) and thus produces the same result. However, by restricting ourselves to this fixed definition for any inner product, we lose the mathematical convenience associated with Dirac's notation, namely that we work on an abstract Hilbert space and can evaluate inner products in any representation by inserting completeness relations $\mathbb{1} = \sum_n |n\rangle\langle n| = \int d\varphi\, |\varphi\rangle\langle\varphi|$.

So the bottom-line question is, can we find a mathematically satisfying explanation why this problem arises at all? It turns out that we can, if we look more carefully at the domains of the operators we use. As rigorously demonstrated in the book by Gustafson and Sigal [GS03], such domain considerations should always be done when working with infinite-dimensional Hilbert spaces, without just blindly abusing the simplicity of Dirac's notation. Otherwise, similar problems can be constructed with the standard position and momentum operators $\hat{x}$ and $\hat{p}$ (see [Gie00]). Therefore, let us take a closer look at the domain of the operator $[\hat{n}, \hat{\varphi}]$. As shown in appendix B, the operator $\hat{\varphi}$ is self-adjoint, bounded, and perfectly well-defined. The unbounded operator $\hat{n}$, however, is

only well-defined and self-adjoint on states $|\psi\rangle$ with a wave function $\psi(\varphi) = \langle\varphi|\psi\rangle$ that satisfies $\psi(0) = \psi(2\pi)$ (together with ψ' being square-integrable), so there is already some restriction. For the operator $[\hat{n}, \hat{\varphi}]$, the proper domain is (see appendix B)

$$\mathcal{D}([\hat{n}, \hat{\varphi}]) = \left\{|\psi\rangle \,:\, \psi, \psi' \in L^2([0, 2\pi]) \text{ and } \psi(0) = \psi(2\pi) = 0\right\} \quad . \tag{2.20}$$

Now the number states $|n\rangle$ have a wave function $n(\varphi) = \langle\varphi|n\rangle = e^{-in\varphi}/2\pi$ (see Eq. (2.10)). This function does obviously not satisfy $n(0) = n(2\pi) = 0$, so it is not inside the domain of $[\hat{n}, \hat{\varphi}]$. Thus it makes mathematically no sense to apply this operator on $|n\rangle$, let alone evaluate matrix elements w.r.t. $|n\rangle$. So it is no surprise that we can tune the calculation in Eq. (2.19) to produce any value such as $\pm i$ or 0. However, if we adhere to the proper domain of the operator, we will always arrive at $[\hat{n}, \hat{\varphi}] = i$ without any contradiction at all.

2.1.4. Alternative models

It should be noted that there have also been alternative models to describe a Josephson junction, some with a deeper focus on physical properties and some from a mathematical perspective. They have been nicely summarized in [Str04] and we only mention three complementary models.

(I) A very simple and intuitive view was given by Feynman in chapter 21-9 of [FLS65]. Since a superconductor can be described as a coherent wave of Cooper pairs with one collective phase, he proposed a wave function $\Psi_i = \sqrt{\rho_i} e^{i\varphi_i}$ where ρ_i is the Cooper pair density and φ_i is the phase of each superconductor. Based on a coupling K due to the insulator between both superconductors, and an external voltage V applied across the junction, he wrote down a TDSE

$$i\hbar \frac{\partial \Psi_1}{\partial t} = \frac{eV}{2}\Psi_1 + K\Psi_2 \tag{2.21a}$$

$$i\hbar \frac{\partial \Psi_2}{\partial t} = -\frac{eV}{2}\Psi_2 + K\Psi_1 \quad . \tag{2.21b}$$

Remarkably, this simple model can already correctly describe the most interesting physical effects about Josephson junctions, namely the DC and the AC Josephson effects given in Eq. (2.6) and Eq. (2.7).

Using the framework of quantum theory, this derivation of the Josephson effects is obviously based on the standard postulates of quantum mechanics. Due to the simplicity of Eqs. (2.21a) and (2.21b), it might be an interesting task to overcome the remaining assumptions by applying the principles of logical inference [DKM14; DKM16]. These principles have already been proven capable of deriving equations for quantum mechanical key experiments [DKD+15a], the Pauli equation [DKD+15b], and the Klein-Gordon equation [DKR+16] by only using observations from robust experiments and plausible reasoning.

(II) Another effective model inspired by the bosonic character of Cooper pairs in superconducting wires has been presented in [ADS01]. In their work, they start from a

two-mode boson Hamiltonian

$$H = \frac{E_C}{4}\left(a_1^\dagger a_1 - a_2^\dagger a_2\right)^2 - \frac{E_J}{N}\left(a_1^\dagger a_2 + a_2^\dagger a_1\right) \quad , \tag{2.22}$$

where $a_i^\dagger$ creates a Cooper pair on side i of the Josephson junction. The first term counts the relative number of Cooper pairs on both sides of the insulator and thus models the charging energy of the capacitor. The second term is responsible for Cooper pairs tunneling through the junction and thus represents the tunnel coupling. In that sense, the model already resembles the Hamiltonian in Eq. (2.9). Compared to other bosonic systems such as Bose-Einstein condensates, the only odd factor seems to be the $1/N$ in front of the coupling term. A physical reason for it lies in the fermionic character of the two electrons forming the Cooper pair: They have to be put into unoccupied states on the other side of the insulator, so there is no bosonic enhancement of the coupling.

A nice property of the model is that it is set in a finite-dimensional Hilbert space and thus does not suffer from the mathematical difficulties presented earlier. Additionally, even though the number states seem more fundamental to start with in this model, the quantum aspect of the phase difference φ across the junction enters naturally when the formalism is carried on (see [Str04]). Moreover, eventually taking the limit $N \to \infty$ correctly reproduces the TDSE in Eq. (2.13).

(III) Finally, there is a path-integral method to derive the dynamics of the phase of a Josephson junction presented in [AES82; ESA84]. In their work, the authors use a functional-integral formulation to treat Josephson junctions from a microscopic perspective. The method is perhaps more fundamental, in the sense that they derive the equations describing the BCS treatment presented above as an approximation. The model is quite elegant from a field-theoretic point of view, and it also takes into account dissipative effects through quasiparticle tunneling that our description has excluded.

2.2. Circuit quantization

To construct superconducting qubits, one needs to incorporate the central nonlinear elements, the Josephson junctions, into electric circuits. These can be quite complicated and difficult to handle from the condensed-matter perspective outlined in the previous section. Fortunately, there exists a quite effective procedure to handle complex circuits, which does not necessarily rely on superconducting elements. It is probably the most economical way to address the problem.

In short, the procedure uses the Lagrangian formalism from analytical mechanics to derive Hamilton functions representing the complete circuit. After some generic quantization step reminiscent of the canonical quantization of classical mechanics, one obtains a Hamiltonian describing the dynamics of the quantum device like the Hamiltonian we derived in Eq. (2.9).

2.2.1. Lagrangian and Hamiltonian description of electric circuits

An electric circuit is, in principle, an arbitrary network of electric elements such as capacitors, inductors and resistors. They can be coupled to external voltage sources, current sources, or magnetic fluxes in order to control and interact with them. A standard way

to derive the dynamics of such a circuit is to identify all nodes and branches, write down Kirchhoff's laws for the currents and voltages, eliminate all superfluous degrees of freedom, and solve the system of coupled differential equations. Although this procedure works, it can result in complicated sets of equations that are not easy to handle.

A more systematic way to derive the dynamics lies in a step similar to the transition from Newtonian to Lagrangian mechanics: In the case of dissipationless electric components (like ideal capacitors, inductors, and Josephson junctions), it can be shown that the equations of motion derived from Kirchhoff's laws are equivalent to Euler-Lagrange equations for a certain Lagrangian. To derive this Lagrangian from the circuit, there exists a methodical procedure based on electrical network graph theory [Dev97] that we will review shortly. Note that it is also possible to describe dissipative circuit elements and study relaxation and decoherence for superconducting qubits within this formalism [BKD04].

Once the Lagrangian of the circuit has been written down, an equivalent Hamiltonian description can be obtained by performing a Legendre transformation. The Hamilton function also paves the way to quantize the circuit. In that step, the question might arise under which circumstances such a quantum description is necessary, and when it is still sufficient to stick to the classical equations of motion. For a simple LC-circuit, for instance, the proper indicator is the ratio of the circuit's resonance wavelength and its geometric size: Consider a circuit with a large capacitance and a large inductance such that $\omega/2\pi = 1/(2\pi\sqrt{LC}) \sim 1\,\mathrm{GHz}$, so it has a characteristic wavelength of $\lambda \sim 0.1\,\mathrm{m}$. If its physical size is on the order of $100\,\mu\mathrm{m} \ll \lambda$, it can already behave as a quantum harmonic oscillator with only one macroscopic collective degree of freedom [Dev97]. In that sense, the LC-circuit provides a reservoir for electromagnetic excitations (photons) of the same kind as standard cavities in quantum optics experiments, and the quantization step is formally equivalent to the quantization of a single-mode electromagnetic field (see [GK05]).

We now review the procedure of obtaining the Lagrangian and Hamiltonian description of the circuit based on the presentation in [Bis10] and [BKD04]; many examples and proper derivations can also be found in [Sur15].

(I) The first step is to represent the circuit diagram as a directed graph. All circuit elements are represented as branches b, and connections between them become nodes n. Subsequently, a spanning tree (i.e. a loop-free version of the graph including all nodes) has to be chosen. This spanning tree effectively divides all branches into *tree branches* that are part of the spanning tree, and *closure branches* connecting two nodes of the spanning tree without being part of the tree itself. A closure branch thus closes a loop $l(b)$ that has been broken by the choice of the spanning tree.

One arbitrary node is chosen as *ground*. Every other node is called *active node* and is assigned a flux variable Φ_n, defined as the time integral of the voltages along the unique path over all tree branches b from this node to ground, i.e.

$$\Phi_n(t) := \sum_b S_{nb} \int_{-\infty}^{t} V_b(t')dt' \quad , \tag{2.23}$$

where $S_{nb} = \pm 1$ is a sign representing the direction of the branch in the directed graph. Note that this definition is, in principle, an expression of Faraday's law of induction. The

Lagrangian $\mathcal{L}$ will then be a function of all fluxes Φ_n and the corresponding voltages $V_n = \dot{\Phi}_n$ associated with each active node n. It is worth mentioning that this choice of flux variables for the Lagrangian description of the circuit is a convention. It has the advantage that the corresponding Hamiltonian naturally becomes a function of the charges (number of Cooper pairs) and fluxes (phases) like the Hamiltonian in Eq. (2.9).

(II) The next step is to construct the Lagrangian $\mathcal{L} = T - U$ from the capacitive energy T and the inductive energy U. For this purpose, each branch $b = n \to n'$ is assigned a branch flux

$$\Phi_b = \begin{cases} \Phi_{n'} - \Phi_n & (\text{if } b \text{ is a } \textit{tree branch}) \\ \Phi_{n'} - \Phi_n \pm \Phi^{ex}_{l(b)} & (\text{if } b \text{ is a } \textit{closure branch} \text{ closing the loop } l(b)) \end{cases} . \tag{2.24}$$

For closure branches, $\Phi^{ex}_{l(b)}$ is the external magnetic flux piercing the loop $l(b)$. Its sign has to be chosen according to the right-hand rule. In our case, we have to distinguish between three different kinds of branches, each producing a different term in either T or U:

(a) If the branch is a capacitor of capacitance C, add its capacitive energy $\frac{C\dot{\Phi}_b^2}{2}$ to T.

(b) If the branch is an inductor of inductance L, add its inductive energy $\frac{\Phi_b^2}{2L}$ to U.

(c) If the branch is a Josephson junction characterized by its Josephson energy E_J, add its inductive energy $-E_J \cos\varphi_b$ with $\varphi_b = \frac{2e}{\hbar}\Phi_b$ to U.

Note that a bare Josephson junction explicitly belongs to the class of inductive branches since they can be seen as inductors with a nonlinear dependence of I on Φ (see Eq. (2.6)). Also, the capacitive part of a Josephson junction characterized by its charging energy in Eq. (2.8) has to be treated as a capacitive branch according to (a).

(III) The next step is the Legendre transformation to obtain the Hamiltonian description of the circuit. We define the canonical momentum for each node as

$$Q_n := \frac{\partial \mathcal{L}}{\partial \dot{\Phi}_n} . \tag{2.25}$$

It physically represents the charge accumulating in the node. This system of equations has to be solved for $\dot{\Phi}_n$. Then we perform the Legendre transformation

$$H := \sum_n Q_n \dot{\Phi}_n - \mathcal{L} \tag{2.26}$$

to obtain the Hamilton function of the circuit as a function of all charges and fluxes associated with each node.

(IV) The last step is given by the quantization procedure. Since we have superconducting circuits with Josephson junctions and Cooper pairs as charge carriers in mind, we first perform a change of variables $(Q, \Phi) \to (n, \varphi)$ for each node via

$$n := \frac{Q}{2e} \qquad \text{and} \qquad \varphi := \frac{2e}{\hbar}\Phi = \frac{2\pi}{\tilde{\Phi}_0}\Phi_n . \tag{2.27}$$

Here, n denotes the charge in terms of the number of Cooper pairs, φ is the superconducting phase discussed in the previous section, and $\tilde{\Phi}_0 = h/2e$ is the superconducting flux quantum.

The actual quantization step resembles the quantization of position and momentum variables in standard quantum mechanics: We elevate number and phase variables to operators $\hat{n}$ and $\hat{\varphi}$ obeying canonical commutation relations $[\hat{n}, \hat{\varphi}] = i$ as discussed in the previous section. With regard to the discussion in section 2.1.3, this rule should not be seen as a rigorous procedure, but rather as a means of arriving at the proper Hamiltonian dictating the dynamics of the system due to its collective degrees of freedom [Dev97] (see also [Gir11]).

The advantage of this set of rules lies in their systematic nature such that they facilitate a treatment of quite complicated circuits. However, doing it by hand can be rather cumbersome as the Legendre transformation for a large system basically amounts to inverting the symmetric matrix associated with the underlying quadratic form. To simplify the procedure, one can apply the usual parallel and series circuit rules in advance, and collect known parts of the circuit into effective combinations (such as the bare Josephson tunnel junction and its associated capacitor). In doing so, Hamiltonians of different circuit components are often simply added to obtain the full circuit Hamiltonian. It has to be stressed, though, that the proper way to derive a circuit's Hamiltonian is to first construct all terms of the Lagrangian as outlined above, and then properly perform the Legendre transformation. Without doing this, one risks losing information about cross-capacitive terms and their energy scales.

We will now go ahead and apply these rules to a selected set of systems that will be of importance for the remainder of the thesis. They serve as an illustration of the procedure and may prepare for the somewhat more involved example in the following section.

2.2.2. Application to selected systems

Josephson junction

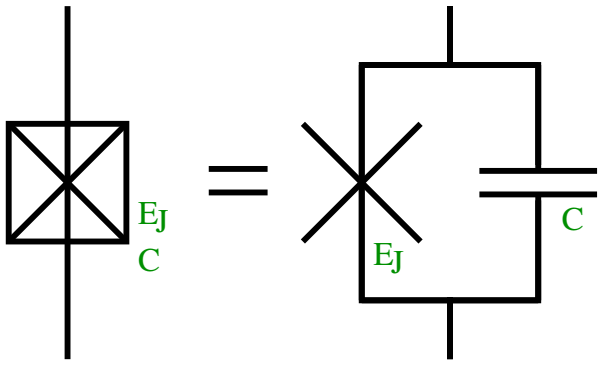

Figure 2.1.: Circuit symbol for a Josephson junction. The capacitive and inductive character of the superconductor-insulator-superconductor geometry have to be treated separately. The first is represented by the standard capacitor symbol, and the bare cross denotes the tunnel junction. Both are combined into one effective circuit symbol given by a crossed box.

The Josephson junction in Fig. 2.1 is modelled as a capacitor C and a tunnel junction characterized by its Josephson energy E_J. In accordance with the recipe presented in the last subsection, we represent the circuit as a two-terminal network graph, see Fig. 2.2. We choose the bottom node as ground, which automatically makes the top node an active

node associated with the flux variable Φ. The spanning tree must be a loop-free version of the graph, so we arbitrarily choose the inductive branch (the blue curve in the figure). This makes the capacitive branch a closure branch. As there is no external flux piercing the loop, both branch fluxes are given by $\pm\Phi$ and their voltages by $\pm\dot{\Phi}$.

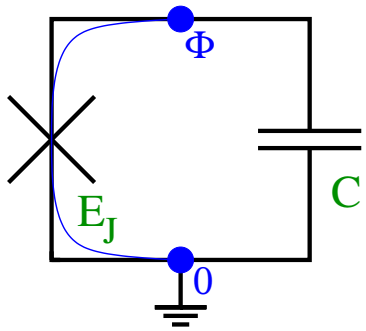

Figure 2.2.: The network graph of the electric circuit of a Josephson junction consists of the ground node 0, the active node Φ, and the spanning tree chosen arbitrarily as the inductive branch. Thus this branch becomes a *tree branch*, and the capacitive branch becomes a *closure branch*.

Since we have two branches in total, we expect the Lagrangian $\mathcal{L} = T - U$ to consist of two terms. The inductive term goes into the potential energy U as $-E_J \cos(2\pi\Phi/\tilde{\Phi}_0)$. Similarly, the capacitive term enters into the kinetic energy T as $C\dot{\Phi}^2/2$. Hence we obtain the Lagrangian

$$\mathcal{L} = \frac{C\dot{\Phi}^2}{2} + E_J \cos\left(\frac{2\pi}{\tilde{\Phi}_0}\Phi\right) \quad . \tag{2.28}$$

For the Legendre transformation, we compute the canonical momentum $Q = \partial\mathcal{L}/\partial\dot{\Phi} = C\dot{\Phi}$ and use this relation to eliminate $\dot{\Phi}$ in Eq. (2.26). After the change of variables according to Eq. (2.27) and the quantization step, we obtain

$$H = \underbrace{\frac{(2e)^2}{2C}}_{E_C}\hat{n}^2 - E_J \cos\hat{\varphi} \quad , \tag{2.29}$$

which is exactly the same expression as the Hamiltonian we derived in Eq. (2.9).

Tunable Josephson junction

A very convenient circuit element, namely a flux-tunable Josephson junction, can be obtained by shunting two Josephson junctions in a superconducting loop pierced by an external magnetic flux Φ_{ex}. Together with an external current bias, this is commonly known as a DC Squid and can be used as a sensitive magnetometer [Che07]. For us, this example serves as a very basic application of the formalism where it is necessary to distinguish between tree branches and closure branches.

The circuit of the system along with a spanning tree is shown in Fig. 2.3. To stress the important aspect of the setup and for the sake of simplicity, we omitted the capacitive parts of the junctions; carrying them through the Legendre transformation is not a big problem, though.

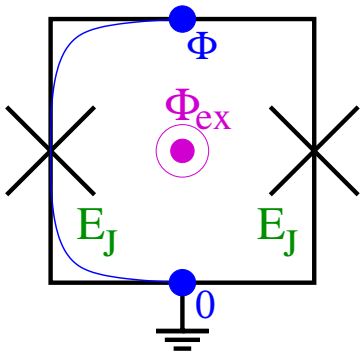

Figure 2.3.: Setup of a superconducting ring with two Josephson junctions and an external magnetic flux Φ_{ex} threading the loop. The spanning tree is chosen as the left inductive branch. Note that there are no boxes around the junctions; the capacitive parts have been omitted for the sake of simplicity.

Since the graph consists of inductive branches only, the Lagrangian does not depend on the voltages $\dot{\Phi}$. Therefore, the Legendre transformation reduces to $H = -\mathcal{L}$ and we can directly construct the Hamiltonian. The only important step now lies in distinguishing between tree and closure branches: The left branch belongs to the spanning tree, so it causes a term $-E_J \cos\varphi$ in the Hamiltonian. The right branch, however, closes the loop that is pierced by the external flux Φ_{ex}, so the branch flux according to the right-hand rule and Eq. (2.24) is $\Phi - 0 + \Phi_{ex}$. Note that this rule immediately enforces conservation of magnetic flux in the loop, without the need to eliminate superfluous degrees of freedom afterwards.

In terms of the reduced flux variable $\phi_{ex} = 2\pi\Phi_{ex}/\tilde{\Phi}_0$, we thus obtain

$$\begin{aligned} H &= -E_J \cos\varphi - E_J \cos(\varphi - \phi_{ex}) \\ &= \underbrace{2E_J \cos\frac{\phi_{ex}}{2}}_{=:E_J(\phi_{ex})} \cos\left(\varphi - \frac{\phi_{ex}}{2}\right) \quad . \end{aligned} \tag{2.30}$$

So the setup behaves as one effective Josephson junction whose Josephson energy $E_J(\phi_{ex})$ is tunable through an external magnetic flux. Note that for a time-independent flux, the phase shift inside the second cosine can be eliminated by a shift of variables.

This effect is very important in experiments since the Josephson energy directly influences the dynamics of the system. Having it tunable from outside thus presents an immediate way to control and interact with the circuit. This can be important for e.g. the realization of gates in applications of quantum computing. Without being explicitly mentioned, the Josephson energy E_J is often considered to be controllable by this very setup.

Voltage source

In many circuits, one way of controlling the system is to apply a certain voltage to some node. To do so, we have to know how the existence of a voltage source is expressed in the present circuit formalism.

An ideal voltage source is a two-terminal device that can maintain a fixed voltage V w.r.t. ground. As such, it can be seen as a large capacitor $C_S \to \infty$ charged with a charge $Q_S \to \infty$ such that $Q_S/C_S \overset{!}{=} V = \text{const}$. Consider coupling this voltage source via a gate

capacitor C_g to some arbitrary system described by a Lagrangian $\mathcal{L}$. This setup is shown in Fig. 2.4 together with a spanning tree. Note that in conjunction with a spanning tree of the other system, the branch over C_S could in principle be a closure branch. This does not change the result, though, since the ideal voltage source is assumed to be unaffected by a potential external magnetic flux.

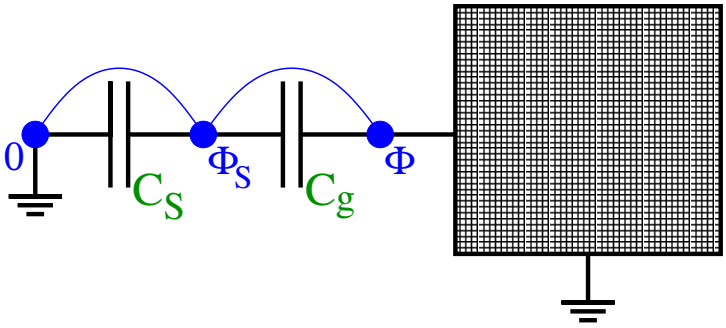

Figure 2.4.: Voltage source coupled through a gate capacitor C_g to a larger system. The flux node Φ is one node of an arbitrary system described by the Lagrangian $\mathcal{L}$. It is represented as a large square in the circuit diagram. The ideal voltage source is modelled as a large capacitor $C_S \to \infty$ charged with $Q_S \to \infty$ such that $Q_S/C_S = V$. As the voltage V is the only essential information entering the Lagrangian, the source capacitor C_S of the voltage source model is usually represented by a mere circle enclosing this voltage label (see Fig. 2.5 or 2.6).

The first branch of the tree is associated with the branch voltage $\dot{\Phi}_S = V$ and causes a capacitive energy shift of $C_S V^2/2$ in the kinetic energy T. As a constant, this term is irrelevant for the dynamics of the system, so we simply drop it. The second branch has a branch voltage of $\dot{\Phi} - \dot{\Phi}_S$, so it produces the term $C_g(\dot{\Phi} - V)^2/2$ in T. Hence, the Lagrangian transforms under this capacitive coupling as

$$\mathcal{L} \mapsto \mathcal{L} + \frac{C_g\left(\dot{\Phi} - V\right)^2}{2} \quad . \tag{2.31}$$

The Legendre transformation is of course affected in a nontrivial way, so there is no easy rule to describe how the Hamiltonian transforms. However, for many systems such as the one in the next example, a voltage bias generically causes a shift in the number operator $\hat{n}$ by some gate-controlled constant.

Cooper pair box

In section 2.1.1, we already learned that the capacitive part of a Josephson junction can be charged with a discrete number of Cooper pairs. Through a capacitively coupled voltage source, this number can be controlled by external parameters. To understand how this comes about, we study the corresponding circuit shown in Fig. 2.5. This setup is also known as Cooper pair box (CPB) and was first presented in [BVJ+98].

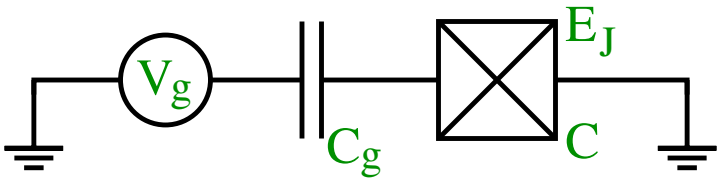

Figure 2.5.: Circuit diagram of a Cooper pair box consisting of a Josephson junction coupled to an external bias voltage V_g via a gate capacitor C_g. The effect of the voltage source is that the relative number of Cooper pairs stored in the capacitor C of the Josephson junction can be controlled by tuning V_g.

Combining the Lagrangian of the Josephson junction given in Eq. (2.28) with the voltage-bias rule derived in Eq. (2.31), we obtain the CPB Lagrangian

$$\mathcal{L} = \frac{C\dot{\Phi}^2}{2} + \frac{C_g\left(\dot{\Phi} - V\right)^2}{2} + E_J \cos\left(\frac{2\pi}{\tilde{\Phi}_0}\Phi\right) \quad . \tag{2.32}$$

Solving the canonical momentum relation $Q = \partial\mathcal{L}/\partial\dot{\Phi}$ for $\dot{\Phi}$ then yields

$$\dot{\Phi} = \frac{1}{C + C_g}\left(Q + C_g V_g\right) \quad . \tag{2.33}$$

After performing the Legendre transformation, completing the square, and neglecting a constant, the Hamiltonian for the CPB in the number and phase variables reads

$$H = \underbrace{\frac{(2e)^2}{2\left(C + C_g\right)}}_{E_C}\left(\hat{n} + \underbrace{\frac{C_g V_g}{2e}}_{-n_g}\right)^2 - E_J \cos\varphi \quad . \tag{2.34}$$

Compared to the unbiased Josephson junction described by Eq. (2.9), we can mark two differences: First the charging energy is reduced a bit by the presence of the gate capacitor C_g. Since this capacitance is usually small $C_g \ll C$, it is often neglected in the expression for the charging energy. Second, the number operator $\hat{n}$ is shifted by the gate-induced offset $n_g = -C_g V_g/2e$. This is interesting insofar as it provides a means to control the preferred number of Cooper pairs from outside.

Together with the flux-tunable Josephson junction depicted in Fig. 2.3, we have now two control parameters for this simple circuit, namely a magnetic field and the applied voltage. If the essential dynamics can be restricted to a two-dimensional computational subspace $\mathrm{span}\{|n\rangle \,|\, n = 0, 1\}$ spanned by the number states $|0\rangle$ and $|1\rangle$ (we will later discuss applications where this is the case), one can perform a so-called two-level approximation (TLA):

$$H \approx \sum_{n,m=0,1} |n\rangle\langle n|\, H\, |m\rangle\langle m| \quad . \tag{2.35}$$

Using the representation of $\hat{n}$ and $\cos\hat{\varphi}$ from Eq. (2.16), we can express these in terms of

the Pauli matrices $\sigma^z = |0\rangle\langle 0| - |1\rangle\langle 1|$ and $\sigma^x = |0\rangle\langle 1| + |1\rangle\langle 0|$:

$$(\hat{n} - n_g)^2 \approx n_g^2 |0\rangle\langle 0| + (1 - n_g)^2 |1\rangle\langle 1| = \left(n_g - \frac{1}{2}\right)\sigma^z + \text{const} \tag{2.36a}$$

$$\cos\hat{\varphi} \approx \frac{1}{2}\left(|0\rangle\langle 1| + |1\rangle\langle 0|\right) = \frac{1}{2}\sigma^x \quad . \tag{2.36b}$$

Thus the CPB Hamiltonian projected onto the computational subspace becomes

$$H \approx E_C\left(n_g - \frac{1}{2}\right)\sigma^z - \frac{E_J(\Phi_{ex})}{2}\sigma^x \quad . \tag{2.37}$$

This already shows a simple example of a qubit realization using superconducting circuits. By unitary time evolution $e^{-iHt/\hbar}$ with Φ_{ex} and V_g as control parameters, we can generate arbitrary single-qubit rotations on the Bloch sphere. With one single qubit, there is of course not that much quantum computation to do; indeed, the difficult part lies in coupling different qubits.

It should be mentioned that there is a certain significance concerning the parameter n_g: Given that $E_J/E_C \ll 1$ (the so-called charge-qubit regime), a voltage of $n_g = 0$ or $n_g = 1$ causes the system to relax into the charge state $|0\rangle$ or $|1\rangle$, respectively. Now a special situation is produced if we tune the gate voltage to $n_g = 1/2$ which causes the ground state to be a uniform superposition of $|0\rangle$ and $|1\rangle$. This is usually called a sweet spot since the dispersion relation as a function of the external voltage has a vanishing first derivative, so the charge qubit is less sensitive to fluctuations in the bias voltage V_g. Gate realizations for this type of qubits generally try not to leave this sweet spot in order not to worsen the qubit coherence.

Another regime for this circuit, the so-called transmon regime, is further discussed in section 2.3. Before we come to that, however, we will look at a specific realization of coupling multiple charge qubits. This will serve as a somewhat more involved example of how to apply the above rules to obtain a Hamiltonian from an electric circuit.

2.2.3. Josephson-inductive coupling

In the following, we derive the circuit Hamiltonian for an array of m Josephson-inductively coupled Cooper pair boxes. The idea has been proposed in [YTN03] and [YWY+08], and we use the circuit (see Fig. 2.6) as a demonstration of how the afore-mentioned rules can be systematically applied.

The Cooper pair boxes are characterized by their capacitances C_i and their Josephson energy E_{Ji}. Each is connected to a bias voltage V_{gi} by a small gate capacitance $C_{gi} \ll C_i$. The Josephson-inductive coupling consists of m Josephson junctions of the same capacitance C_i and potentially different Josephson energies E_{JCi}. All these coupling junctions are connected to ground through a big Josephson junction E_{J0} with a high capacitance C_0, thereby enclosing an external magnetic flux Φ_{ex}.

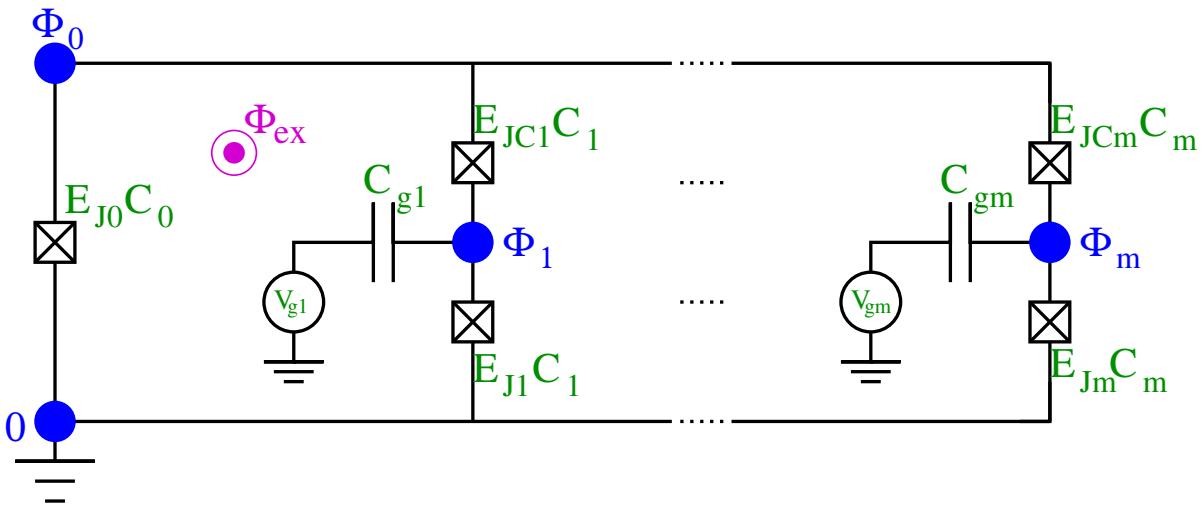

Figure 2.6.: Circuit diagram of m Cooper pair boxes coupled by a Josephson-inductance $J0$. The big blue circles denote the flux nodes of the spanning tree of the circuit diagram. The flux nodes Φ_1 through Φ_m are located at the point where the Cooper pairs reside in the m boxes. Each of these is coupled to the flux node Φ_0 of the Josephson junction $J0$ by an additional tunnel junction JCi. These represent the closure branches that enclose the external magnetic flux Φ_{ex}. Note that there are no flux nodes between the voltage sources V_{gi} and the corresponding gate capacitances C_{gi} inside the spanning tree. The reason is that the effect of the voltage biases on the kinetic energy of the circuit is already accounted for by Eq. (2.31).

The inductive energy U of the circuit is easy to obtain as all Josephson junctions Ji give a contribution of the form $-E_{Ji}\cos\varphi_i$, where $\varphi_i = 2\pi\Phi_i/\tilde{\Phi}_0$. The junctions JCi on the closing branches are not part of the spanning tree, so their contribution includes the external flux Φ_{ex}, resulting in terms of the form $-E_{JCi}\cos(\varphi_0 - \varphi_i + \phi_{ex})$. As before, all lower-case symbols φ_i and ϕ_{ex} represent the dimensionless versions of the flux variables Φ_i and Φ_{ex}. In total, the inductive energy thus amounts to

$$U = -E_{J0}\cos\varphi_0 + \sum_{i=1}^{m}\left(-E_{Ji}\cos\varphi_i - E_{JCi}\cos(\varphi_0 - \varphi_i + \phi_{ex})\right) \quad . \tag{2.38}$$

As U only contains the pure system's variables φ_0 and φ_i ($i \in \{1,\ldots,m\}$), it simply carries through the Legendre transformation and thus already constitutes the potential part of the circuit Hamiltonian H.

The capacitive energy T is a bit harder to handle, because many cross-capacitive terms will arise in the Legendre transformation. In the following, "=" always means up to a constant. We start by splitting T into the contribution T_0 from the coupling junction $J0$, and the contributions T_i from each junction Ji in the spanning tree and JCi outside the spanning tree. Apart form these, T_i also contains the effective contribution of the voltage bias as shown in Eq. (2.31). Hence, in terms of the voltages $\dot{\Phi}_i$, the capacitive energy reads

$$T = T_0 + \sum_{i=1}^{m} T_i \quad , \tag{2.39}$$

where

$$T_0 = \frac{C_0 \dot{\Phi}_0^2}{2} \tag{2.40a}$$

$$T_i = \frac{C_i \dot{\Phi}_i^2}{2} + \frac{C_i \left(\dot{\Phi}_i - \dot{\Phi}_0\right)^2}{2} + \frac{C_{gi} \left(\dot{\Phi}_i - V_{gi}\right)^2}{2} \quad . \tag{2.40b}$$

Since the gate capacitances C_{gi} are in general negligible compared to the junction capacitances C_i, we make one approximation to the capacitive energies T_i, namely that the coefficient of $\dot{\Phi}_i^2$ in T_i becomes $2C_i + C_{gi} \approx 2C_i$. In experimental setups such as the one in [YWY+08], this is usually the case. Thus the capacitive energy reads

$$T_i = \frac{C_i \dot{\Phi}_i^2}{2} + \frac{C_i \left(\dot{\Phi}_i - \dot{\Phi}_0\right)^2}{2} - C_{gi} V_{gi} \dot{\Phi}_i \quad . \tag{2.41}$$

For the Legendre transformation, we need the voltages $\dot{\Phi}_i$ expressed in terms of their canonical conjugates $Q_i = \partial_{\dot{\Phi}_i} T$, which also represent the charges induced by the number of Cooper pairs on each junction capacitor. For these charges, we obtain

$$Q_i = \frac{\partial T_i}{\partial \dot{\Phi}_i} = 2C_i \dot{\Phi}_i - C_i \dot{\Phi}_0 - C_{gi} V_{gi} \tag{2.42a}$$

$$Q_0 = \frac{\partial T}{\partial \dot{\Phi}_0} = \left(C_0 + \sum_{i=1}^{m} C_i \right) \dot{\Phi}_0 - \sum_{i=1}^{m} C_i \dot{\Phi}_i \quad , \tag{2.42b}$$

which can be recast as

$$\dot{\Phi}_i = \frac{Q_i}{2C_i} + \frac{C_{gi} V_{gi}}{2C_i} + \frac{\dot{\Phi}_0}{2} \tag{2.43a}$$

$$\dot{\Phi}_0 = \frac{2Q_0}{C_\Sigma} + \sum_{i=1}^{m} \frac{Q_i}{C_\Sigma} + \sum_{i=1}^{m} \frac{C_{gi} V_{gi}}{C_\Sigma} \quad . \tag{2.43b}$$

Here we introduced the parameter $C_\Sigma = 2C_0 + \sum_{i=1}^{m} C_i$ which is physically equal to twice the total junction capacitance of the circuit.

The Legendre transformation is made up of terms of the form $Q_i \dot{\Phi}_i - T_i$. Since T_i is quadratic in the variables $\dot{\Phi}_i$, the terms arising in this expression need to be carefully ordered. The elimination of $\dot{\Phi}_0$ is postponed until all occurrences of $\dot{\Phi}_0^2$ have been gathered.

Thus we obtain

$$\begin{aligned} Q_i\dot{\Phi}_i - T_i &= \frac{Q_i^2}{2C_i} + \frac{Q_i C_{gi} V_{gi}}{2C_i} + \frac{Q_i\dot{\Phi}_0}{2} - \frac{C_i}{2}\left(2\left[\frac{Q_i}{2C_i} + \frac{C_{gi}V_{gi}}{2C_i}\right]^2 + \frac{\dot{\Phi}_0^2}{2}\right) \\ &\qquad + C_{gi}V_{gi}\left(\frac{Q_i}{2C_i} + \frac{C_{gi}V_{gi}}{2C_i} + \frac{\dot{\Phi}_0}{2}\right) \\ &= \frac{Q_i^2}{4C_i} + \frac{Q_i C_{gi}V_{gi}}{2C_i} + \frac{Q_0 Q_i}{C_\Sigma} + \sum_{j=1}^{m}\frac{Q_i Q_j}{2C_\Sigma} + \sum_{j=1}^{m}\frac{Q_i C_{gj}V_{gj}}{2C_\Sigma} - \frac{C_i\dot{\Phi}_0^2}{4} + \frac{C_{gi}V_{gi}\dot{\Phi}_0}{2} \end{aligned} \tag{2.44a}$$

$$Q_0\dot{\Phi}_0 - T_0 = \frac{2Q_0^2}{C_\Sigma} + \sum_{j=1}^{m}\frac{Q_0 Q_j}{C_\Sigma} + \sum_{j=1}^{m}\frac{Q_0 C_{gj}V_{gj}}{C_\Sigma} - \frac{C_0\dot{\Phi}_0^2}{2} \quad . \tag{2.44b}$$

In the sum over i of these terms, the coefficient of $\dot{\Phi}_0^2$ is $-(2C_0 + \sum_i C_i)/4 = -C_\Sigma/4$. Using the relation

$$-\frac{C_\Sigma}{4}\dot{\Phi}_0^2 + \sum_{i=1}^{m}\frac{C_{gi}V_{gi}}{2}\dot{\Phi}_0 = -\frac{Q_0^2}{C_\Sigma} - \sum_{i,j=1}^{m}\frac{Q_i Q_j}{4C_\Sigma} - \sum_{i=1}^{m}\frac{Q_0 Q_i}{C_\Sigma} \tag{2.45}$$

we arrive at the Hamilton function

$$\begin{aligned} H &= \sum_{i=0}^{m}\left(Q_i\dot{\Phi}_i - T_i\right) + U \\ &= \sum_{i=1}^{m}\frac{Q_i^2}{4C_i} + \sum_{i=1}^{m}\frac{Q_i C_{gi}V_{gi}}{2C_i} + \sum_{i,j=1}^{m}\frac{Q_i Q_j}{4C_\Sigma} + \sum_{i,j=1}^{m}\frac{Q_i C_{gj}V_{gj}}{2C_\Sigma} + \frac{Q_0^2}{C_\Sigma} + \sum_{i=1}^{m}\frac{Q_0 Q_i}{C_\Sigma} + \sum_{i=1}^{m}\frac{Q_0 C_{gi}V_{gi}}{C_\Sigma} + U \quad . \end{aligned} \tag{2.46}$$

The next step is to complete the squares such that the characteristic offset charges and energy scales can be identified, i.e.

$$\begin{aligned} H = &\sum_{i=1}^{m}\left(\frac{1}{4C_i} + \frac{1}{4C_\Sigma}\right)\left(Q_i + C_{gi}V_{gi}\right)^2 + \frac{1}{C_\Sigma}\left(Q_0 + \frac{\sum_{i=1}^{m} C_{gi}V_{gi}}{2}\right)^2 \\ &+ \sum_{1\le i<j\le m}\frac{1}{2C_\Sigma}\left(Q_i + C_{gi}V_{gi}\right)\left(Q_j + C_{gj}V_{gj}\right) + \sum_{i=1}^{m}\frac{1}{C_\Sigma}Q_0 Q_i + U \quad . \end{aligned} \tag{2.47}$$

Now we introduce the variables $n_i = Q_i/2e$ for $i \in \{0, \ldots, m\}$ denoting the respective number of Cooper pairs that the junction capacitors are charged with. Similarly, we define the gate-induced reference numbers $n_{gi} = -C_{gi}V_{gi}/2e$ for $i \in \{1, \ldots, m\}$ (the corresponding reference for $i = 0$ can be expressed in terms of these). The capacitances C_i and C_Σ can be absorbed in the charging energies $E_{Ci} := e^2/C_i$ and $E_{C0} := 4e^2/C_\Sigma$.

After the quantization rule, the Hamiltonian of the circuit finally reads

$$\begin{aligned} H = &\sum_{i=1}^{m} \left(E_{Ci} + \tfrac{1}{4}E_{C0}\right)\left(\hat{n}_i - n_{gi}\right)^2 + E_{C0}\left(\hat{n}_0 - \frac{\sum_{i=1}^{m} n_{gi}}{2}\right)^2 \\ &+ \sum_{1\le i<j\le m} \tfrac{1}{2}E_{C0}\left(\hat{n}_i - n_{gi}\right)\left(\hat{n}_j - n_{gj}\right) + \sum_{i=1}^{m} E_{C0}\,\hat{n}_0\,\hat{n}_i \\ &+ \sum_{i=1}^{m}\left(-E_{Ji}\cos\hat{\varphi}_i - E_{JCi}\cos(\hat{\varphi}_0 - \hat{\varphi}_i + \phi_{ex})\right) - E_{J0}\cos\hat{\varphi}_0 \quad . \end{aligned} \tag{2.48}$$

Here we can observe some physical effects of the circuit components: The shunting of the capacitances belonging to the Josephson junctions results in a shift of $E_{C0}/4$ to each individual CPB's charging energy. The voltage sources V_{gi} induce shifts of the number operators $\hat{n}_i$ as mentioned in section 2.2.2, but the shifts do not affect each occurrence of the number operators. The specific shift of $\hat{n}_0$ in the charging term of the coupling junction can be understood as the capacitive action of the gate-induced charges on the coupling junction (the factor 1/2 coming from the splitting of the CPBs into two Josephson junctions). Finally, we see that the cross-capacitive contributions $\sim \hat{n}_i\hat{n}_j$ are of the same order of magnitude as the charging energy E_{C0} of the coupling junction $J0$, so they should not be neglected unless $E_{C0} \ll E_{Ci}$.

2.3. Circuit QED

The charge qubit described by Eq. (2.34) that we have discussed in the previous section is usually operated in a regime where the charging energy is much greater than the Josephson energy, i.e., E_J/E_C is somewhere between 0.1 and 0.01 (hence the name). This property makes charge qubits quite sensitive to environmental charge fluctuations such that the gate voltages have to be tuned to some sweet spot $n_g \approx 1/2$ where the energy dispersion w.r.t. n_g has a vanishing slope. Nevertheless, sufficient long-time stability is still a major problem since large fluctuations can drive the qubit out of the sweet spot.

To overcome this problem of high charge sensitivity, Koch *et al.* proposed in 2007 another type of superconducting qubits based on the same CPB Hamiltonian, the so-called *transmon* [KYG+07]. It is characterized by an increased ratio of $E_J/E_C \approx 10-100$, and the name refers to a shunted transmission line used to achieve this. When coupled to a transmission line resonator, the system behaves in the same way as cavity quantum electrodynamics (cavity QED) setups in quantum optics. The transmon then takes on the role of an artificial atom whose parameters can be engineered, and the resonator represents the cavity. This has led to the name circuit QED (circuit quantum electrodynamics) [Gir11], and we review the basic constituents in this section.

2.3.1. The transmon

The transmon qubit essentially resembles the ordinary CPB with a flux-tunable Josephson junction, the only difference being an increased energy ratio E_J/E_C that is typically between 10 and 100. This is achieved by shunting the Josephson junction with a large capacitance C_B that effectively increases C, such that $E_C \propto C^{-1}$ becomes quite small compared to E_J. In optical micrographs, this shunting capacitance C_B can often be

directly observed as interdigitated fingers.

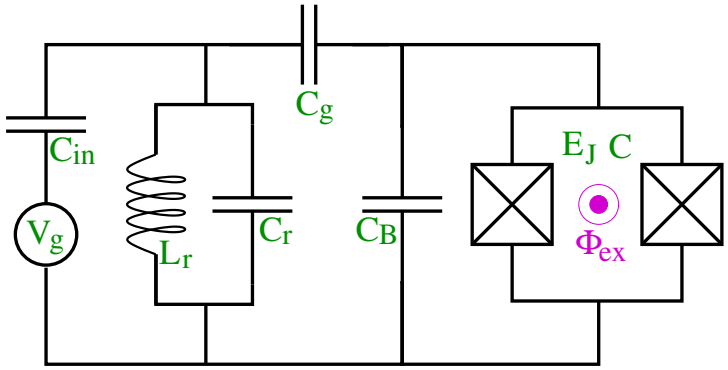

Figure 2.7.: Circuit of the transmon setup. The flux-tunable Josephson junctions are shunted with a large capacitance C_B to increase the charging energy E_C. The voltage source V_g and a transmission line resonator characterized by C_r and L_r are capacitively coupled to the transmon, and an external circuit (not shown) is used to generate the flux for tuning E_J. Figure redrawn from [KYG+07].

What effectively happens in the process of increasing E_J/E_C can be understood from the spectrum of the corresponding Hamiltonian given in Eq. (2.34). In φ-space, the stationary Schrödinger equation for a wave function $\psi(\varphi)$ defined by Eq. (2.12) reads

$$\left[E_C\left(i\frac{\partial}{\partial\varphi} - n_g\right)^2 - E_J\cos\varphi\right]\psi(\varphi) = E\psi(\varphi) \quad . \tag{2.49}$$

This is a type of Mathieu's differential equation and its solution can be expressed in terms of Mathieu sine and cosine functions [AS64]. The eigenenergies E_m are given by Mathieu's characteristic value as shown in [KYG+07]. They are plotted as a function of the gate voltage n_g in Fig. 2.8 for different values of E_J/E_C. One can clearly see how the dependence of the lowest part of the spectrum on the voltage grows much weaker for higher ratios of E_J/E_C. This can be explained as follows:

For large E_C, H is essentially dominated by $E_C(\hat{n} - n_g)^2$ and the eigenvectors are approximately given by the charge states $|n\rangle$ defined in Eq. (2.10). Hence the eigenenergies as a function of the gate voltage $E_m(n_g)$ are narrow parabolas centered at integers. Fluctuations in n_g can thus easily disturb the system, which is exactly the problem of the charge qubit mentioned above. Now by increasing E_J/E_C, the Josephson term in H becomes more and more important which effectively flattens the parabolas. In fact, one can show that the distance between the minimum and the maximum of $E_m(n_g)$ for each level m scales down with $\exp(-\sqrt{32E_J/E_C})$ [KYG+07] (the difference by a factor of 4 comes from the alternative definition of the charging energy in Eq. (2.8)). Thus the system's sensitivity to charge noise through n_g is exponentially suppressed.

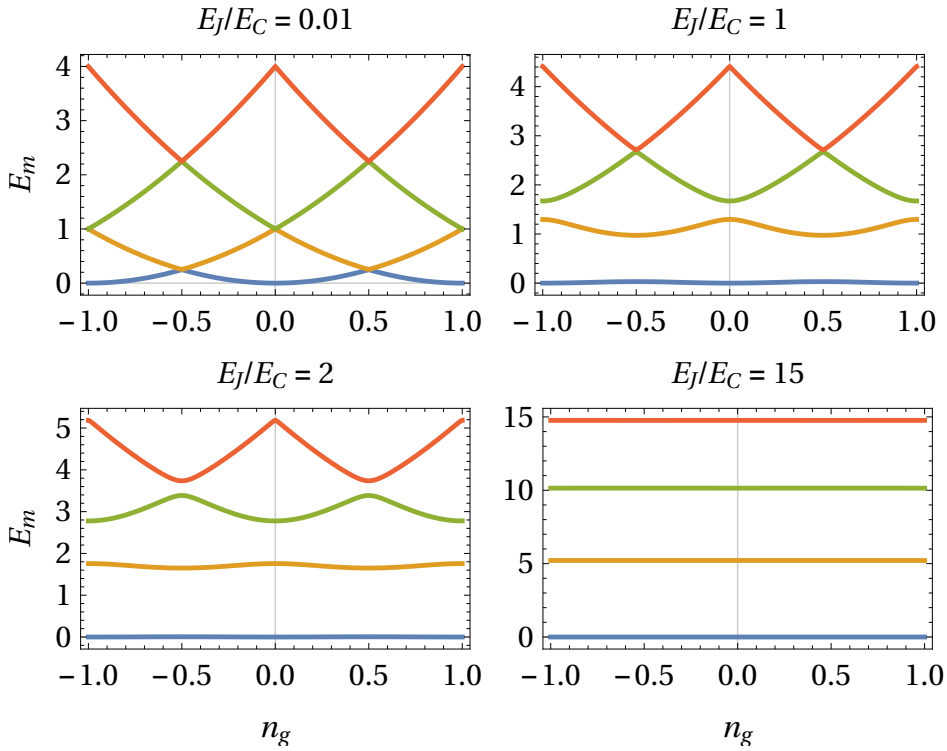

Figure 2.8.: The lowest eigenenergies $E_{m=0,1,2,3}$ of the CPB Hamiltonian in units of E_C as a function of the gate voltage n_g for various ratios of the Josephson energy E_J and the charging energy E_C. For $E_C \gg E_J$ (upper left), the ground state $|m = 0\rangle$ is approx. given by the charge state $|n = \lfloor n_g + \frac{1}{2} \rfloor\rangle$. In that case, the system's sensitivity to changes in the gate voltage is highest. It grows notably weaker on the way to the transmon regime, where the eigenstates $|m\rangle$ become superpositions of charge states around $|\lfloor n_g + \frac{1}{2} \rfloor\rangle$ (see text). Note that the ratios E_J/E_C differ from [KYG+07] by a factor of 4 due to the alternative definition of E_C in Eq. (2.8).

However, the ratio of Josephson energy to charging energy cannot be made arbitrarily large. The problem is that increasing the ratio makes the eigenenergies almost equidistant. More precisely, the relative anharmonicity $\alpha_r = (E_{1\to2} - E_{0\to1})/E_{0\to1}$ goes to 0 which is a problem since gate operations tuned to resonance with some transition (say $E_{0\to1}$) can easily excite other transitions as well. Furthermore, it puts an upper bound on the speed of gate operations. Fortunately, the anharmonicity scales only as $\alpha_r \sim -1/\sqrt{32E_J/E_C}$ [Cot02], i.e., a weak power law compared to the exponential suppression of the charge sensitivity. Hence there is an optimal range for the ratio E_J/E_C.

The eigenstates $|m\rangle$ of the transmon can also be obtained by solving Eq. (2.49) in the charge representation. As the Josephson term couples only adjacent charge states (see Eq. (2.16)), the problem amounts to diagonalizing a tridiagonal matrix. One finds that for $n_g = 0$, the first transmon eigenstates $|m\rangle$ are symmetric and antisymmetric superpositions of the first charge states $|n\rangle \in \{|-5\rangle, \ldots, |5\rangle\}$ [Gam13] (for $n_g \neq 0$, the distribution is shifted accordingly). Using a transmon as a qubit thus also changes the definition of the computational states $|0\rangle$ and $|1\rangle$. Furthermore, due to the reduced anharmonicity, a two-level approximation might not necessarily be possible and higher transmon levels have to be taken into account. On the other hand, this also provides additional degrees of freedom in the realization of qubit gates [GCS15]. We will discuss these issues in more detail in section 5.2.

2.3.2. Transmission line resonator

While the transmon plays the role of the tunable atom in circuit QED, the cavity is represented by a transmission line resonator. This resonator can be described by a simple LC-circuit [BHW+04; WSB+04] labeled by L_r and C_r in Fig. 2.7. The reason that this circuit functions as a single-mode cavity can be seen by examining the circuit Hamiltonian according to section 2.2: The capacitive branch produces the kinetic energy term and the inductive branch yields the potential energy such that we find

$$H = \frac{\hat{Q}^2}{2C_r} + \frac{\hat{\Phi}^2}{2L_r} \quad . \tag{2.50}$$

This is a simple harmonic oscillator that can be diagonalized analogously to the mechanical case, i.e. (up to a constant)

$$H = \hbar\omega_r \hat{a}^\dagger \hat{a} \quad , \tag{2.51}$$

where $\omega_r = 1/\sqrt{L_r C_r}$ is the mode's resonance frequency, and $\hat{a}$ and $\hat{a}^\dagger$ are the bosonic operators. Since the excitations of the resonator are obviously of the electromagnetic kind, they are actually photons. In many experiments, the circuit parameters are tuned to microwave photons. Of course, in experiments there can be multiple modes populating the cavity. This is an effect that experimentalists have to take special care of [Gir11].

The only missing part of the architecture is the coupling between the transmon and the resonator. This is mediated by the capacitor C_g in Fig. 2.7. When doing the full circuit analysis [KYG+07], one finds that the interaction is given by

$$H_{Res \leftrightarrow CPB} = \hbar g \hat{n} (\hat{a} + \hat{a}^\dagger) \quad , \tag{2.52}$$

where g is the coupling strength dependent on the circuit parameters. There is also another intuitive way of understanding how this electric dipole coupling comes about [Gam13]: Apart from the gate voltage, there is now the voltage $\hat{V}_r$ across the LC-circuit determining the offset charge n_g in Eq. (2.34). Note that this voltage is not an external parameter from a voltage source but an operator associated with the variables $\hat{Q}_r$ and $\hat{\Phi}_r$. From the charging term $(\hat{n} - n_g)^2$, we then get a linear contribution $\propto \hat{n}\hat{V}_r$. Rewriting $\hat{V}_r \propto \hat{a} + \hat{a}^\dagger$, we find again Eq. (2.52).

With the circuit QED architecture as an engineerable atom-light interaction, many quantum optics scenarios such as Rabi splitting or the Purcell effect can be investigated. For quantum computing applications, the cavities are useful for coherent control and readout [KYG+07]. This is done in the dispersive regime where the transmon's transition frequencies are much larger than the resonator's frequency ω_r. Then microwave pulses are used for qubit operations, and readout (in the sense of projective measurements) is done by measuring a resonator frequency shift induced by the state of the qubit [Gam13]. In principle, this idea is not limited to one qubit; it has also been used for joint readout of multiple qubits [MCG+07; Gir11].

We will further study the circuit QED architecture in the two-qubit part of section 5.2.

2.4. State of the art

In the last few years, the superconducting qubit community has converged on implementations of the transmon qubit [Rei15] (cf. section 2.3.1) and slight variations of it [BKM+13]. With average gate lengths $\sim 10 - 100\,\text{ns}$ and coherence times $\sim 100\,\mu\text{s}$ [GCS15], the number of operations per qubit coherence has reached a very satisfactory magnitude of about $10^3 - 10^4$. The time scale for single-shot readout at 99% fidelity is converging to around a few 100 ns [Rei15]. Single-qubit gate fidelities of nearly 100% have been reported [BKM+14; SBM+16], and experimentalists work hard on pushing the speed and the fidelity of two-qubit gates based on fixed-frequency transmons [SMC+16] and tunable transmons [BKM+14; MG14]. Furthermore, the first quantum simulation of molecular energies in the sense of Feynman's vision [Fey82] without exponentially costly precompilations has been shown [OBK+15].

Another important step is the realization of small error-correction protocols. The idea of error-correction is to add redundancy by using more physical qubits to represent one logical qubit such that the whole system can preserve its encoded state longer than the individual components. It is actually the same concept that happens for classical codes used in digital computer hardware. The qubit system must detect errors induced by the environment by measuring a part of the redundancy without inferring the whole state of the system since that would project it onto the measurement basis and thus extract too much information. The protocols usually propose correction operations to undo the error; however, in practice they are not carried out explicitly as these gates could induce additional errors. Instead, the changes in the logical computational space are kept track of to compensate for in future operations [BK15]. DiCarlo's group from Delft has presented bit-flip error detection on a linear five-qubit processor [RPH+15], and Martinis' group at UCSB recently demonstrated a three-qubit state preservation by repetitive error detection on a linear nine-qubit array [KBF+15]. However, for demonstration of full fault-tolerance, both bit and phase flip errors on a state must be simultaneously detected. This is currently pursued on a two-dimensional lattice implementing the (rotated) surface code, which has been one of the most successful schemes so far [GCS15]. The group at IBM has demonstrated such a surface code on a square lattice of four superconducting qubits [CMS+15; CSM+15] and on a five-qubit processor [TCM+16], which can be publicly accessed on the IBM cloud [IBM16].

An important step towards building useful quantum computer hardware is of course the process of scaling up to larger processors. This process is becoming more and more an engineering challenge [BK15]. Also, techniques from computer science such as machine learning and big data schemes will find their way into the controlling and calibrating systems [Rei15]. Even though a full-scale universal gate-model quantum computer still lies far in the future, systems of about $\mathcal{O}(100)$ qubits are considered to be well within reach [GCS15].

3. Physical models

In this thesis, we basically examine two models that have been of significant importance in the context of quantum computing. Each model is characterized by its Hamiltonian which has been chosen to support a big range of parameters, such that a wide class of systems occurring in experimental setups can be realized and investigated with the simulation software.

3.1. The CPB model

The first model addresses quantum computing devices based on superconducting circuits. As outlined in chapter 2, these circuits contain Josephson junctions providing the possibility to store Cooper pairs in Cooper pair boxes (CPBs). As this model comprises Hamiltonians containing CPBs and different ways of coupling them, we will refer to it as the CPB model. Its intended purpose is to model various hardware realizations based on CPB qubits such as charge qubits and transmon qubits.

The Hamiltonian consists of 4 separate contributions. The first contains $m+1$ Cooper pair boxes described by the Hamiltonian given in Eq. (2.34). The other three each implement one way of coupling them, namely via a transmission line resonator as described in section 2.3.2 (we set the reduced Planck constant $\hbar = 1$ from now on), through an additional large Josephson junction as shown in section 2.2.3, or capacitively by the electronic interaction of their charges. In total, the complete model Hamiltonian with all parameters reads

$$H = H_{\mathrm{CPB}} + H_{\mathrm{Res}} + H_{\mathrm{JC}} + H_{\mathrm{CC}} \tag{3.1}$$

where

$$\begin{aligned}
H_{\mathrm{CPB}} &= \sum_{i=0}^{m} \left(E_{Ci}(\hat{n}_i - n_{gi})^2 - E_{Ji}\cos\hat{\varphi}_i \right) && \text{(Cooper pair box qubits)} \\
H_{\mathrm{Res}} &= \omega_r \hat{a}^\dagger \hat{a} + \sum_{i=0}^{m} g_i \hat{n}_i (\hat{a} + \hat{a}^\dagger) && \text{(Transmission line resonator)} \\
H_{\mathrm{JC}} &= -\sum_{i=1}^{m} E_{JCi} \cos\left(\hat{\varphi}_0 - \hat{\varphi}_i + \phi_i^{\mathrm{ex}}\right) && \text{(Josephson-inductive coupling)} \\
H_{\mathrm{CC}} &= \sum_{0 \le i < j \le m} E_{Ci,Cj} \left(\hat{n}_i - n^L_{Ci,Cj}\right)\left(\hat{n}_j - n^R_{Ci,Cj}\right) && \text{(Capacitive coupling)}
\end{aligned}$$

Note that all parameters can in principle be time-dependent. For H_{CPB}, the parameters are the charging energies E_{Ci}, the Josephson energies E_{Ji}, and the voltage-induced charge offsets n_{gi}. While the charging energies are usually given by the experimental setup,

the Josephson energies can in principle be tuned through an external magnetic flux (cf. Eq. (2.30)). The offsets n_{gi} can be controlled via external voltages. The first coupling H_{Res} has the resonator's eigenfrequency ω_r and the coupling constants g_i as parameters. The second coupling H_{JC} is defined by the energy scales E_{JCi} and additional magnetic fluxes threading the loops ϕ_i^{ex}. Note that unlike the circuit in section 2.2.3, the model supports different external fluxes for each of the m CPB qubits. The last coupling H_{CC} is parametrized by the energies $E_{Ci,Cj}$ and (potentially different) charge offsets $n_{Ci,Cj}^{L/R}$.

In the simulation, the three coupling Hamiltonians can of course be individually switched on or off depending on the underlying hardware, as using all of them simultaneously might not model a meaningful hardware realization. To model the system given by the Hamiltonian in Eq. (2.48), for instance, we only need the couplings H_{JC} and H_{CC}.

To gain a deeper understanding of the effect of the different terms in Eq. (3.1), we compute the action of H on a basis state $|\psi\rangle = |n_0 \cdots n_m k\rangle$. Each operator in H is either diagonal w.r.t. this basis, or maps $|\psi\rangle$ onto some superposition of states $|\psi'\rangle = |n_0' \cdots n_m' k'\rangle$ where at most two of the indices $n_0' \cdots n_m' k'$ differ by one from those in $|n_0 \cdots n_m k\rangle$. Therefore, we adopt the notation $|\cdots n_i \pm 1 \cdots\rangle$ to indicate only those identifiers that have changed w.r.t. $|\psi\rangle$. Consequently, $|\psi\rangle$ is denoted by $|\cdots\rangle$. Hence the action of $H = H_{\text{CPB}} + H_{\text{Res}} + H_{\text{JC}} + H_{\text{CC}}$ on $|\psi\rangle$ is

$$\begin{aligned} H|\psi\rangle = &\sum_{i=0}^{m} \left(E_{Ci} \left(n_i - n_{gi}\right)^2 |\cdots\rangle - \frac{E_{Ji}}{2} |\cdots n_i + 1 \cdots\rangle - \frac{E_{Ji}}{2} |\cdots n_i - 1 \cdots\rangle \right) \\ &+ \omega_r k |\cdots\rangle + \sum_{i=0}^{m} \left(g_i n_i \sqrt{k} |\cdots k-1\rangle + g_i n_i \sqrt{k+1} |\cdots k+1\rangle \right) \\ &+ \sum_{i=1}^{m} \left(-\frac{E_{JCi}}{2} e^{i\phi_i^{ex}} |n_0 - 1 \cdots n_i + 1 \cdots\rangle - \frac{E_{JCi}}{2} e^{-i\phi_i^{ex}} |n_0 + 1 \cdots n_i - 1 \cdots\rangle \right) \\ &+ \sum_{0 \le i < j \le m} E_{Ci,Cj} \left(n_i - n_{Ci,Cj}^{L}\right) \left(n_j - n_{Ci,Cj}^{R}\right) |\cdots\rangle \quad . \end{aligned} \tag{3.2}$$

Each term can be physically understood in this basis: The first line represents the charging energy associated with $|\cdots\rangle$ and the tunneling interaction which can increase or decrease the corresponding relative number difference of Cooper pairs on each CPB. The second line first attaches the resonator's associated photon energy to the state, and furthermore induces changes in the number of photons dependent on the number of charges on each CPB. The third line has a nice interpretation w.r.t. Fig. 2.6: The coupling Josephson junctions JCi are in fact tunneling contacts between the Cooper pairs at the nodes Φ_i and Φ_0, so the corresponding terms in the Hamiltonian represent the tunneling of single Cooper pairs from Φ_i to Φ_0. Thereby, the magnetic fluxes ϕ_i^{ex} control the phases. The last line is diagonal in the charge basis, so it just associates the proper capacitive interaction energy with the state.

The Hilbert space that the model lives in is a tensor product of the $m+1$ Hilbert spaces spanned by the charge states of each CPB, and the resonator's Hilbert space given by the photonic Fock space, i.e.

$$\mathcal{H}_\infty = \left(\bigotimes_{i=0}^{m} \text{span}\{|n\rangle : n \in \mathbb{Z}\} \right) \otimes \text{span}\{|k\rangle : k \in \mathbb{N}_0\} \quad . \tag{3.3}$$

For the simulation, we truncate the Hilbert space to a finite-dimensional subspace chosen large enough such that all essential dynamics is still contained and the results are independent of these dimensions. This means that we restrict the number states to $n_0 \in \{-N_0, \ldots, N_0\}$ and $n_i \in \{-N_i, \ldots, N_i\}$ Cooper pairs in each box (usually we set $N_1 = \ldots = N_m = N$) and $k \in \{0, \ldots, N_{\mathrm{ph}}\}$ photons in the resonator, i.e.

$$\mathcal{H} := \mathrm{span}\{|n_0\rangle\,|n_1\rangle \cdots |n_m\rangle\,|k\rangle : n_i \in \{-N_i, \ldots, N_i\}\,, k \in \{0, \ldots, N_{\mathrm{ph}}\}\} \quad . \tag{3.4}$$

This process of truncation works by projecting H onto $\mathcal{H}$, i.e., we simply omit all terms in Eq. (3.2) that lie outside $\mathcal{H}$. Note that mathematically, there are some subtleties in keeping the representation of H in terms of $\cos\hat{\varphi}_i$, $\hat{a}$ and $\hat{a}^\dagger$. One example is that we cannot have commutation relations such as $\left[\hat{a}, \hat{a}^\dagger\right] = \mathbb{1}_{\mathrm{Res}}$ anymore, since the commutator has trace 0 while the identity $\mathbb{1}_{\mathrm{Res}}$ has trace $N_{\mathrm{ph}} + 1$. However, as this is physically irrelevant for the simulation, we spare ourselves additional complications in the notation and just keep the representation of H in Eq. (3.1).

In the truncated space $\mathcal{H}$, an arbitrary state $|\Psi\rangle \in \mathcal{H}$ can be represented as

$$|\Psi\rangle = \sum_{n_0 \cdots n_m k} a_{n_0 \cdots n_m k}\,|n_0 \cdots n_m k\rangle \quad , \tag{3.5}$$

where the sum ranges over the finite number of indices determined by Eq. (3.4). We thus have to keep track of all the complex coefficients $a_{n_0 \cdots n_m k}$. Mathematically, this object is a complex tensor of rank $m + 2$ where each index ranges over a variable set of integers. Storing and handling this object efficiently on a computer is a nontrivial task since the program must be written generically for any value of m. As the computer's memory is a one-dimensional array, the coefficients must eventually be addressed by a single index. This works by first shifting each index n_i by N_i into a range of non-negative values $n_i + N_i \in \{0, \ldots, 2N_i\}$ and then introducing a one-dimensional index `idx` given by

$$\texttt{idx} = (n_0 + N_0)S_0 + \cdots + (n_m + N_m)S_m + k \quad . \tag{3.6}$$

Here the numbers S_i are the so-called strides that have the property that $\texttt{idx} \mapsto \texttt{idx} + S_i$ corresponds to $n_i \mapsto n_i + 1$. They can be computed analytically by taking the product of the extents of all lower dimensions, i.e., $S_i = (2N_{i+1} + 1) \cdots (2N_m + 1)(N_{\mathrm{ph}} + 1)$. Consequently, the stride of the photon index k would be $S_{m+1} = 1$, and the stride of the coupling junction index n_0 is $S_0 = (2N_1 + 1) \cdots (2N_m + 1)(N_{\mathrm{ph}} + 1)$. Following this scheme, the highest stride S_{-1} would thus give the total number of complex coefficients in the tensor. The strides further obey the strict ordering relation $S_0 > \cdots > S_m > 1$ and we have $S_i = (2N_{i+1} + 1)S_{i+1}$ for $i < m$. Inverting Eq. (3.6), we can retrieve the indices $(n_0, \ldots, n_m, k)$ from `idx` by using integer division (`div`) and the modulo operation (`mod`) given by taking the remainder of the integer division. For instance, the subindex $n_i + N_i$ can be computed from `idx` by $n_i + N_i = (\texttt{idx mod } S_{i-1})\ \texttt{div}\ S_i$, and the corresponding charge number is given by subtracting N_i from this number.

3.2. The spin model

The second model commonly serves as the basic model to theoretically examine gate-based quantum computation and quantum algorithms [NC11]. It is set in a product space $\mathcal{H} = \mathrm{span}\{|0\rangle, |1\rangle\}^{\otimes N}$ of simple two-level systems, the qubits. A quantum computer that is described within this space represents an ideal quantum computer. In analytical studies, many physical setups (like the Cooper pair box in Eq. (2.37)) are at some point projected onto such two-level systems to examine their potential w.r.t. applications of quantum computing (see also Eqs. (2.36a) and (2.36b)). One purpose of this second model is thus to test such TLAs for the CPB model defined in the previous section.

A prominent setup is given by single spin-1/2 particles, which naturally provide a set of two-level systems. In that sense, a nuclear magnetic resonance (NMR) quantum computer with nuclear spins provides nearly ideal qubits. Equipped with an arbitrary two-particle interaction, this makes up the second model which we therefore call the spin model. It is characterized by its Hamiltonian

$$\begin{aligned} H &= -\sum_{\langle j,k\rangle} \vec{S}_j^T \, \mathbb{J}_{jk} \, \vec{S}_k - \sum_j \vec{h}_j \cdot \vec{S}_j \\ &= -\sum_{1\le j<k\le N} \sum_{\alpha=x,y,z} J_{jk}^\alpha S_j^\alpha S_k^\alpha - \sum_{j=1}^{N} \sum_{\alpha=x,y,z} h_j^\alpha S_j^\alpha \quad , \end{aligned} \tag{3.7}$$

where $S_j^\alpha = \sigma_j^\alpha/2$ is the spin operator defined by the Pauli matrices σ^α ($\alpha \in \{x,y,z\}$) acting on the j^{th} two-level subsystem. $\vec{S}_j$ denotes the corresponding vector of the three spin operators. In terms of spins, the vector $\vec{h}_j = \left(h_j^x, h_j^y, h_j^z\right) \in \mathbb{R}^3$ represents a magnetic field on the j^{th} site and the coupling constants J_{jk}^α in $\mathbb{J}_{jk} = \mathrm{diag}(J_{jk}^x, J_{jk}^y, J_{jk}^z)$ denote the exchange coupling between spin j and k. The sum in Eq. (3.7) is restricted to nearest-neighbor interaction on a one-dimensional lattice, implied by the notation $\langle j,k\rangle$.

An arbitrary state $|\Psi\rangle \in \mathcal{H}$ can be expressed in the computational basis as

$$|\Psi\rangle = \sum_{j_0\cdots j_{N-1}=0,1} a_{j_{N-1}\cdots j_0} \, |j_{N-1}\cdots j_0\rangle = \sum_{n=0}^{2^N-1} a_n \, |n\rangle \quad . \tag{3.8}$$

In this notation, we identify the computational states $|j_{N-1}\cdots j_0\rangle = |n\rangle$ where $j_{N-1}\cdots j_0$ denotes the integer n in binary representation, i.e., $n = j_{N-1}2^{N-1} + \cdots + j_0 2^0$. As in the CPB model (see Eq. (3.5)), we need to store and keep track of the 2^N complex coefficients a_n when we study the state $|\Psi\rangle$. However, since the binary digits $j_{N-1}, \ldots, j_0$ can only be either 0 or 1, this is not as involved as in the CPB model. We simply use a linear array of size 2^N and obtain the index j_i using the binary conjunction `and` from Boolean logic, i.e., $j_i = (n \texttt{ and } 2^i)$. The computational state of the i^{th} spin ($i = 1, \ldots, N$ counted from left to right) is then given by the binary value j_{N-i}.

Gate-model quantum computing usually works by controlling the system's parameters $\vec{h}_j$ and J_{jk}^α and then letting the system undergo a unitary time evolution $U = e^{-itH}$ (in the simplified case of time-independent parameters). The transformation U then corresponds to the gate that is being applied to the qubits. Our system given by Eq. (3.7) can thus be used to implement single-qubit gates using the fields $\vec{h}_j$ and two-qubit gates using

the exchange couplings J^{α}_{jk}. Remarkably, the special case $J^{y}_{jk} = J^{z}_{jk} = 0$ corresponding to the Ising spin model is already universal for quantum computing [Llo93]. In fact, it can be shown that any system providing single-qubit rotations and one nontrivial two-qubit gate can be used to implement all unitary operations in successive sequences of time evolutions [DiV95; DBK+00]. Nontrivial in that context means that the two-qubit gate needs to be capable of mapping product states $|\psi\rangle \otimes |\phi\rangle$ to entangled states such that they cannot be expressed as product states anymore. In the set of all two-level unitaries, almost all matrices have this property [DBE95]. Famous examples of such gates are the controlled-not and the controlled-phase gate

$$\text{CNOT} : |i\rangle|j\rangle \mapsto |i\rangle|i \text{ xor } j\rangle \tag{3.9}$$

$$\text{CPHASE} : |i\rangle|j\rangle \mapsto (-1)^{i \text{ and } j} |i\rangle|j\rangle \quad , \tag{3.10}$$

which both map the product state $|{+}{+}\rangle$ where $|\pm\rangle := (|0\rangle \pm |1\rangle)/\sqrt{2}$ to a maximally entangled state. Of course, the set of well implementable nontrivial two-qubit gates is ultimately dictated by the underlying physical hardware.

For some instances of the model in Eq. (3.1) and corresponding two-level approximations that can be represented by Eq. (3.7), we will explicitly examine and compare various realizations of quantum gates in chapter 5. Before we can do that, however, we need to focus on the program and the algorithms to actually simulate the hardware given by the above Hamiltonians, which is the purpose of the following chapter.

4. Simulation software

A major part of this thesis lies in the development of a software application and the implementation of suitable algorithms to simulate and investigate the physical models introduced in the previous chapter. To run the simulations for different models and examine the influence of various device parameters, the program offers a graphical user interface and visualizations of the results as three-dimensional animations and suitable time-evolution plots. A short description and some screenshots of the interface are presented in appendix F.

As the models in chapter 3 are expressed in terms of a Hamiltonian, the simulation is basically required to solve the TDSE given in Eq. (1.1) for arbitrary initial states. For this purpose, the program offers a choice of numerical algorithms that are either fast or capable of making huge leaps in time. In the context of quantum computation, the application further supports the specification of sequences of elementary gates through the corresponding parameters in the Hamiltonian, thus emulating a means of programming the hardware. For a given sequence of gates, the evolution of the initial state can be visualized in terms of three-dimensional arrows on the Bloch sphere or by means of the probabilities to measure certain states in the Hilbert space. Last but not least, the software framework provides a means of assessing effective Hamiltonians and gates that rely on the interaction with additional degrees of freedom outside the computational subspace.

In this chapter, we first review the numerical algorithms used to solve the TDSE, following the presentation in [DM06]. Then we establish the concrete implementation of these algorithms for the physical models discussed in chapter 3. A precise evaluation of the actions of all operators composing the Hamiltonians and their exponentials will prove to be inevitable for this step. Subsequently, we present means to validate the correctness of the implementations and measure the accuracy. After that, we will briefly outline how the information for the visualization is obtained from the data. Finally, we describe the method to examine effective evolutions in the computational subspace.

4.1. Numerical algorithms

The central goal of the numerical algorithms studied in this thesis is to solve the TDSE. For a state $|\Psi(t)\rangle \in \mathcal{H}$, it can be expressed as the partial differential equation ($\hbar = 1$)

$$i\frac{\partial}{\partial t}|\Psi(t)\rangle = H(t)\,|\Psi(t)\rangle \quad , \tag{4.1}$$

where the operator $H(t)$ is the Hamiltonian of the system. In this abstract form, the TDSE exposes only a derivative w.r.t. time; however the Hamiltonian can contain other derivatives depending on the chosen representation. The problem at hand is to obtain the state $|\Psi(t)\rangle$ for a certain set of times t from a given initial state $|\Psi(0)\rangle$. A standard technique to solve the problem is to discretize the partial derivative w.r.t. time, and

iterate the equation in time steps τ. For applications in quantum mechanics where the norm of $|\Psi(t)\rangle$ is conserved, however, a far more natural approach would be to consider algorithms that preserve the unitarity of the time evolution by construction. With that goal in mind, we express the formal solution to Eq. (4.1) in terms of a unitary time evolution operator:

$$|\Psi(t)\rangle = U(t,0)\,|\Psi(0)\rangle \quad , \tag{4.2}$$

where [BF04]

$$U(t,0) = \mathcal{T}_t \left(e^{-it\int_0^t dt'\, H(t')} \right) \quad . \tag{4.3}$$

The symbol $\mathcal{T}_t$ is the time-ordering symbol that indicates that in all terms in the series expansion of the exponential, the product of Hamiltonians $H(t')H(t'')\cdots$ must be ordered so that $t' < t'' < \cdots$. Eventually, we are interested in not only the final state $|\Psi(t)\rangle$, but also intermediate states in the evolution from 0 to t. On a computer, the number of these intermediate states can only be finite, so we have to divide the time evolution in discrete time steps τ. It turns out that this requirement can be used to simplify Eq. (4.3). For this purpose, we utilize a group property of $U(t,0)$, namely

$$U(t,0) = U(t,t-\tau)U(t-\tau,t-2\tau)\cdots U(\tau,0) \quad . \tag{4.4}$$

By making τ sufficiently small, we can achieve that the Hamiltonian does essentially not change within one time step. Of course, we can adjust the time steps dynamically depending on the properties of H; the essential idea is that we have to make sure that at some time t_0, $H(t_0)$ and $H(t_0+\tau)$ are well approximated by $H(t_0+\tau/2)$. Then the expression for the time evolution operator Eq. (4.3) boils down to the simple version for a time-independent Hamiltonian

$$U(t_0+\tau,t_0) = e^{-i\tau H\left(t_0+\frac{\tau}{2}\right)} \quad . \tag{4.5}$$

It is this expression that the algorithms developed in this thesis are based on. See also [DMH+02] and, in particular, [DM06] for a comprehensive survey of the algorithms and a special focus on quantum computation using the spin model from section 3.2 for applications in NMR quantum computing.

Note that the simulation is eventually carried out on a digital computer, so the states $|\Psi(t)\rangle$ will always be represented by a finite set of complex double-precision numbers. Moreover, the Hamiltonian can be expressed as a finite matrix and the Hilbert space is always finite-dimensional. Hence we have to truncate and discretize the system in an appropriate way without changing the physics. This means that we need to make sure that the obtained solution always agrees with the exact mathematical solution up to some specified numerical precision. Due to the use of double-precision floating-point arithmetic, this precision is always bounded from below by 15 decimal digits (the IEEE 754 double-precision format contains 52 binary digits for the mantissa [08]). Above this bound, any algorithm is required to be able to go to arbitrary precision by refining the discretization. We will check this requirement and some other theoretical validations for the algorithms and models under consideration in section 4.2.

4.1.1. Exact diagonalization

The most straightforward approach to obtain the unitary time evolution operator in Eq. (4.5) is to simply calculate it. This means, given the action of the Hamiltonian on all of the D basis states (on the computer we have $D = \dim \mathcal{H} < \infty$), we can construct a complex matrix H of size $D \times D$ with each basis state's image in the columns. Since the Hamiltonian is Hermitian, it can be diagonalized and we can compute its eigendecomposition $H = V\Lambda V^\dagger$. Here, V is a unitary matrix whose columns comprise an orthonormal basis of $\mathcal{H}$ given by the complex eigenvectors of H, and Λ is a diagonal matrix containing the corresponding real eigenvalues of H. The unitary time evolution operator $U = e^{-i\tau H}$ (we set $t_0 = 0$ and $H = H(t_0 + \tau/2)$ in Eq. (4.5) for simplicity) can then be calculated via

$$U = e^{-i\tau H} = V e^{-i\tau\Lambda} V^\dagger \quad , \tag{4.6}$$

where the exponential of the diagonal matrix Λ can just be taken component-wise. The evolution of some state $|\Psi\rangle$ under U then amounts to two matrix-vector multiplications and one component-wise multiplication with complex phases from Λ.

The advantage of this approach is that the complicated task of computing the eigendecomposition of H can be delegated to well-established high-performance linear algebra libraries such as LAPACK [ABB+99] and the Eigen C++ template library [GJ10]. For a complex Hermitian matrix H, most of the algorithms can be divided into three stages:

(a) Reduction to tridiagonal form $T = Q^\dagger H Q$ using similarity transformations Q, thus preserving the spectrum of H

(b) Tridiagonal eigensolver $TZ = Z\Lambda$ where Z contains the eigenvectors of T and Λ the eigenvalues of T and H

(c) Backtransformation of the eigenvectors $V = QZ$ to obtain the eigenvectors of H from those of T

The heart of the algorithms lies in the second step, i.e., the tridiagonal eigensolver. One of the most efficient methods to do this is called Multiple Relatively Robust Representations (MR^3) which runs in $\mathcal{O}(D^2)$ [DMP+07].

However, this approach does not exploit many of the specific features of the Hamiltonian. For the comparatively large Hilbert space of the CPB model (see Eq. (3.4)), the full diagonalization is only feasible for smaller systems where the full eigenproblem can still be solved. Since the other two algorithms presented in the next sections are specifically tailored to the purpose of computing the time evolution of $|\Psi\rangle$, they are still orders of magnitude faster for practical purposes. In any case, the exact diagonalization approach is an essential tool to check the correctness of the other algorithms.

4.1.2. Suzuki-Trotter product-formula algorithm

A class of efficient algorithms that inherently preserve the unitarity of the time evolution operator U is based on systematic product decompositions of U into simpler unitary operations. Since all matrices in the decomposition are unitary, the algorithms are unconditionally stable. The framework has been presented and discussed in [DeR87], along

with applications to prominent physical systems and many rigorous statements about the character of the algorithms.

The central idea is to decompose the Hamiltonian into K Hermitian matrices $H = \sum_{k=1}^{K} H_k$ such that the exponentials $e^{-i\tau H_k}$ are easy to compute. The choice of basis to represent the Hamiltonian is crucial for this step. We then approximate the time evolution operator from Eq. (4.3) for the time-independent Hamiltonian $H = \sum_{k=1}^{K} H_k$

$$U(\tau) = e^{-i\tau(H_1+\cdots+H_K)} \quad , \tag{4.7}$$

by a product of K simple unitary matrices

$$\tilde{U}_1(\tau) := e^{-i\tau H_1} \cdots e^{-i\tau H_K} \quad . \tag{4.8}$$

The Lie-Trotter-Suzuki product-formula [SMK77]

$$U(\tau) = \lim_{m\to\infty} \tilde{U}_1\big(\tfrac{\tau}{m}\big)^m \tag{4.9}$$

already suggests that this decomposition might be a good approximation if τ is sufficiently small. In fact, by expanding the exponentials in Eq. (4.8) into a series and collecting all terms up to first order in τ (which essentially constitute H), we see that $\tilde{U}_1$ is a proper first-order approximation in τ. This means that we have

$$\Big\| U(\tau) - \tilde{U}_1(\tau) \Big\|_F \leq \text{const} \cdot \tau^2 \quad , \tag{4.10}$$

where $\|\cdot\|_F$ denotes the Frobenius norm (see appendix C) and the constant can be analytically expressed in terms of the commutators of different H_k [DeR87].

The nice thing of the product-formula framework is that the accuracy of the approximation to $U(\tau)$ can be systematically improved at almost no additional programming effort: Once the first-order approximation $\tilde{U}_1(\tau)$ has been implemented, we can obtain a second-order and a fourth-order approximation by using [DM06]

$$\tilde{U}_2(\tau) := \tilde{U}_1^\dagger(-\tfrac{\tau}{2})\, \tilde{U}_1(\tfrac{\tau}{2}) \tag{4.11a}$$

$$\tilde{U}_4(\tau) := \tilde{U}_2(a\tau)\, \tilde{U}_2(a\tau)\, \tilde{U}_2((1-4a)\tau)\, \tilde{U}_2(a\tau)\, \tilde{U}_2(a\tau) \quad , \tag{4.11b}$$

where $a = 1/\big(4 - 4^{1/3}\big)$. For these expressions, there are rigorous bounds on the local error [DeR87], i.e.

$$\Big\| U(\tau) - \tilde{U}_2(\tau) \Big\|_F \leq \text{const} \cdot \tau^3 \tag{4.12a}$$

$$\Big\| U(\tau) - \tilde{U}_4(\tau) \Big\|_F \leq \text{const} \cdot \tau^5 \quad , \tag{4.12b}$$

according to the order of the approximation. In principle, this process can be continued to obtain even higher-order approximations [Suz91]. However, in most cases Eq. (4.11a) and Eq. (4.11b) suffice to find the mathematical solution to arbitrary precision.

Using the actual implementation, we can in fact verify the local error bounds in Eqs. (4.10), (4.12a), and (4.12b) using the following relation: Let $\psi(\tau) = \tilde{U}_n(\tau)\psi(0)$ and $\psi_{\text{exact}}(\tau) = U(\tau)\psi(0)$ denote the D-dimensional complex vectors obtained from the time evolution. By computing the Euclidean norm (see appendix C) of their difference,

we obtain for $n \in \{1, 2, 4\}$

$$\begin{aligned} \|\psi(\tau) - \psi_{\text{exact}}(\tau)\| &\leq \left\| \tilde{U}_n(\tau) - U(\tau) \right\|_F \underbrace{\|\psi(0)\|}_{1} \\ &\leq \text{const} \cdot \tau^{n+1} \quad . \end{aligned} \tag{4.13}$$

This bound will be investigated in section 4.2. Note that this expression contains the bare complex coefficients and not some fidelity based on the overlap of the states. Hence the algorithm also produces the correct global phases. In practice, we see that even when the approximation $\tilde{U}_n(\tau)$ is only first- or second-order, the difference comes from some global phases such that the actual fidelity of the states is much better. To see whether a lesser approximation still suffices, we only have to check if the expectation values under consideration numerically remain the same after decreasing the order.

Due to the simplicity of dynamically adjusting the algorithm's accuracy without much computational effort, the product-formula approach is especially suited for efficient high-resolution simulations. For the CPB model, e.g., it is no problem to go to sub-picoseconds while the average gate times are on the order of $10 - 100$ nanoseconds. The Chebyshev algorithm discussed in the next section can in turn be used to make huge leaps in time at high accuracy, so both methods complement each other well.

We now proceed to construct the particular decompositions of the Hamiltonians of the CPB model and the spin model from Eq. (3.1) and Eq. (3.7), respectively.

CPB model

As we want the simulation to provide the option of using only a selected combination of the qubit couplings $H_{\text{Res}}, H_{\text{JC}}$, and H_{CC}, the first level of decomposition lies in the four Hamiltonians in Eq. (3.1). We discuss each of them separately and summarize the final decomposition in the end.

(CPB) For the CPB Hamiltonian H_{CPB}, the first thing to note is that the different Cooper pair box qubits all commute, so we define $H_{\text{CPB}} = \sum_{i=0}^{m} H^i_{\text{CPB}}$ with each $H^i_{\text{CPB}} = E_{Ci}(\hat{n}_i - n_{gi})^2 - E_{Ji} \cos \hat{\varphi}_i$. From Eq. (3.2), we find that in the chosen basis of charge states $|n\rangle_i$ on this part of the Hilbert space, each term can be represented by a tridiagonal matrix

$$H^i_{\text{CPB}} \stackrel{\bullet}{=} \begin{array}{c} \begin{matrix} |-N_i\rangle_i & |-N_i+1\rangle_i & \cdots & |N_i-1\rangle_i & |N_i\rangle_i \end{matrix} \\ \begin{pmatrix} E^i_{-N_i}/2 & -E_{Ji} & & & \\ -E_{Ji} & E^i_{-N_i+1} & & & \\ & & \ddots & & \\ & & & E^i_{N_i-1} & -E_{Ji} \\ & & & -E_{Ji} & E^i_{N_i}/2 \end{pmatrix} \end{array} , \tag{4.14}$$

where

$$E^i_n = \begin{cases} 2E_{Ci}(n - n_{gi})^2 & (n = -N_i \text{ or } n = N_i) \\ E_{Ci}(n - n_{gi})^2 & (\text{otherwise}) \end{cases} . \tag{4.15}$$

The additional factor of 2 in the definition of $E^i_{-N_i}$ and $E^i_{N_i}$ is only for notational convenience in the following decomposition. By analogy with the particle moving in one dimension in [DeR87], we write this matrix as a sum of two block-diagonal matrices

$$H^i_{\mathrm{CPB}} \overset{\bullet}{=} \begin{pmatrix} \overset{}{\ddots} & & & & \\ & \overset{|n\rangle_i\,,|n+1\rangle_i}{H^{i,n}_{\mathrm{CPB}}} & & & \\ & & \ddots & & \\ & & & \overset{|N\rangle_i}{0} & \end{pmatrix} + \begin{pmatrix} \overset{|-N\rangle_i}{0} & & & \\ & \ddots & & \\ & & \overset{|n\rangle_i\,,|n+1\rangle_i}{H^{i,n}_{\mathrm{CPB}}} & \\ & & & \ddots \end{pmatrix} , \tag{4.16}$$

where

$$H^{i,n}_{\mathrm{CPB}} \overset{\bullet}{=} \begin{pmatrix} \overset{|n\rangle_i}{E^i_n/2} & \overset{|n+1\rangle_i}{-E_{Ji}/2} \\ -E_{Ji}/2 & E^i_{n+1}/2 \end{pmatrix} . \tag{4.17}$$

We label the first matrix in Eq. (4.16) *even* and the second matrix *odd* since for each of the contained 2×2 submatrices, $n + N_i$ is either even or odd. For the corresponding time evolution $U^{\mathrm{even/odd}}_{\mathrm{CPB}}$, we can then apply the matrix exponential of each 2×2 block separately. The only approximation lies in the decomposition corresponding to Eq. (4.16) as within one even/odd group, all submatrices act on different two-dimensional subspaces and thus commute. By using the algebraic analog to Euler's formula for the Pauli matrices (see appendix D), we obtain for the matrix exponential

$$e^{-i\tau H^{i,n}_{\mathrm{CPB}}} \overset{\bullet}{=} e^{-\frac{i\tau}{4}(E^i_n+E^i_{n+1})} \begin{pmatrix} \cos(v\tau) - i\frac{\Delta E}{4v}\sin(v\tau) & i\frac{E_{Ji}}{2v}\sin(v\tau) \\ i\frac{E_{Ji}}{2v}\sin(v\tau) & \cos(v\tau) + i\frac{\Delta E}{4v}\sin(v\tau) \end{pmatrix} , \tag{4.18}$$

where $\Delta E = E^i_n - E^i_{n+1}$ and $v = \sqrt{\Delta E^2 + 4E^2_{Ji}}/4$. Note that in this case, all global phases of the transformations must be included in the algorithm since they become relative phases on the total Hilbert space.

So we only have to implement 2×2 transformations on the complex coefficients of the tensor in Eq. (3.5). This means that for a certain set of indices (`idx`, `idx'`) given by Eq. (3.6), we have to transform the coefficients ($a_{\texttt{idx}}, a_{\texttt{idx'}}$). For the matrix in Eq. (4.18), this has to be done for each `idx` with $n_i = n$, and the second index corresponding to $n_i = n + 1$ is given by `idx'` = `idx` + S_i.

(Res) The resonator Hamiltonian H_{Res} in Eq. (3.1) consists of two parts, namely the resonator itself and its coupling to the qubits. The resonator term $\omega_r \hat{a}^\dagger \hat{a} = \sum_{k=0}^{N_{\mathrm{ph}}} k\omega_r \, |k\rangle\langle k|_{\mathrm{Res}}$ is diagonal in the selected basis, so the corresponding factor $U^0_{\mathrm{Res}} := e^{-i\tau\omega_r \hat{a}^\dagger \hat{a}}$ in the product decomposition of U just attaches a phase $e^{-i\tau\omega_r k}$ to each $a_{\texttt{idx}}$ with `idx mod` $N_{\mathrm{ph}} = k$.

Each term in the second part of the Hamiltonian $H^i_{\mathrm{Res}} := g_i \hat{n}_i (\hat{a} + \hat{a})^\dagger$ couples $|n\rangle_i \, |k\rangle_{\mathrm{Res}}$ with the corresponding states for $k + 1$ and $k - 1$, so it is tridiagonal in the subspace spanned by the photon states $|k\rangle_{\mathrm{Res}}$. Hence we can apply the same decomposition into even and odd block-diagonal matrices as in Eq. (4.16). For fixed n, each 2×2 block is

then given by

$$H_{\mathrm{Res}}^{i,n,k} \doteq \sqrt{k+1}\, g_i\, n \begin{pmatrix} |k\rangle_{\mathrm{Res}} & |k+1\rangle_{\mathrm{Res}} \\ 0 & 1 \\ 1 & 0 \end{pmatrix} \quad . \tag{4.19}$$

The corresponding factor in the time evolution reads

$$e^{-i\tau H_{\mathrm{Res}}^{i,n,k}} \doteq \begin{pmatrix} \cos(\eta\tau) & -i\sin(\eta\tau) \\ -i\sin(\eta\tau) & \cos(\eta\tau) \end{pmatrix} \quad , \tag{4.20}$$

where $\eta = \sqrt{k+1} g_i n$. Again, within the total evolution $U_{\mathrm{Res}}^{\mathrm{even/odd}}$, each pair of two-dimensional transformations commute so their specific order of evaluation does not matter.

(JC) For the terms in the Josephson-inductive coupling Hamiltonian $H_{\mathrm{JC}} = \sum_{i=1}^{m} H_{\mathrm{JC}}^i$, we obtain by expanding the cosines into exponentials and applying Eq. (2.15)

$$\begin{aligned} H_{\mathrm{JC}}^i &= -E_{JCi} \cos(\hat{\varphi}_0 - \hat{\varphi}_i + \phi_i^{\mathrm{ex}}) \qquad (4.21) \\ &= -\frac{E_{JCi}}{2} \sum_{n_0=-N_0}^{N_0-1} \sum_{n=-N_i}^{N_i-1} \left(e^{i\phi_i^{\mathrm{ex}}} |n_0\rangle\langle n_0+1|_0 \, |n+1\rangle\langle n|_i + e^{-i\phi_i^{\mathrm{ex}}} |n_0+1\rangle\langle n_0|_0 \, |n\rangle\langle n+1|_i \right) \quad . \end{aligned}$$

The tricky thing is now that H_{JC}^i is tridiagonal both in the $|n_0\rangle_0$ part of the Hilbert space and in the $|n\rangle_i$ part. Thus we have to extend the decomposition in Eq. (4.16), namely into four matrices in which $n_0 + N_0$ and $n + N_i$ are both even, both odd, or one even and the other odd. Inside the corresponding time evolution operators $U_{\mathrm{JC}}^{\mathrm{even/odd,even/odd}}$, these matrices again consist of simple commuting two-level transformations, and we have for some fixed n_0 and n:

$$H_{\mathrm{JC}}^{i,n_0,n} \doteq -\frac{E_{JCi}}{2} \begin{pmatrix} |n_0\rangle_0 |n+1\rangle_i & |n_0+1\rangle_0 |n\rangle_i \\ 0 & e^{i\phi_i^{ex}} \\ e^{-i\phi_i^{ex}} & 0 \end{pmatrix} \tag{4.22}$$

with the corresponding time evolution

$$e^{-i\tau H_{\mathrm{JC}}^{i,n_0,n}} \doteq \begin{pmatrix} \cos(\chi\tau) & ie^{i\phi_i^{\mathrm{ex}}} \sin(\chi\tau) \\ ie^{-i\phi_i^{\mathrm{ex}}} \sin(\chi\tau) & \cos(\chi\tau) \end{pmatrix} \quad , \tag{4.23}$$

where $\chi = E_{JCi}/2$. Compared to the CPB part, this matrix now transforms all the coefficients $(a_{\mathtt{idx}+S_i}, a_{\mathtt{idx}+S_0})$ for each `idx` with fixed n_0 and $n_i = n$.

(CC) The final term is the capacitive coupling H_{CC}. As it is already diagonal in the charge states, its effect in the time evolution U_{CC} is similar to U_{Res}^0 in that it just adds phases to each coefficient of $|\Psi\rangle$. This means that it maps

$$a_{\mathtt{idx}} \mapsto e^{-i\tau E_{Ci,Cj}(n_i - n_{Ci,Cj}^L)(n_j - n_{Ci,Cj}^R)} a_{\mathtt{idx}} \tag{4.24}$$

for each `idx` of the linearized tensor of coefficients.

In summary, the total first-order decomposition of $U = e^{-i\tau H}$ reads

$$\tilde{U}_1 := U_{\mathrm{CPB}}^{\mathrm{even}}\, U_{\mathrm{CPB}}^{\mathrm{odd}}\, U_{\mathrm{Res}}^{0}\, U_{\mathrm{Res}}^{\mathrm{even}}\, U_{\mathrm{Res}}^{\mathrm{odd}}\, U_{\mathrm{JC}}^{\mathrm{even,even}}\, U_{\mathrm{JC}}^{\mathrm{even,odd}}\, U_{\mathrm{JC}}^{\mathrm{odd,even}}\, U_{\mathrm{JC}}^{\mathrm{odd,odd}}\, U_{\mathrm{CC}} \quad , \tag{4.25}$$

with

$$U_{\mathrm{CPB}}^{\mathrm{even/odd}} = \prod_{i=0}^{m} \prod_{\substack{n=-N_i \\ n+N_i \text{ even/odd}}}^{N_i-1} e^{-i\tau H_{\mathrm{CPB}}^{i,n}} \quad , \qquad H_{\mathrm{CPB}}^{i,n} \overset{\bullet}{=} \begin{pmatrix} |n\rangle_i & |n+1\rangle_i \\ E_n^i/2 & -E_{Ji}/2 \\ -E_{Ji}/2 & E_{n+1}^i/2 \end{pmatrix}$$

$$U_{\mathrm{Res}}^{0} = e^{-i\omega_r \tau \hat{a}^\dagger \hat{a}} \quad , \qquad \hat{a}^\dagger \hat{a} = \sum_{k=0}^{N_{\mathrm{ph}}} k\, |k\rangle\langle k|_{\mathrm{Res}}$$

$$U_{\mathrm{Res}}^{\mathrm{even/odd}} = \prod_{i=0}^{m} \prod_{n=-N_i}^{N_i} \prod_{\substack{k=0 \\ k \text{ even/odd}}}^{N_{\mathrm{ph}}-1} e^{-i\tau H_{\mathrm{Res}}^{i,n,k}} \quad , \qquad H_{\mathrm{Res}}^{i,n,k} \overset{\bullet}{=} \sqrt{k+1}\, g_i\, n \begin{pmatrix} |k\rangle_{\mathrm{Res}} & |k+1\rangle_{\mathrm{Res}} \\ 0 & 1 \\ 1 & 0 \end{pmatrix}$$

$$U_{\mathrm{JC}}^{\mathrm{even/odd,even/odd}} = \prod_{i=1}^{m} \prod_{\substack{n_0=-N_0 \\ n_0+N_0 \\ \text{even/odd}}}^{N_0-1} \prod_{\substack{n=-N_i \\ n+N_i \\ \text{even/odd}}}^{N_i-1} e^{-i\tau H_{\mathrm{JC}}^{i,n_0,n}}, \quad H_{\mathrm{JC}}^{i,n_0,n} \overset{\bullet}{=} -\frac{E_{JCi}}{2} \begin{pmatrix} |n_0\rangle_0 |n+1\rangle_i & |n_0+1\rangle_0 |n\rangle_i \\ 0 & e^{i\phi_i^{ex}} \\ e^{-i\phi_i^{ex}} & 0 \end{pmatrix}$$

$$U_{\mathrm{CC}} = \prod_{0 \le i < j \le m} e^{-i\tau E_{Ci,Cj} \left(\hat{n}_i - n_{Ci,Cj}^L\right)\left(\hat{n}_j - n_{Ci,Cj}^R\right)} \quad , \qquad \hat{n}_i = \sum_{n=-N_i}^{N_i} n\, |n\rangle\langle n|_i$$

Except for the transformation U_{JC}, all factors inside each unitary transformation in Eq. (4.25) commute and can be carried out in an arbitrary order without compromising the accuracy. Thus the number of approximations used in the product decomposition is not so high. Moreover, even though the model looks quite complex, it basically only requires unary and binary transformations on the coefficients $a_{\texttt{idx}}$ from Eq. (3.5). Nevertheless, in the actual implementation, there are many things that can go wrong w.r.t. ordering and indexing. Therefore we will check and compare all implementations with the exact diagonalization in section 4.2.

Spin model

For the spin Hamiltonian in Eq. (3.7), the first step is to decompose H into single-qubit and two-qubit terms. As the single-qubit terms in $-\sum_j \vec{h}_j \cdot \vec{S}_j$ for different j all commute, we have the exact relation

$$e^{i\tau \sum_{j=1}^{N} \vec{h}_j \cdot \vec{S}_j} = \prod_{j=1}^{N} e^{i\tau \vec{h}_j \cdot \vec{S}_j} \quad . \tag{4.26}$$

Each factor in the product acts only on the two-dimensional subspace $\mathcal{H}_j = \mathrm{span}\{|0\rangle_j, |1\rangle_j\}$ of the total Hilbert space $\mathcal{H} = \bigotimes_{j=1}^{N} \mathcal{H}_j$. In this subspace, the matrix exponential can

again be evaluated analytically (cf. appendix D). The result is

$$e^{i\tau\vec{h}_j\cdot\vec{S}_j} \stackrel{\bullet}{=} \begin{matrix} \\ |0\rangle_j \\ |1\rangle_j \end{matrix} \begin{matrix} \begin{matrix} |0\rangle_j & |1\rangle_j \end{matrix} \\ \begin{pmatrix} c + ish_j^z/h_j & is(h_j^x + h_j^y)/h_j \\ is(h_j^x - h_j^y)/h_j & c - ish_j^z/h_j \end{pmatrix} \end{matrix} , \tag{4.27}$$

where $h_j = \|\vec{h}_j\|$ is the Euclidean norm of $\vec{h}_j$, $c = \cos(\tau h_j/2)$, and $s = \sin(\tau h_j/2)$. These unitary transformations are not very hard to implement: For a given state $|\Psi\rangle$ represented by the 2^N complex coefficients a_n as defined in Eq. (3.8), we have to loop over all $n \in \{0, \ldots, 2^N - 1\}$ with $j_{N-j} = 0$ and transform the coefficients $a_{\ldots 0 \ldots}$ and $a_{\ldots 1 \ldots}$ according to this matrix.

For the two-qubit terms $-\sum_{jk\alpha} J_{jk}^\alpha S_j^\alpha S_k^\alpha$, there are two obvious decompositions. One is the pair decomposition defined by decomposing the sum $\sum_{1\le j<k\le N}$, and the other is the XYZ decomposition defined by decomposing the sum $\sum_{\alpha=x,y,z}$. In this work, we make use of the pair decomposition; see [DM06] for details regarding the XYZ decomposition. Each term in the pair decomposition produces exponentials of $i\tau \sum_\alpha J_{jk}^\alpha S_j^\alpha S_k^\alpha$ which only act on a four-dimensional subspace spanned by $\{|0\rangle_k |0\rangle_j, \ldots, |1\rangle_k |1\rangle_j\}$. Moreover, they couple only two of these states such that they effectively amount to two 2×2 transformations. By analogy with Eq. (4.27), we can work out each of them analytically, yielding

$$e^{i\tau \sum_\alpha J_{jk}^\alpha S_j^\alpha S_k^\alpha} \stackrel{\bullet}{=} \begin{matrix} \\ |0\rangle_k |0\rangle_j \\ |0\rangle_k |1\rangle_j \\ |1\rangle_k |0\rangle_j \\ |1\rangle_k |1\rangle_j \end{matrix} \begin{matrix} \begin{matrix} |0\rangle_k |0\rangle_j & |0\rangle_k |1\rangle_j & |1\rangle_k |0\rangle_j & |1\rangle_k |1\rangle_j \end{matrix} \\ \begin{pmatrix} e^{ia\tau}\cos b\tau & 0 & 0 & ie^{ia\tau}\sin b\tau \\ 0 & e^{-ia\tau}\cos c\tau & ie^{-ia\tau}\sin c\tau & 0 \\ 0 & ie^{-ia\tau}\sin c\tau & e^{-ia\tau}\cos c\tau & 0 \\ ie^{ia\tau}\sin b\tau & 0 & 0 & e^{ia\tau}\cos b\tau \end{pmatrix} \end{matrix} , \tag{4.28}$$

where $a = J_{jk}^z/4$, $b = (J_{jk}^x - J_{jk}^y)/4$, and $c = (J_{jk}^x + J_{jk}^y)/4$. These transformations can be implemented in the same manner as the single-qubit transformations: We have to loop over all $n \in \{0, \ldots, 2^N - 1\}$ with $j_{N-j} = 0$ and $j_{N-k} = 0$, and for each we transform the coefficients $(a_{\ldots 0 \ldots 0 \ldots}, a_{\ldots 1 \ldots 1 \ldots})$ and $(a_{\ldots 0 \ldots 1 \ldots}, a_{\ldots 1 \ldots 0 \ldots})$ accordingly.

Hence the total first-order decomposition $\tilde{U}_1$ of $U = e^{-i\tau H}$ in terms of Eq. (4.8) reads

$$\tilde{U}_1 := \prod_{1\le j<k\le N} e^{i\tau \sum_\alpha J_{jk}^\alpha S_j^\alpha S_k^\alpha} \prod_{j=1}^{N} e^{i\tau\vec{h}_j\cdot\vec{S}_j} \quad . \tag{4.29}$$

As with the CPB decomposition in Eq. (4.25), the specific order of the terms inside each product is not relevant for the approximation itself; it can be chosen freely so as to reach the maximum execution speed using vectorization and parallelization techniques as described in [DMD+07].

4.1.3. Chebyshev polynomial algorithm

A naive alternative approach to calculate the exponential in the time evolution operator $U = e^{-i\tau H}$ would be to use its Taylor expansion and simply truncate the sum. However, this approach exhibits very unsatisfactory numerical instabilities as vividly demonstrated in [ML03]. A much more attractive way would be to use a polynomial expansion of U in terms of powers of H, in which high-order terms are exponentially suppressed. A finite

number of terms would then suffice to make the approximation numerically exact [TK84].

Fortunately, there is an expansion of the exponential in terms of Chebyshev polynomials $T_k(x) = \cos(k \arccos x)$ with coefficients given by integer-order Bessel functions $J_k(z)$ that have exactly this property, namely $J_k(z) \sim (\frac{ez}{2k})^k / \sqrt{2\pi k} \propto z^k / k^{k+1/2}$ for $k \gg 1$ [AS64]. The expansion for $x \in [-1, 1]$ reads [AS64]

$$e^{-izx} = J_0(-z) + 2 \sum_{k=1}^{\infty} i^k J_k(-z)\, T_k(x) \quad . \tag{4.30}$$

To turn this expression into a matrix-valued exponential for U, we make the following considerations: As $T_k(x)$ is a polynomial of order k in x and we strive for a polynomial expansion in powers of H, we have to identify the variable x with the Hamiltonian H. However, due to the domain of the Chebyshev polynomials being $[-1, 1]$, we need to rescale H such that its spectrum does not exceed this interval. As H is Hermitian, this is most effectively done by using the spectral norm $\|H\|_2$ corresponding to the largest absolute eigenvalue of H (see appendix C). Hence the eigenvalues of $H/\|H\|_2$ lie in $[-1, 1]$ as desired. Of course, we might not necessarily be able to compute $\|H\|_2$ exactly without utilizing the costly step of diagonalizing H. Therefore, we will replace it by some easily computable upper bound $\|H\|_2 \leq h_b$ that hopefully approximates the norm well enough. Thus we set $\hat{H} := H/h_b$ which can then take on the role of x in Eq. (4.30). The time evolution operator then reads $U = e^{-i\tau h_b \hat{H}}$, which makes the variable z in Eq. (4.30) correspond to the rescaled time step τh_b. As $\|T_k(\hat{H})\|_2 \leq 1$, this value solely determines the number K of how many terms of the sum over k we need to take into account. For $k > K$, the Bessel function then numerically extinguishes all further contributions. Therefore, it pays off to put enough effort into a tight estimation of h_b because the performance of the algorithm depends on it.

With these points in mind, the approximation to U reads

$$\tilde{U} := J_0(-\tau h_b) + 2 \sum_{k=1}^{K} J_k(-\tau h_b)\, \hat{T}_k(\hat{H}) \quad , \tag{4.31}$$

where the i^k has been absorbed in $\hat{T}_k := i^k T_k$. A nice feature of using the matrix-valued extension of the Chebyshev polynomials is that we can use a forward recursion relation to compute them, in which only the simple action of H on some state needs to be implemented. Thus we find for the modified version $\hat{T}_k$ [PTV+07]

$$\hat{T}_k(\hat{H}) = \begin{cases} \mathbb{1} & (k = 0) \\ i\hat{H} & (k = 1) \\ 2i\hat{H}\hat{T}_{k-1}(\hat{H}) + \hat{T}_{k-2}(\hat{H}) & (k \geq 2) \end{cases} \quad . \tag{4.32}$$

Clearly, the bottleneck is the calculation of these functions applied to the evolving state $|\Psi\rangle$, so we need to know the number of terms K in advance. For this purpose, we have to examine the values of the Bessel functions $J_k(-\tau h_b)$ for all k. As they exhibit oscillatory behavior along the way to zero for high k, the stable way is to use a downward recursion from an asymptotic approximation with eventual renormalization [PTV+07]. In doing so, we store all the values $\{J_k(-\tau h_b)\}_k$ obtained along the way in one large array. Then we can traverse this array from the end and fix the value of K as soon as we find

the first coefficient that is not numerically zero. The only subtlety lies in choosing the right starting point for the downward recursion such that K is really inside. Since this algorithm takes practically no time compared to computing the Chebyshev polynomials in Eq. (4.32), we simply start at $\lfloor 20\,000 + \tau h_b \rfloor$ inspired by the asymptotic behavior of $J_k(z)$ mentioned above.

The advantage of the Chebyshev algorithm is that a single time step τ can be made arbitrarily large without influencing the accuracy, which complements the product-formula algorithm discussed in the last section.

Since the performance of the Chebyshev algorithm depends on the number of terms K and thus on the bound h_b, and this is almost the only point where the implementations of our two models differ, we now turn to deriving such bounds for the two Hamiltonians in question.

CPB model

The central starting point for an upper bound on the norm of the Hamiltonian from Eq. (3.1) is the triangle inequality $\|A+B\|_2 \leq \|A\|_2 + \|B\|_2$. Thus we start from

$$\|H\|_2 \leq \|H_{\mathrm{CPB}}\|_2 + \|H_{\mathrm{Res}}\|_2 + \|H_{\mathrm{JC}}\|_2 + \|H_{\mathrm{CC}}\|_2 \quad . \tag{4.33}$$

The next step is to find the norm of each of the basic constituents of the four Hamiltonians. As the required operator norm yields the maximum absolute value that the operator can attain on any state (see appendix C), we can compute the following norms exactly:

$$\|\hat{n}_i - n_{gi}\|_2 = \left.\begin{cases} N_i + n_{gi} & (n_{gi} \geq 0) \\ N_i - n_{gi} & (n_{gi} < 0) \end{cases}\right\} = N_i + |n_{gi}| \tag{4.34a}$$

$$\|\cos\hat{\varphi}\|_2 = 1 \tag{4.34b}$$

$$\left\|\hat{a}^\dagger \hat{a}\right\|_2 = N_{ph} \tag{4.34c}$$

$$\|a\|_2 = \left\|a^\dagger\right\|_2 = \sqrt{\|a^\dagger a\|_2} = \sqrt{N_{ph}} \quad . \tag{4.34d}$$

Note that it is essential to work in the truncated finite-dimensional Hilbert space given in Eq. (3.4) since otherwise, some of the operators would be unbounded. Using these expressions in conjunction with the triangle inequality results in

$$\|H_{\mathrm{CPB}}\|_2 \leq \sum_{i=0}^{m} \left(|E_{Ci}|(N_i + |n_{gi}|)^2 + |E_{Ji}|\right) \tag{4.35a}$$

$$\|H_{\mathrm{Res}}\|_2 \leq |\omega_r| N_{ph} + \sum_{i=0}^{m} 2|g_i| N_i \sqrt{N_{ph}} \tag{4.35b}$$

$$\|H_{\mathrm{JC}}\|_2 \leq \sum_{i=1}^{m} |E_{JCi}| \tag{4.35c}$$

$$\|H_{\mathrm{CC}}\|_2 \leq \sum_{0 \leq i < j \leq m} |E_{Ci,Cj}|(N_i + |n^L_{Ci,Cj}|)(N_j + |n^R_{Ci,Cj}|) \quad . \tag{4.35d}$$

Depending on the specific application, we can of course omit some of the three coupling Hamiltonians if they are not needed. By summing up all the remaining terms on the

right-hand side, we obtain the desired bound h_b.

Spin model

By analogy with the CPB model, we compute an upper bound on the Hamiltonian using the 2-norm (see appendix C). We have $\left\|S_j^\alpha\right\|_2 = 1/2$ and $\left\|S_j^\alpha S_k^\alpha\right\|_2 = 1/4$ corresponding to the largest absolute eigenvalue of the operators. Using the triangle inequality, we thus obtain

$$\|H\|_2 \leq \frac{1}{4}\sum_{\substack{\langle j,k\rangle \\ \alpha\in\{x,y,z\}}} |J_{jk}^\alpha| + \frac{1}{2}\sum_{\substack{j \\ \alpha\in\{x,y,z\}}} |h_j^\alpha| \quad . \tag{4.36}$$

4.2. Validation of the algorithms

When some physical process is simulated on a computer on the basis of some theory such as quantum theory, two things have to be taken special care of: First, the algorithms have to mathematically agree with the theory that is believed to explain the process. This we have ensured by construction as we developed the algorithms from the basic equation of the theory (i.e. the TDSE) presented in the last section. Second, the actual implementations of the algorithms on a computer must be consistent with each other; i.e. if they are made for the same purpose (such as solving the TDSE), they must not lead to mutually contradictory results. This is the purpose of the present section.

To check this second requirement, we compare the different algorithms in terms of accuracy. Moreover, we validate the mathematical statements regarding the accuracy of the approximations such as the scaling of local errors. This has the advantage of providing us with an estimation of the correct parameters we need to specify for the algorithms (like the proper time step to solve the TDSE); and it will also tell us which algorithm is suited best for which purpose.

The central quantity examined in this section is the *local error*. It is defined by the error that is made after one single time step τ and can be computed from

$$\|\psi(\tau) - \psi_{\text{exact}}(\tau)\| \quad , \tag{4.37}$$

where the symbol ψ stands for a vector of all complex coefficients a_n representing the state in one of the chosen bases (see Eq. (3.5) and Eq. (3.8)). $\psi(\tau)$ then corresponds to the state obtained from the algorithm's approximation $\psi(\tau) = \tilde{U}(\tau)\psi(0)$, and the reference value $\psi_{\text{exact}}(\tau) = e^{-i\tau H}\psi(0)$ comes from the diagonalization of the full Hamiltonian.

We study the dependence of the local error from Eq. (4.37) for a range of different single time steps τ. Each algorithm described in section 4.1 is implemented for both the CPB and the spin model. For the Suzuki product-formula algorithm, we further check the scaling of the local error as proposed in Eq. (4.13) for different orders of approximation, namely $n \in \{1, 2, 4\}$. This is done by fitting straight lines using logarithmic scales on both axes and comparing the slope of the lines with $n + 1$. Besides being a confirmation of the correctness of the implementation, it also helps in tracking down possible errors made in the construction. This is because a higher order n would not show better scaling w.r.t. τ if not all terms in the $U(\tau) - \tilde{U}_n(\tau)$ vanished up to n^{th} order.

Given a bound on the local error in one time step, the global error made after m time steps is then bounded by m times the local error [DeR87]. This helps in estimating the proper time step when we are given the total duration of the simulated time evolution. In practice, the time step can then be further increased as long as the expectation values do not change, on the grounds that, as differences in global phases are measured as well in Eq. (4.37), the actual fidelity of the states is usually much better.

4.2.1. CPB model

The accuracy for the CPB model is evaluated for two systems. The first is a "random" system with all parameters in Eq. (3.1) given by a random double-precision number in $[-1, 1]$, and the second is a "realistic" system with parameters taken from the device properties of typical CPB setups such as the one in [YWY+08]. This means that energy scales over 2π are on the order of $10 - 100\,\mathrm{GHz}$ and charge offsets are around the sweet spot at 0.5. The initial state is set to $|0 \cdots 0\rangle$ in the notation of Eq. (3.5), and the Hilbert space in Eq. (3.4) is defined by $m = 2, N_0 = 4, N_1 = N_2 = 2$, and $N_{\mathrm{ph}} = 3$ such that full diagonalization can still be done in a reasonable amount of time. A system's type is denoted by $t_1 t_2 t_3$ where each $t_i \in \{0, 1\}$ determines which of the coupling Hamiltonians is turned on, i.e., $H = H_{\mathrm{CPB}} + t_1 H_{\mathrm{Res}} + t_2 H_{\mathrm{JC}} + t_3 H_{\mathrm{CC}}$. All examined combinations show the same qualitative behavior; some representative results are shown in Figs. 4.1–4.1.

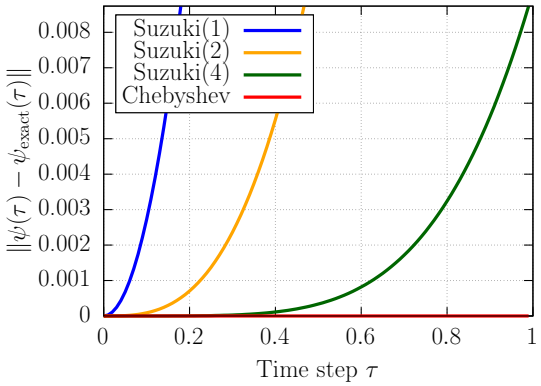

Figure 4.1.: The local error for a random system of two uncoupled Cooper pair boxes shows the proposed polynomial scaling for different orders of the Suzuki product-formula approach. The Chebyshev algorithm performs equally well for all single time steps τ, so it is independent of τ as expected from the discussion in section 4.1.3.

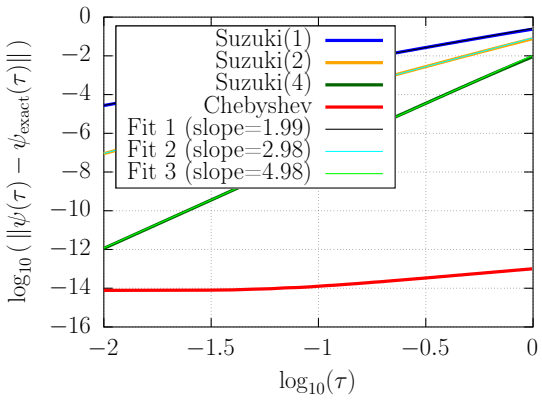

Figure 4.2.: A log-log plot of Fig. 4.1 reveals the exponents of the local errors in the Suzuki algorithm. For each order $n \in \{1, 2, 4\}$, they are around the expected value of $n + 1$ as derived in Eq. (4.13). The Chebyshev algorithm always reaches local errors close to machine precision, so it is the most accurate one to make huge time steps.

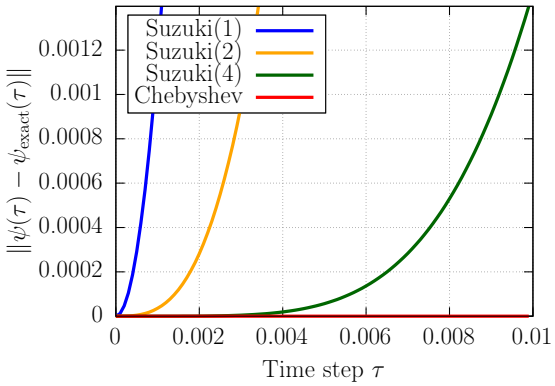

Figure 4.3.: The local error for a system with realistic device parameters (see also section 5.1) that has all couplings turned on. The curves are qualitatively equal to the case without coupling, but the time scales have changed.

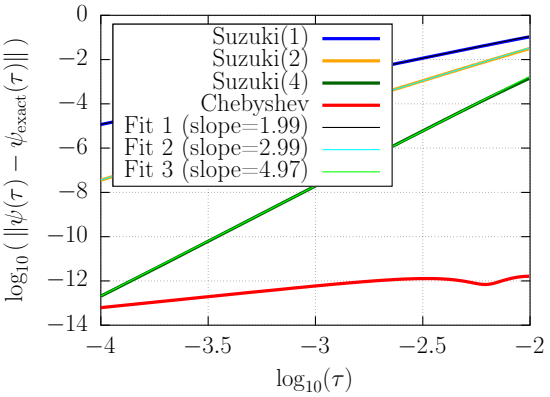

Figure 4.4.: The behavior of the local errors in logarithmic scales resembles the one in Fig. 4.2. We can estimate that a time step of $\tau = 10^{-3}$ is small enough to achieve local errors between 10^{-4} and 10^{-6} in the second-order Suzuki algorithm.

Comparing Fig. 4.1 and Fig. 4.3, we see that the increase of the energy scales by a factor of 100 results in the corresponding reduction of the time steps τ. This makes of course sense since it is the product of H and τ that governs the approximation of the time evolution operator. Judging from the results shown in Fig. 4.4, we conclude that a time step of 10^{-4} to 10^{-3} should be sufficient for the solution of the TDSE. In the realistic system, this corresponds to sub-picoseconds. As mentioned above, the time step can in principle be further increased as long as the results of the expectation values under consideration are not affected. However, as the algorithms are fast enough, we will mainly stick to $\tau = 10^{-4}$. If the energy scales in the Hamiltonian are given in GHz, this corresponds to 0.1 ps. On a notebook with an Intel Core i7 processor having a 6 MB cache and a frequency of 2.1 GHz, 1000 time steps with the Suzuki algorithm take less than a second. The Chebyshev algorithm performs a bit slower, but its time step can be dynamically adjusted to the time-dependence of the parameters in the Hamiltonian. Of course, for larger systems the exact diagonalization is not competitive.

4.2.2. Spin model

The spin model has been evaluated for various numbers of qubits. Exemplarily, we show the local errors for a system of $N = 8$ qubits in Figs. 4.5 and 4.6. The corresponding Hilbert space then has a dimension of $D = 2^8 = 256$, which is not yet a problem for the full diagonalization algorithm.

From the results, we conclude that a solution of the TDSE with $\tau = 0.01$ is accurate enough. A more detailed examination and comparison of the algorithms for the spin model with applications of certain gate sequences is presented in [DM06].

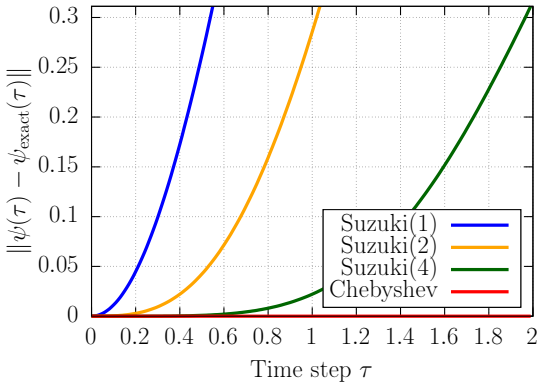

Figure 4.5.: The local error for a spin system of $N = 8$ qubits shows the same qualitative behavior as for the CPB model: The Suzuki algorithms of order n grow as τ^{n+1} (cf. Eq. (4.13)), whereas the Chebyshev algorithm stays close to machine precision for any single time step τ.

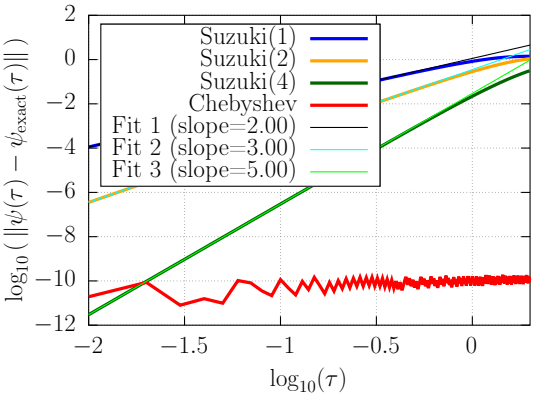

Figure 4.6.: A log-log plot of Fig. 4.5 confirms the expected growths of the local errors in the Suzuki algorithms: The fits reproduce the upper bound on the local error up to 2 decimal digits. For the Chebyshev algorithm, we find that the local error is again practically independent of τ and close to machine precision.

4.3. Visualization methods

The simulation program provides two means of visualizing the solutions of the TDSE for both diagnostic and educational purposes. Each uses the complex coefficients a_n obtained from the solution to compute some physically meaningful quantity. For both the CPB and the spin model, expectation values of local spin operators are computed to represent each qubit as an animated arrow on the Bloch sphere, visualized in a three-dimensional space. For the CPB model, expectation values of number and phase operators can be monitored during the time evolution to see if and by how much the CPBs leak out of their computational subspaces.

4.3.1. 3D visualization on the Bloch sphere

A simple qubit described by a pure state $|\Psi\rangle = a_0 |0\rangle + a_1 |1\rangle$ is quite often geometrically visualized as a three-dimensional arrow on a sphere $\mathbb{S} = \{\vec{x} \in \mathbb{R}^3 : \|\vec{x}\| = 1\}$. Its coordinates can be computed from the expectation value of the spin operator $\vec{S} = \vec{\sigma}/2$, where $\vec{\sigma} = (\sigma^x, \sigma^y, \sigma^z)$ are the Pauli matrices. The calculation yields

$$\langle \vec{S} \rangle = \begin{pmatrix} \mathrm{Re}(a_0^* a_1) \\ \mathrm{Im}(a_0^* a_1) \\ \frac{1}{2}(|a_0|^2 - |a_1|^2) \end{pmatrix} \quad . \tag{4.38}$$

The nice thing about the Bloch sphere representation is that a unitary operation $e^{i\alpha \vec{n} \cdot \vec{S}} \in SU(2)$ can be interpreted as a rotation of $\langle \vec{S} \rangle$ about the axis $\vec{n} \in \mathbb{S}$, where α specifies the angle according to the left-hand rule [NC11] (see also appendix D). Mathematically, this is due to the Lie group of 2×2 special unitaries $SU(2)$ being the universal covering

group of the three-dimensional rotations $SO(3)$ [CF12].

For a product space of several qubits $\mathrm{span}\{|0\rangle, |1\rangle\}^{\otimes N}$, the expectation values corresponding to the spin operators $\vec{S}_k$ $(k = 1, \ldots, N)$ can be evaluated in the same manner, so we obtain for a state $|\Psi\rangle = \sum a_{j_1 \cdots j_N} |j_1 \cdots j_N\rangle$

$$\langle \vec{S}_k \rangle = \sum_{\substack{j_1 \cdots j_N \\ \text{without } j_k}} \begin{pmatrix} \mathrm{Re}(a^*_{j_1 \cdots 0 \cdots j_N} a_{j_1 \cdots 1 \cdots j_N}) \\ \mathrm{Im}(a^*_{j_1 \cdots 0 \cdots j_N} a_{j_1 \cdots 1 \cdots j_N}) \\ \frac{1}{2}(|a_{j_1 \cdots 0 \cdots j_N}|^2 - |a_{j_1 \cdots 1 \cdots j_N}|^2) \end{pmatrix} \quad . \tag{4.39}$$

Of course, since the information contained in these vectors consists of $3N$ real numbers whereas $|\Psi\rangle$ is defined by 2^N complex numbers, this representation does evidently not yield the full information about $|\Psi\rangle$. Indeed, information about correlations between different qubits is lost. The only thing remaining is that the presence of entanglement usually makes the norm of the real vectors $\langle \vec{S}_k \rangle$ smaller than one. For instance, the maximally entangled singlet state $|\Psi^-\rangle = (|01\rangle - |10\rangle)/\sqrt{2}$ has $\langle \vec{S}_1 \rangle = \langle \vec{S}_2 \rangle = (0, 0, 0)$. However, we can still interpret single-qubit rotations $e^{i\alpha \vec{n} \cdot \vec{S}_k}$ and intermediate steps in two-qubit operations accordingly, and thus use the representation to study quantum algorithms.

It should be mentioned that other ideas have been put forth to visualize multi-qubit states and also correctly display information of entanglement, yet there is no known simple generalization of the intuitive Bloch sphere picture [NC11]. What is commonly done for two-qubit systems is to display a state tomography of the corresponding density matrix $\rho \in \mathbb{C}^{4\times4}$. In this representation, ρ is expanded in the Pauli basis $\{\mathbb{1}, \sigma^x, \sigma^y, \sigma^z\}^{\otimes 2}$ of Hermitian matrices. Due to the properties of ρ, the 16 expansion coefficients are always real and thus usually shown in bar diagrams. We will get back to this expansion in section 4.4.1. Another interesting idea of visualizing two-qubit states on spheres has been presented in [Rig09]. For the purpose of this thesis, however, we stick to the simple Bloch sphere representation.

The graphical user interface can be used to program a certain sequence of gates by specifying the corresponding parameters of the Hamiltonian. During the time evolution, the program computes and stores the expectation values of the CPB states given in Eq. (3.5) and the spin states given in Eq. (3.8) according to Eq. (4.39), possibly including a user-specified change of basis. Afterwards, the motion of the arrows can be investigated in a three-dimensional setting with the opportunity to step through individual gate sequences and verify the programmed algorithm. The open source high-performance 3D engine Irrlicht [GAC+05] was used to render the three-dimensional scene.

4.3.2. Monitoring the non-computational states

For a given sequence of gates for the CPB model, the application provides a means to monitor the occupation of all energy levels in some user-specified basis. This is done by animated bar diagrams that show the evolution of the probabilities to measure a specific number of Cooper pairs on the qubit. If the computational states are given by the charge states $|0\rangle$ and $|1\rangle$, for instance, it can be used to see whether the CPB leaks out of the computational subspace.

For the state $|\Psi\rangle$ given by Eq. (3.5), the probabilities are obtained from the expectation

values of the corresponding projectors. A straightforward calculation yields

$$p(n_0) = \langle\Psi| \left(|n_0\rangle\langle n_0|_0\right) |\Psi\rangle = \sum_{n_1 \cdots n_m k} |a_{n_0 \cdots n_m k}|^2 \tag{4.40a}$$

$$p(n_i) = \langle\Psi| \left(|n_i\rangle\langle n_i|_i\right) |\Psi\rangle = \sum_{\substack{n_0 \cdots n_m k \\ \text{without } n_i}} |a_{n_0 \cdots n_m k}|^2 \tag{4.40b}$$

$$p(k) = \langle\Psi| \left(|k\rangle\langle k|_{\text{Res}}\right) |\Psi\rangle = \sum_{n_1 \cdots n_m} |a_{n_0 \cdots n_m k}|^2 \tag{4.40c}$$

$$p(\varphi_0) = \langle\Psi| \left(|\varphi_0\rangle\langle\varphi_0|_0\right) |\Psi\rangle = \frac{1}{2N_0+1} \sum_{n_0 \tilde{n}_0} e^{i(n_0 - \tilde{n}_0)\varphi_0} \sum_{n_1 \cdots n_m k} a^*_{n_0 \cdots n_m k} a_{\tilde{n}_0 \cdots n_m k} \quad . \tag{4.40d}$$

The last expression corresponds to the Fourier transform given in Eq. (2.14). Note that, in the truncated finite-dimensional Hilbert space in Eq. (3.4), this Fourier transform has been replaced by its discrete counterpart. We will need this particular expression in the analysis of the model corresponding to the Josephson-inductive coupling [YWY+08]. The population of photons in the cavity given by Eq. (4.40c) will be useful in the study of the transmon quantum computer in section 5.2.

4.4. Effective Hamiltonians

Many systems proposed for quantum computing rely on additional degrees of freedom to couple the qubits, such as the resonator in circuit QED setups (see section 2.3) or the additional Josephson junction mentioned in section 2.2.3. These degrees of freedom are often described by a subspace of the complete Hilbert space. To examine the quantum computing system theoretically, one needs to find a way to eliminate these degrees of freedom such that a bare effective qubit-qubit interaction remains. This means that one seeks a procedure to derive an effective Hamiltonian from the total Hamiltonian (preferably expressed in the spin space spanned by the Pauli matrices, such as Eq. (3.7)). This can then be used to investigate the influence of external control parameters such as voltages or magnetic fields, and to assess the system's potential to realize multi-qubit gates.

Obviously, there are many more or less rigorous ways to derive such effective spin Hamiltonians. Some rely on simple Taylor expansions, and some make use of various kinds of perturbation theory. A straightforward approach is to simply write down the partial differential equations for each expansion coefficient of an arbitrary state, and extract the effective Hamiltonian generating these equations to a desired order (cf. [Par06]). Other common approaches include time-averaging [JJ07], adiabatic-elimination [PRN+14], and the Schrieffer-Wolff transformation [SW66]. This last method is a special version of degenerate perturbation theory. It is based on direct similarity transformations of the original Hamiltonian, thereby diagonalizing the Hamiltonian to a desired order. The method has been frequently applied to multi-qubit systems and there exist rigorous statements about the precision and the range of validity of the effective Hamiltonians [BDL11].

One purpose of the present software is to examine and test such methods of obtaining effective Hamiltonians. Fortunately, as we obtain the system's time evolution by solving the TDSE, we have access to the data set of the total density matrices $\{\rho(t)\}$ for

all times. By tracing out the additional degrees of freedom, we can obtain the reduced density matrices in the computational subspace. Assuming that the subsystem can really be described by an effective Hamiltonian living in the subspace only, these reduced matrices should more or less agree with the time evolution of the initial subsystem's state under an effective Hamiltonian H_{eff}. Thus by fitting an arbitrary time-independent Hamiltonian through unitary evolution to the data set of reduced density matrices, we can assess whether such an effective Hamiltonian exists and to which degree the evolution can be effectively described by it. Furthermore, we will obtain its expansion coefficients in the basis of Pauli matrices. This procedure is described in detail in the next section, followed by a brief outline of the measures used to estimate its success.

4.4.1. Procedure

We start from a bipartite system in some state $|n_1\rangle \otimes |n_2\rangle$, where n_1 and n_2 enumerate the states including the two-qubit subspace. It is coupled to an external system 0, whose initial state is labeled $|0\rangle_0$. This system can be one single unit such as a resonator or another Josephson junction, or some greater entity such as a purifying system [NC11] or an environment. So the initial density matrix of the compound system is given by

$$\rho(0) = |0\rangle\langle 0|_0 \otimes \rho_{12}(0) = |0\rangle\langle 0|_0 \otimes |n_1 n_2\rangle\langle n_1 n_2| \quad , \tag{4.41}$$

describing a pure state. In quantum theory, the total system undergoes a unitary time evolution $U = U(t, 0)$, i.e.

$$\rho(t) = U\left(|0\rangle\langle 0|_0 \otimes |n_1 n_2\rangle\langle n_1 n_2|\right) U^\dagger \quad . \tag{4.42}$$

All expectation values for local observables $A = A_{12}$ living only in the bipartite subsystem can then be computed through the reduced density matrix $\rho_{12}(t) = \operatorname{Tr}_0 \rho(t)$, since we have $\langle A\rangle(t) = \operatorname{Tr}(\rho(t)A) = \operatorname{Tr}_{12}((\operatorname{Tr}_0 \rho(t))A) = \operatorname{Tr}_{12}(\rho_{12}(t)A)$. The time evolution of this reduced density matrix can always be written as [NC11]

$$\rho_{12}(t) = \operatorname{Tr}_0 \rho(t) = \sum_{n_0} M_{12}^{n_0}\, \rho_{12}(0)\, M_{12}^{n_0\dagger} = \sum_{n_0} M_{12}^{n_0}\, |n_1 n_2\rangle\langle n_1 n_2|\, M_{12}^{n_0\dagger} \quad , \tag{4.43}$$

where $M_{12}^{n_0} = {}_0\langle n_0|\, U\, |0\rangle_0$ are the so-called Kraus operators satisfying $\sum_{n_0} M_{12}^{n_0\dagger} M_{12}^{n_0} = \mathbb{1}$ [KBD+83]. Here, n_0 enumerates all states of the additional system. From Eq. (4.43), we can see that the final state of the bipartite system is, in general, a mixed state. In fact, it is only pure if the evolution of the subsystem is unitary, i.e., there is an effective unitary transformation U_{eff} such that $M_{12}^0 = U_{\text{eff}}$ and $M_{12}^{n_0\neq 0} = 0$. However, in many common cases in quantum information technology, the coupling to system 0 is weak or the duration of the evolution is short, and the reduced system remains in an almost pure state (meaning that the purity $\operatorname{Tr} \rho_{12}(t)^2 \lesssim 1$). Alternatively, the system can be entangled during the evolution such that it looks mixed in the reduced system (e.g. $\operatorname{Tr} \rho_{12}(\tilde{t})^2 < 1$ for some $\tilde{t} \in (0, t)$), but it might eventually return to a pure state in either reduced system. Then we can still find an approximately unitary operator $U_{\text{eff}} \approx M_{12}^0$, or equivalently an approximately Hermitian Hamiltonian H_{eff}, describing the system's effective evolution between the states $\rho_{12}(t')$ for which $\operatorname{Tr} \rho_{12}(t')^2 = 1$. Note that the purity of the total density matrix is always $\operatorname{Tr} \rho(\tilde{t})^2 = 1$ since the total time evolution given by U is unitary.

If the object mediating the coupling between the qubits is not an explicit part of the

Hilbert space (such as a capacitor or an interaction through higher non-computational levels), the procedure can of course still be applied to assess effective Hamiltonians. In that case, we simply omit taking the trace over system 0 after the time evolution.

We obtain the effective Hamiltonian from a nonlinear optimization using the data generated during the time evolution. If the fit succeeds (see the next section for validation measures) and the effective Hamiltonian is Hermitian, we know that such an effective description exists.

Since we are looking for an effective evolution in the two-qubit subspace (ultimately to find and check proposals for various two-qubit gates), we first project the reduced density matrices onto the two-qubit subspace. If this subspace corresponds to $n_1, n_2 \in \{0, 1\}$, this means that we compute the projection

$$\rho_{12}^{\text{comp}}(t) = \sum_{n_1,n_2,n_1',n_2'=0}^{1} |n_1 n_2\rangle\langle n_1 n_2|\, \rho_{12}(t)\, |n_1' n_2'\rangle\langle n_1' n_2'| \quad . \tag{4.44}$$

Of course, if the computational states are defined in another basis, we need to adjust the projectors accordingly. Hence, if an effective unitary evolution in the two-qubit subsystem exists, there is a solution to the set of equations

$$\rho_{12}^{\text{comp}}(t+\tau) \stackrel{!}{=} e^{-i\tau H_{\text{eff}}(\{h_{ij}\})}\ \rho_{12}^{\text{comp}}(t)\ e^{i\tau H_{\text{eff}}(\{h_{ij}\})} \quad , \tag{4.45}$$

for various times t and different initial states $\rho_{12}(0)$. In Eq. (4.45), h_{ij} are parameters defining the effective Hamiltonian. Since ρ_{12}^{comp} describes two qubits, the space of Hamiltonians has 16 dimensions, so we have to find 16 such parameters. For convenience, we define these parameters from the expansion of H_{eff} in the Pauli basis $(\sigma^0 = \mathbb{1}, \sigma^1 = \sigma^x, \sigma^2 = \sigma^y, \sigma^3 = \sigma^z)^{\otimes 2}$:

$$H_{\text{eff}} = \sum_{i,j=0}^{3} h_{ij}\, \sigma^i \otimes \sigma^j \quad . \tag{4.46}$$

This choice of basis has the advantage that we can immediately infer the induced two-qubit gate from h_{ij}. Furthermore, for a Hermitian Hamiltonian, we know that $h_{ij} \in \mathbb{R}$. By allowing for complex coefficients in the fit, the magnitude of the imaginary parts of h_{ij} tells us whether the evolution in the two-qubit subspace was really unitary or if there has been decoherence or leakage into other levels. This reflects the fact that the final state in Eq. (4.43) had a small purity.

So the nonlinear optimization problem solved on the computer is given by the minimization procedure

$$\min_{\{h_{ij}\}} \|\mathbf{Y} - \mathrm{F}(\{h_{ij}\}, \mathbf{X})\|_F^2 \quad , \tag{4.47}$$

where

$$\mathbf{Y} = \begin{pmatrix} \rho^{\text{comp}}_{12,|\psi_1\rangle}(\tau) \\ \vdots \\ \rho^{\text{comp}}_{12,|\psi_r\rangle}(m\tau) \end{pmatrix}, \qquad \mathbf{X} = \begin{pmatrix} \rho^{\text{comp}}_{12,|\psi_1\rangle}(0) \\ \vdots \\ \rho^{\text{comp}}_{12,|\psi_r\rangle}((m-1)\tau) \end{pmatrix},$$

$$\mathrm{F}(\{h_{ij}\}, \mathbf{X}) = \begin{pmatrix} e^{-i\tau H_{\text{eff}}(\{h_{ij}\})}\ \rho^{\text{comp}}_{12,|\psi_1\rangle}(0)\ e^{i\tau H_{\text{eff}}(\{h_{ij}\})} \\ \vdots \\ e^{-i\tau H_{\text{eff}}(\{h_{ij}\})}\ \rho^{\text{comp}}_{12,|\psi_r\rangle}((m-1)\tau)\ e^{i\tau H_{\text{eff}}(\{h_{ij}\})} \end{pmatrix}.$$

Since the matrix norm in the residual is the Frobenius norm, this is essentially a nonlinear least squares fit of complex parameters. Note that the precise order of rows in $\mathbf{X}$ and $\mathbf{Y}$ does not matter as long as every row in $\mathbf{Y}$ represents the time evolution of the corresponding row in $\mathbf{X}$. The integer m denotes the number of intermediate time steps for which data is generated. The additional subscript $k \in \{1, \ldots, r\}$ for $|\psi_k\rangle$ on the reduced density matrices denotes the corresponding initial state of $\rho_{12}(0)$ in Eq. (4.41), selected from a set of r different initial states. In practice, we usually set $r = 12$ and choose $|\psi_k\rangle$ from the eigenbasis $|ij\rangle$ of σ_1^z and σ_2^z, the eigenbasis $|\pm\pm\rangle$ of σ_1^x and σ_2^x, and the four maximally entangled states $|\Phi^\pm\rangle = (|00\rangle \pm |11\rangle)/\sqrt{2}$ and $|\Psi^\pm\rangle = (|01\rangle \pm |10\rangle)/\sqrt{2}$. We can of course include the evolution of other initial states as well; we only need to make sure that the supplied data in $\mathbf{X}$ and $\mathbf{Y}$ yields enough information about the effective evolution to reconstruct H_{eff}.

Note that τ in Eq. (4.47) is not necessarily equal to the time step that is chosen to solve the TDSE. It can be made arbitrarily large to allow intermediate interactions through higher non-computational levels or entanglement between the systems, or even a time-dependence of the effective Hamiltonian. But in the end, if we study a proposed scheme that can in theory generate a specific gate, we should be able to see the corresponding effect in the resultant h_{ij}.

4.4.2. Evaluation

The fitting procedure given by Eq. (4.47) is, of course, a complicated nonlinear minimization problem. Hence the results will depend highly on the initial values for the algorithm. Furthermore, there is no theoretical guarantee that it really converges to a global minimum, and if it does not, we have no definite way of knowing whether no effective Hamiltonian exists or the fit just did not find one.

To overcome these issues, we always start the fit from an effective Hamiltonian that has been analytically obtained using one of the theoretical methods described above. That is to say, we take the initial values for the fitting algorithm directly from the form of the effective Hamiltonian predicted by the theory.

If the fit has been successful, we use the found effective Hamiltonian to recompute the time evolution in Eq. (4.45) for all t and take the norm of the difference from the original $\rho_{12}^{\text{comp}}(t+\tau)$. This is mathematically equivalent to taking the norm of the residuals from the nonlinear fit in Eq. (4.47). As a reference norm, we use the bare residuals for the case $H_{\text{eff}} = 0$ when no evolution takes place. This allows us to find the degree of how much better the Hamiltonian evolution can describe the data. So we define the *failure rate* γ

as

$$\gamma = \frac{\|\mathbf{Y} - \mathrm{F}(\{h_{ij}\}, \mathbf{X})\|_F^2}{\|\mathbf{Y} - \mathbf{X}\|_F^2} \quad . \tag{4.48}$$

A failure rate $\gamma \ll 1$ then tells us that the evolution can be well described in terms of the effective Hamiltonian in the two-qubit space, whereas $\gamma \approx 1$ implies the opposite.

As a proof of concept, we used the spin model from Eq. (3.7) to solve the TDSE and generate data sets $\{\rho_{12}^{\mathrm{comp}}(t)\}$ for 20 to 80 different times t. The parameters were chosen to generate single-qubit X and Z rotations (meaning only $h_j^{x/z} \neq 0$), and two-qubit couplings of the type XX, YY, and ZZ (meaning only $J_{12}^{x/y/z} \neq 0$). The initial states were set to either $|ij\rangle$ for all $i, j \in \{0, 1\}$, or $|ab\rangle$ for all $a, b \in \{+, -\}$. Then we used the procedure described in the previous section to reconstruct the Hamiltonian from the density matrices. In each experiment, the procedure was able to reconstruct H exactly (up to numerical precision), achieving failure rates γ between 10^{-9} and 10^{-12}. Seeing this as a demonstration of principle, we now proceed to apply the simulation software including this method to study some proposed gate realizations in superconducting qubit networks in the following chapter.

5. Quantum computing systems

In the previous chapters, we have given an overview of the theory regarding Cooper pair box qubits (CPB qubits) and introduced the computational tools we have developed to study them. Thus we are now ready to investigate a few selected systems that have been proposed for quantum computer hardware and have already partly been implemented.

The regimes which CPBs are operated in can be divided into the charge and the transmon regime (see section 2.3). Both can be classified by their ratios of charging energy E_C to Josephson energy E_J and the preferred basis used for computational operations. Since the charge regime is the traditional regime, we first examine two representatives with different couplings, as proposed in the literature. Then we turn our focus on transmon qubits and, in particular, look at recent developments in the refinement of single-qubit and two-qubit gates.

5.1. Charge quantum computer

In the charge regime $E_C \gg E_J$, the computational states are usually chosen to be the charge states or their symmetric and antisymmetric superpositions. To operate a quantum computer with more than one qubit, however, we have to additionally define the way of coupling the qubits. Two proposals, namely a capacitive coupling through the charges on each CPB and an inductive coupling via an additional Josephson junction, are studied in this section.

5.1.1. Charge qubits with capacitive coupling

Typical gate proposals for multi-qubit systems traditionally require either tuning the individual qubits (by e.g. some external flux) or tuning the intermediate circuitry to achieve coupling. In 2005, a novel scheme has been presented based on setups that have both fixed-frequency qubits and fixed coupling elements [RBD05], using only microwave signals to control and couple the qubits. A significant experimental representative of this class is the so-called cross-resonance gate [RD10; CCG+11] that is now one of the popular schemes for transmon qubits [SMC+16]. Its underlying two-qubit interaction controlled by microwave signals has initially been proposed for capacitively coupled charge qubits [Par06; LCP08]. Hence, before coming to the cross-resonance gate in the next section, we use this scheme as a first application of the simulation software.

The system is characterized by a Hamiltonian describing two CPBs and a capacitive coupling between them [Par06], i.e.

$$H = \sum_{i=1}^{2} (E_{Ci}(\hat{n}_i - n_{gi})^2 - E_{Ji}\cos\hat{\varphi}_i) + E_m(\hat{n}_1 - n_{g1})(\hat{n}_2 - n_{g2}) \quad . \tag{5.1}$$

By comparing this Hamiltonian with the capacitive coupling Hamiltonian of the CPB model in Eq. (3.1), we can identify the only nonzero parameters $E_{C1,C2} = E_m$, $n^L_{C1,C2} = n_{g1}$, $n^R_{C1,C2} = n_{g2}$. Since we need two qubits in the charge basis, we set the parameters of the Hilbert space in Eq. (3.4) to $m = 2, N_0 = 0, N_1 = N_2 = 2$, and $N_{\text{ph}} = 0$, such that each CPB is described in a space spanned by the five charge states $|n = -2\rangle, \ldots, |n = 2\rangle$. By monitoring the populations during the time evolutions, we verified that this Hilbert space is large enough to describe all relevant dynamics of the system.

For the device parameters, we take the energies suggested in [LCP08]. They are expressed in terms of an effective coupling strength $\omega_{xx} = 2\pi \times 0.02\,\text{GHz}$. With $\hbar = 1$, we thus set $E_{J1} = 201\omega_{xx}, E_{J2} = 199\omega_{xx}$, and $E_m = 4\omega_{xx}$. Additionally, we set $E_{C1} = E_{C2} = 2\pi \times 100\,\text{GHz}$, so $E_J/E_C \approx 0.04$, which should make the CPBs operate in the charge regime. As motivated in section 4.2, we set the time step to solve the TDSE to 0.1 ps.

The charge qubits are each operated at their sweet spots (a.k.a. codegeneracy point), so we set $n_{g1} = n_{g2} = 1/2$. Each qubit's dynamics should then be contained within the two-dimensional subspace spanned by the charge states $|0\rangle$ and $|1\rangle$. Thus, w.r.t. the basis $|\pm\rangle = (|0\rangle \pm |1\rangle)/\sqrt{2}$, the system is said to be well described by the effective Hamiltonian [Par06]

$$H^{\text{eff}} = -\frac{E_{J1}}{2}\sigma_1^z - \frac{E_{J2}}{2}\sigma_2^z + \omega_{xx}\sigma_1^x\sigma_2^x \quad . \tag{5.2}$$

The first thing to check is whether this effective spin Hamiltonian can reproduce the free evolution of the system over a time span of 30 ns, which is the gate duration of the two-qubit gate examined shortly. We do this by applying the procedure outlined in section 4.4 to assess effective Hamiltonians. The parameters for Eq. (4.47) are set to $\tau = 0.001$, $m = 30000$, and $r = 12$. For the expansion coefficients h_{ij} of the resultant effective Hamiltonian in the Pauli basis (see Eq. (4.46)), the procedure yields

$$h_{30}/2\pi = -2.0098\,\text{GHz} \tag{5.3a}$$
$$h_{03}/2\pi = -1.9898\,\text{GHz} \tag{5.3b}$$
$$h_{11}/2\pi = \quad 0.0200\,\text{GHz} \quad , \tag{5.3c}$$

together with a failure rate of $\gamma = 1.56632 \times 10^{-8}$ (see Eq. (4.48)). Since these numbers match the coefficients in Eq. (5.2) up to two decimal digits, we find that the system is indeed well described by this effective Hamiltonian.

It is worth listing the approximations we have validated for this case at the codegeneracy point: First, the superposition of charge states $|\pm\rangle$ is a valid approximation to the eigenstates of the uncoupled Hamiltonian; and second, the qubits do not leak out of the two computational subspaces.

Next, we consider a scheme for the realization of the CNOT gate given by Eq. (3.9) between both qubits. Since the computational basis for the Hamiltonian in Eq. (5.2) is given by $|\pm\rangle$, but we are usually familiar with the action of CNOT on basis states labeled $|0\rangle$ and $|1\rangle$, we now relabel $|+\rangle \mapsto |0\rangle$ and $|-\rangle \mapsto |1\rangle$.

The proposed scheme for the CNOT operation relies on using only microwave driving of the individual qubits through the capacitively coupled voltage sources V_{gi}. As they enter the Hamiltonian via the offset charges n_{gi}, we model their explicit time-dependence

as suggested in [Par06], i.e.

$$n_{g1}(t) = \frac{1}{2} + w_1(t)\cos(\omega t + \phi_1) \tag{5.4a}$$

$$n_{g2}(t) = \frac{1}{2} + w_2(t)\cos(\omega t + \phi_2) \quad , \tag{5.4b}$$

where ϕ_1 and ϕ_2 are arbitrary phases and the microwave frequency $\omega = 200\omega_{xx}$ lies exactly between the two Josephson energies of the qubits. The effective Hamiltonian given by Eq. (5.2) then needs to be updated to include the new sinusoidal drivings according to

$$H^{\text{eff}} \mapsto H^{\text{eff}} + E_{C1} w_1(t)\cos(\omega t + \phi_1)\,\sigma_1^x + E_{C2} w_2(t)\cos(\omega t + \phi_2)\,\sigma_2^x \quad . \tag{5.5}$$

For an efficient realization of the CNOT gate, proper pulse shapes $w_1(t)$ and $w_2(t)$ are given in [LCP08], resulting from simulated annealing. They are defined as 30 ns-long continuous piecewise linear functions satisfying $0 \leq w_i(t) \leq 10\omega_{xx}/E_{Ci}$ as well as the boundary conditions $w_i(0) = w_i(30\,\text{ns}) = 0$, and the phases are set to $\phi_1 = -0.2\pi$ and $\phi_2 = 0.07\pi$ (see Fig. 5.1 for plots of the pulses).

A time evolution of the system for the initial state $|10\rangle$ and the spin singlet $|\Psi^-\rangle = (|01\rangle - |10\rangle)/\sqrt{2}$ is shown in Fig. 5.1 and Fig. 5.2, respectively. In both cases, the CNOT gate is properly carried out. This is also confirmed by the corresponding animations on the Bloch sphere (see appendix F): For the initial state $|10\rangle$, both spins start and end parallel to the z-axis, with the second spin flipped after the evolution. For the state $|\Psi^-\rangle$, the evolution starts with both spin vectors having magnitude zero, and it ends with the first spin pointing along the negative x-axis (state $|-\rangle$) and the second spin pointing along the negative z-axis (state $|1\rangle$).

To evaluate the operation a bit more quantitatively, we compute the gate fidelity for the same twelve initial states that we also selected for the optimization problem (cf. Eq. (4.47)). For the gate fidelity, we use the common definition from [Nie02]

$$F_g = \frac{d\,\text{Tr}(\rho\rho_{\text{ideal}}) + 1}{d+1} \quad , \tag{5.6}$$

where $d = 2^2 = 4$ is the dimension of the computational Hilbert space, ρ is the density matrix obtained after the quantum operation, and ρ_{ideal} is the ideal density matrix computed from the unitary gate $U_g = \text{CNOT}$ applied to the initial state $|\psi\rangle$, i.e. $\rho_{\text{ideal}} = U_g\,|\psi\rangle\langle\psi|\,U_g^\dagger$.

We consider a sequence of nine successive CNOT gates. Since in theory $\text{CNOT}^n = \text{CNOT}$ for n odd, we evaluate Eq. (5.6) after every second gate starting from $n = 1$ to see how the gate fidelity behaves in successive operations. The results are shown in Fig. 5.3.

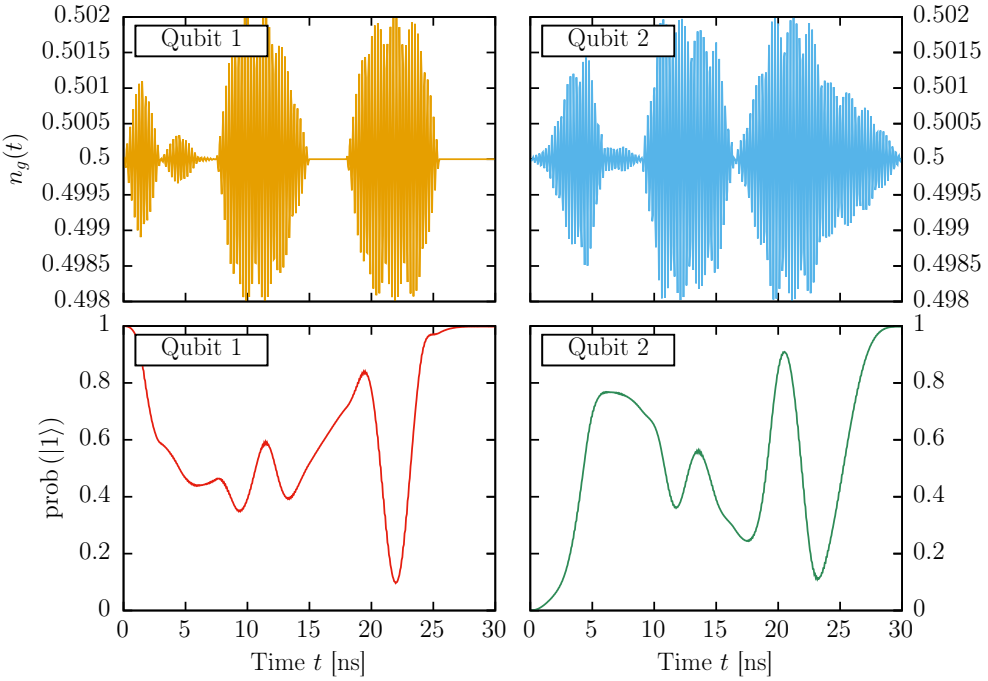

Figure 5.1.: Time evolution of the operation CNOT $|10\rangle = |11\rangle$. The upper two plots show the voltage pulses applied to both qubits, defined by the envelopes $w_{1/2}(t)$ in Eq. (5.4a) and Eq. (5.4b). The lower two plots show the time evolution of the probability to measure the qubit in the state $|1\rangle$. As expected, the first qubit starts and ends in $|1\rangle$, while the second qubit undergoes a bit flip from $|0\rangle$ to $|1\rangle$.

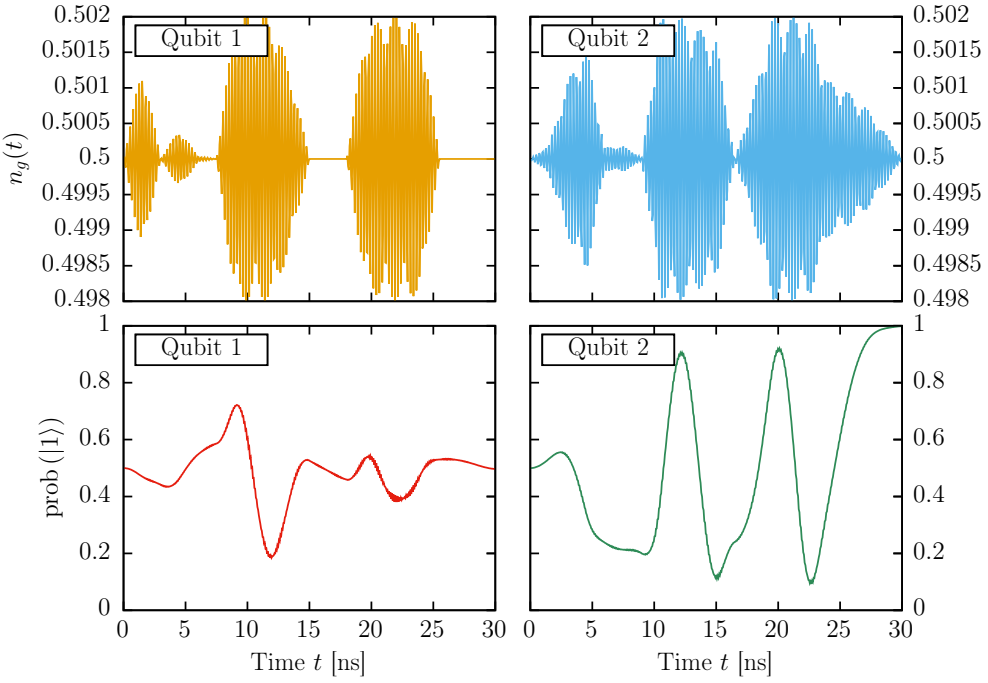

Figure 5.2.: Time evolution of the CNOT gate applied to the singlet $|\Psi^-\rangle$ (labeling as in Fig. 5.1). Since CNOT $|\Psi^-\rangle = |-1\rangle$, the first qubit starts and ends in a superposition of $|0\rangle$ and $|1\rangle$ while the second qubit evolves into $|1\rangle$.

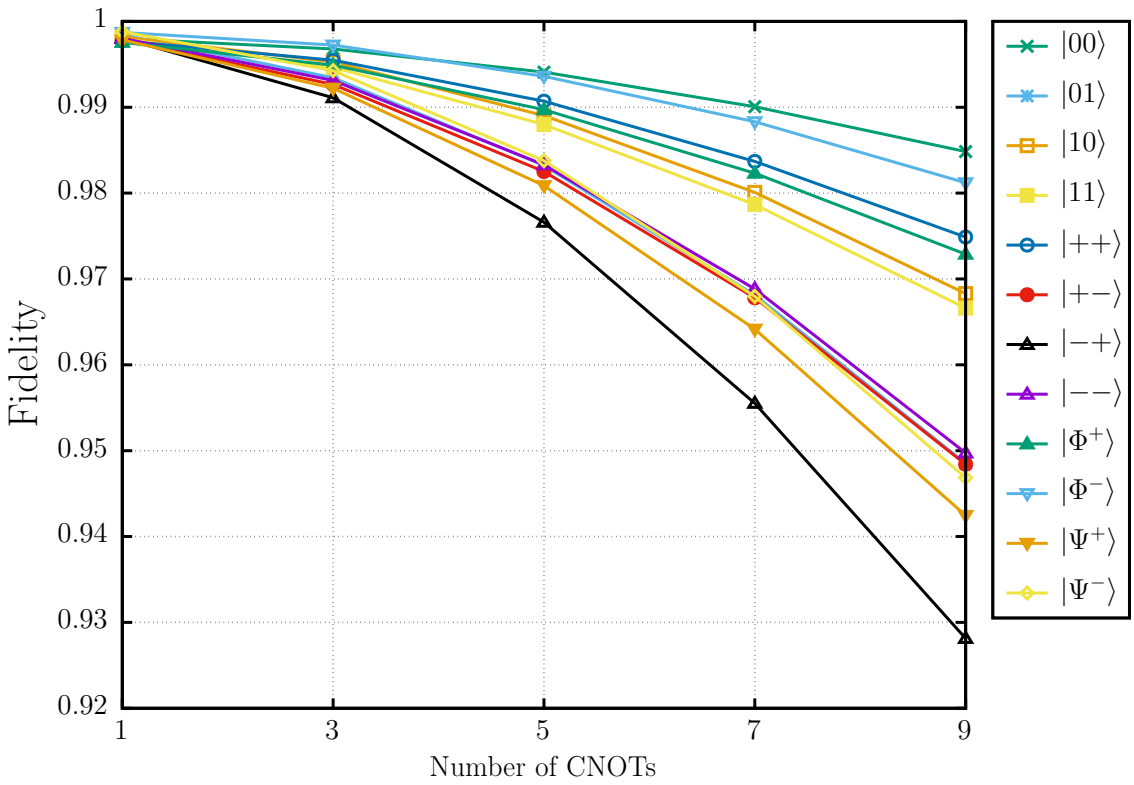

Figure 5.3.: Gate fidelity of CNOT according to Eq. (5.6) during nine successive operations, starting from various initial states corresponding to different colors in the plot. For one application, all evolutions have a fidelity above 99.7%. After nine applications, all fidelities are still above 92%. Observe also that even if successive gate applications on the basis states are fine, this does not necessarily hold for superposition states. Interestingly, the best state $|00\rangle$ and the worst state $|-+\rangle$ are actually both eigenstates of CNOT.

The gate fidelities for one application are above 99.7% for all initial states under consideration. This agrees with the results stated in [LCP08], where the RWA has already been made before evaluating the gate fidelities. Thus the RWA does not seem to influence the success of the gate much in this case. Even after nine successive applications, the fidelities are still above 92%, with the best performance achieved for the initial state $|00\rangle$.

We have to keep in mind, though, that the gate fidelity defined by Eq. (5.6) is actually a rather kind measure. Observing the states of the spin vectors on the Bloch sphere, we find that for $F_g \approx 92\%$, a single spin can point away from the x-axis by an angle of more than 35° (see also the example in Fig. F.2 in appendix F). Furthermore in experiments, it has proven difficult to keep charge qubits coherent over a longer time span due to charge noise [KYG+07]. Nevertheless, we observe that the scheme under investigation, which forms the basis of the cross-resonance gate, performs reasonably well w.r.t. Hamiltonian dynamics.

5.1.2. Charge qubits with Josephson-inductive coupling

Having studied a scheme of static coupling without external flux-tuning in the previous subsection, we now also briefly investigate a scheme for tunable coupling proposed in 2003 [YTN03] and experimentally studied in 2008 [YWY+08]. The idea is to use an additional Josephson junction closing the branches between split Cooper pair boxes such that the

coupling can be tuned by an external flux. The corresponding circuit has already been introduced as an application of the circuit quantization rules in section 2.2.3 (see Fig. 2.6).

In [YTN03], the authors start from a circuit equivalent to the one in Fig. 2.6 for $m = 2$ and $E_{JCi} = E_{Ji}$. After making a few approximations, they arrive at the circuit Hamiltonian

$$H = \sum_{i=1}^{2}(E_{Ci}(\hat{n}_i - n_{gi})^2 - E_{Ji}\cos\hat{\varphi}_i - E_{Ji}\cos(\hat{\varphi}_0 - \hat{\varphi}_i + \phi_{\text{ex}})) - E_{J0}\cos\hat{\varphi}_0 \quad , \tag{5.7}$$

where the notation has been adjusted to the CPB model given by Eq. (3.1). This Hamiltonian differs from the one obtained in the full circuit analysis (see Eq. (2.48)) in that the cross-capacitive terms are missing, but both Hamiltonians coincide if E_{C0} is negligible to all other energy scales. Therefore, we study two Hamiltonians in this section:

- H_{ideal} given by Eq. (2.48) without capacitive coupling (i.e., without the second line)
- H_{real} given by Eq. (2.48)

For H_{ideal}, we take the parameters estimated in [YTN03] since they are what their derivation is based on. For H_{real}, we consider the slightly different energies measured in the actual experiment [YWY+08]. In both cases, the charge qubits are operated at the codegeneracy point $n_{g1} = n_{g2} = 1/2$. A summary of the device parameters is given in Tab. 5.1.

Table 5.1.: Device parameters for the two Hamiltonians H_{ideal} and H_{real}. The energies of the first setting are chosen according to the theoretical estimation given in [YTN03]. In particular, we set $E_{C0}/2\pi = 0.01\,\text{GHz}$ to make H_{ideal} coincide with the Hamiltonian in Eq. (5.7). The second setting is taken directly from the measurement of sample A in the corresponding experiment in [YWY+08].

	$E_{Ci}/2\pi$ (GHz)			$E_{Ji}/2\pi$ (GHz)		
	$i=0$	$i=1$	$i=2$	$i=0$	$i=1$	$i=2$
ideal	0.01	100	100	13.13	2.63	2.63
real	8.8	114	108	23	5.7	5.7

The simulation is carried out with the same time step and the same Hilbert space as before, the only difference being the new subspace for the coupling junction that we define by $N_0 = 20$. The reason to include $2N_0+1 = 41$ different charge states for this Josephson junction lies in the fact that $E_{J0} \gg E_{C0}$, so we need to make sure that all dynamics is contained within this space and boundary effects do not play a role. Essentially, this implies that $p(n_0)$ given by Eq. (4.40a) must go to zero for $|n_0| \lesssim N_0$. Furthermore, $p(\varphi_0)$ given by Eq. (4.40d) should remain a smooth function throughout the time evolution. The coupling junction is always initialized in its respective ground state. Mathematically, this state corresponds to the transmon ground state $|m = 0\rangle_0$ (see section 2.3.1) and is thus completely characterized by the energies E_{C0} and E_{J0}. For the qubits, we prepare various initial states from the two-qubit subspace $\bigotimes_{i=1}^{2} \text{span}\{|n_i = 0\rangle, |n_i = 1\rangle\}$.

The result of the derivation in [YTN03] is that for H_{ideal}, a coupling between both qubits can be tuned by the external flux ϕ_{ex}. To obtain this result, the authors first apply a variable transformation to Eq. (5.7) inspired by flux quantization. Then by using current conservation and a series expansion in $\hat{\varphi}_0$ and the parameters $\eta_i = E_{Ji}/2E_{J0} \ll 1$, the authors eliminate the coupling system to obtain an effective spin Hamiltonian in the charge basis $\{|0\rangle, |1\rangle\}^{\otimes 2}$, consisting only of terms of the form σ_i^z, σ_i^x, and $\sigma_1^x\sigma_2^x$, controlled by the external flux ϕ_{ex}. By tuning $\phi_{\text{ex}} = 0$, the two-qubit terms can be turned off to generate single-qubit operations, whereas for $\phi_{\text{ex}} = \pi$, we have only the coupling. The steps of the derivation have been put into a Mathematica notebook [Wol15] that can be found in appendix E. Since the transformation of variables contains some mathematical subtleties w.r.t. the domains of the operators (see also the discussion in appendix B), we have chosen not to make it. Instead we keep the Hamiltonian in the fundamental form that directly results from the circuit quantization rules in section 2.2.3. The same derivation applied to the original Hamiltonian then leads to the same single-qubit terms for $\phi_{\text{ex}} = 0$ and a two-qubit coupling of the same coupling strength for $\phi_{\text{ex}} = \pi$, but of the form $\sigma_1^y\sigma_2^y$ (see appendix E). Thus we consider the effective Hamiltonian

$$H^{\text{eff}} = \sum_{i=1}^{2} \left(E_{Ci} \left(n_{gi} - \frac{1}{2} \right) \sigma_i^z - E_{Ji} \cos \frac{\phi_{\text{ex}}}{2} \sigma_i^x \right) - \frac{E_{J1}E_{J2}}{4E_{J0}} \sin^2 \frac{\phi_{\text{ex}}}{2} \sigma_1^y \sigma_2^y \quad . \tag{5.8}$$

At the sweet spots, the terms along σ_i^z vanish such that H^{eff} generates only single-qubit rotations along the x-axis and two-qubit couplings of the type $\sigma_1^y\sigma_2^y$. The resultant leading-order terms can also be understood by an intuitive argument: First, the σ_i^z terms are the same as in Eq. (2.36a), so there is no surprise. Similarly, Eq. (2.36b) yields already half of the σ_i^x terms for $\phi_{\text{ex}} = 0$. The other half comes from the coupling term $\cos(\hat{\varphi}_0 - \hat{\varphi}_i) \approx \cos \hat{\varphi}_i$ since with the coupling system prepared in the transmon ground state, we have $\cos \hat{\varphi}_0 \approx 1$ (recall that $E_{J0} \gg E_{C0}$). This also explains why the σ_i^x terms cancel for $\phi_{\text{ex}} = \pi$, as $\cos(\hat{\varphi}_0 - \hat{\varphi}_i + \pi) = -\cos(\hat{\varphi}_0 - \hat{\varphi}_i)$. To understand the emergence of the exchange coupling $\sigma_1^y\sigma_2^y$ at next-to-leading order, it helps to recall the explicit form of the Josephson-coupling in the charge states (see Eq. (4.21) from the derivation of the product-formula algorithm). There we see that it generates single Cooper-pair transitions between the coupling junction and either qubit with phases determined by ϕ_{ex}. Eliminating these transitions then results in a virtual exchange coupling between both qubits.

Obviously, the next step is to see how well H^{eff} can describe the effective time evolution in the two-qubit subspace. For this purpose, we continuously evaluate the fidelity

$$F(t) = \frac{d \operatorname{Tr}(\rho(t)\rho^{\text{eff}}(t)) + 1}{d + 1} \quad , \tag{5.9}$$

where $d = 4$ as before, and

$$\rho^{\text{eff}}(t) = e^{-itH^{\text{eff}}} |\psi\rangle\langle\psi| e^{itH^{\text{eff}}} \tag{5.10}$$

represents the predicted effective time evolution, and $\rho(t)$ is the actual reduced density matrix obtained from the simulation. The results for various initial states $|\psi\rangle$ are shown in Fig. 5.4. We find that the ideal case for $\phi_{\text{ex}} = 0$ is accurately reproduced by H^{eff}. The case $\phi_{\text{ex}} = \pi$ can obviously only be well described at certain time intervals, suggesting that higher orders in η_1 and η_2 play a non-negligible role. For the real system, the additional

capacitive coupling terms seem to thwart the success of the effective Hamiltonian. This is reasonable since their energy scales are on the same order of magnitude as the Josephson energies of both qubits (see Tab. 5.1 and Eq. (2.48)). The reason that the singlet $|\Psi^-\rangle$ performs so well is that, as an eigenstate of $\sigma_1^x\sigma_2^x$, $\sigma_2^y\sigma_2^y$, and $\sigma_1^z\sigma_2^z$, its evolution is trivial in each case.

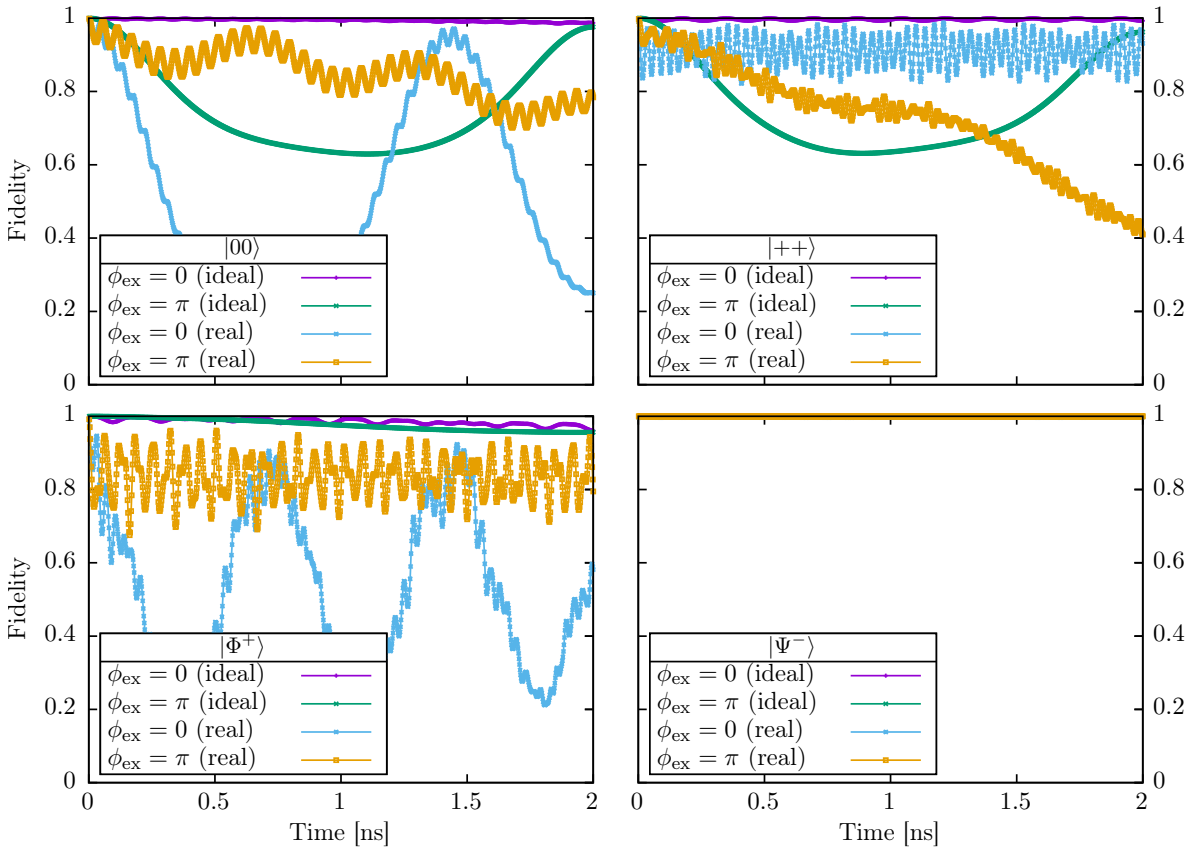

Figure 5.4.: Time evolution of the fidelity in Eq. (5.9) to compare the actual evolution given by H_{ideal} and H_{real} (see Eq. (2.48)) to the effective evolution generated by H^{eff} in Eq. (5.8). Both the ideal and the real case are shown for $\phi_{\text{ex}} \in \{0, \pi\}$. The four plots correspond to different initial states in the two-qubit subspace.

Since the success of the leading-order approximation H^{eff} in Eq. (5.8) especially for H_{real} seems to be rather limited, we use the procedure from section 4.4 to see which additional contributions need to be considered in an effective spin Hamiltonian. Furthermore, this also tells us whether there actually exists an effective unitary evolution in the two-qubit subspace such that eliminating the coupling system makes sense in the first place. For the optimization procedure given by Eq. (4.47), we set the parameters to $\tau = 0.001$, $m = 2000$, and $r = 12$. The results are shown in Tab. 5.2.

Table 5.2.: Effective Hamiltonians obtained from the generated data of the time evolution of 12 different initial states. The numbers in each 4×4 matrix are the expansion coefficients $h_{ij}/2\pi$ in GHz defined by Eq. (4.46). Beneath each matrix, the failure rate γ given by Eq. (4.48) is shown. The terms already contained in H^{eff} in Eq. (5.8) are shown in green if their magnitude is correct and in blue if not, while additional significant contributions are printed red. In all cases, the fits converged to the same Hamiltonians when no initial values were given, so the procedure is stable for this setup.

	$\phi_{\text{ex}} = 0$				$\phi_{\text{ex}} = \pi$				
		$\mathbb{1}_2$	σ_2^x	σ_2^y	σ_2^z		$\mathbb{1}_2$	σ_2^x	σ_2^y	σ_2^z
$H^{\text{eff}}_{\text{ideal}}$	$\mathbb{1}_1$	-0.000	-2.619	-0.000	0.000	$\mathbb{1}_1$	0.000	-0.010	0.000	-0.000
	σ_1^x	-2.619	-0.000	-0.000	-0.000	σ_1^x	-0.010	-0.001	-0.000	-0.000
	σ_1^y	-0.000	-0.000	0.001	0.000	σ_1^y	0.000	-0.000	-0.074	0.001
	σ_1^z	0.000	-0.000	0.000	-0.000	σ_1^z	-0.000	-0.000	0.001	0.007
	$\gamma = 0.000$					$\gamma = 0.823$				
		$\mathbb{1}_2$	σ_2^x	σ_2^y	σ_2^z		$\mathbb{1}_2$	σ_2^x	σ_2^y	σ_2^z
$H^{\text{eff}}_{\text{real}}$	$\mathbb{1}_1$	0.001	-5.113	0.014	0.000	$\mathbb{1}_1$	-0.000	-0.256	-0.011	-0.001
	σ_1^x	-5.114	-0.031	0.002	-0.001	σ_1^x	-0.256	-0.037	-0.002	-0.004
	σ_1^y	0.014	0.002	0.019	-0.031	σ_1^y	-0.012	-0.002	-0.351	0.005
	σ_1^z	0.000	-0.001	-0.030	0.001	σ_1^z	-0.001	-0.004	0.005	0.117
	$\gamma = 0.158$					$\gamma = 0.972$				

As expected from the plot in Fig. 5.4, the ideal case H_{ideal} for $\phi_{\text{ex}} = 0$ is well described by Eq. (5.8), and the corresponding failure rate $\gamma = 0.000$ shows that the effective evolution on the subspace is unitary. The dominating terms in $H^{\text{eff}}_{\text{ideal}}$ are single-qubit rotations about the x-axis, with the coefficients given by a value slightly smaller than the Josephson energy in Tab. 5.1. So in this case, the description in terms of H^{eff} is accurate. However, for $\phi_{\text{ex}} = \pi$ we find that the evolution of the system is too complex to be well described by an effective Hamiltonian in the two-qubit subspace. Even though the coefficient of $\sigma_1^y \sigma_2^y$ gives the largest contribution, it is smaller than the supposed coupling strength in Eq. (5.8) by a factor of 2, and the failure rate $\gamma = 0.823$ is close to one. Mathematically, this expresses the fact that the Kraus operators $M_{12}^{n_0}$ in Eq. (4.43) cannot be approximated by a unitary transformation.

In the real case H_{real} for $\phi_{\text{ex}} = 0$, the resulting coefficients of σ_1^x and σ_2^x of approx. $-5.1\,\text{GHz}$ are also slightly smaller than the Josephson energies given by Tab. 5.1. Interestingly, this explains the large sinusoidal oscillations of the blue curves in Fig. 5.4: Since the rotations about the x-axis are slightly slower than Eq. (5.8) predicts, the fidelity represented by the blue curve for $|\psi\rangle = |00\rangle$ returns to 1 only every 1.5 ns. A similar behavior is observed for $|\psi\rangle = |\Phi^+\rangle$, where the operation creates an entangled state. Apart from that, the red numbers in Tab. 5.2 for $H^{\text{eff}}_{\text{real}}$ indicate the effects of the additional capacitive coupling terms. Also in this case, higher failure rates reflect the fact that not all dynamics of the system can be sufficiently covered by an effective Hamiltonian.

5.2. Transmon quantum computer

In this section, we consider transmon qubits classified by a larger ratio of E_J/E_C (see section 2.3.1). Due to the decrease in charging energy, the bare charge states are not suitable for quantum computing anymore; instead, the new transmon eigenstates characterized by E_J and E_C constitute the computational basis.

The type of transmons we study are those with fixed energies coupled by fixed microwave resonators, where quantum gates are realized by capacitively coupled voltage sources using all-microwave controls. The design principle is sometimes called FLIC-FORQ and the idea is to take advantage of the natural spread in the parameters of the fabricated devices instead of suffering from it [RBD05]. The specific system we study is inspired by a recent setup from IBM that can be accessed on the Internet [IBM16]. A similar architecture was also recently employed to implement parity checks in a quantum error correction protocol [TCM+16].

The Hamiltonian of the system under consideration comprises two CPBs in the transmon regime coupled by a transmission line resonator (cf. Eq. (3.1)), i.e.

$$H = H_{\mathrm{CPB}} + H_{\mathrm{Res}} \quad , \tag{5.11}$$

where

$$H_{\mathrm{CPB}} = \sum_{i=1}^{2} \left(E_{Ci}(\hat{n}_i - n_{gi})^2 - E_{Ji}\cos\hat{\varphi}_i \right) \tag{5.12a}$$

$$H_{\mathrm{Res}} = \omega_r \hat{a}^\dagger \hat{a} + \sum_{i=1}^{2} g_i \hat{n}_i (\hat{a} + \hat{a}^\dagger) \quad . \tag{5.12b}$$

Since we consider microwave driving through the capacitively coupled voltage sources, and the external voltage is proportional to n_{gi}, we put an explicit time dependence on this control parameter from now on. Furthermore, it makes sense to separate H_{CPB} into the bare transmon systems H_{Tr1} and H_{Tr2}, and the external drivings H_{Dr1} and H_{Dr2}, such that (up to a constant) $H_{\mathrm{CPB}} = \sum_{i=1}^{2}(H_{\mathrm{Tr}i} + H_{\mathrm{Dr}i})$ where

$$H_{\mathrm{Tr}i} = E_{Ci}\hat{n}_i^2 - E_{Ji}\cos\hat{\varphi}_i \tag{5.13a}$$

$$H_{\mathrm{Dr}i} = -2E_{Ci}n_{gi}(t)\hat{n}_i \quad . \tag{5.13b}$$

It is common to write the microwave driving at frequency ω_{di} as

$$n_{gi}(t) = n_{gxi}(t)\cos(\omega_{di}t) + n_{gyi}(t)\sin(\omega_{di}t) \quad , \tag{5.14}$$

since in a rotating frame, the quadratures $n_{gxi}(t)$ and $n_{gyi}(t)$ induce single-qubit rotations about the x-axis and the y-axis, respectively [Gam13].

For the simulation, we define the Hilbert space given in Eq. (3.4) by $N_0 = 0$, $N_{\mathrm{ph}} = 3$, and $N_1 = N_2 = 8$ such that each qubit is described by 17 charge states. Since the transmon states $|m\rangle_i$ are superpositions of charge states distributed around $|n = 0\rangle_i$ [KYG+07], this number has proven sufficient to cover all dynamics without introducing boundary effects due to missing states in the representation of $|m\rangle_i$. In the simulation program, these states are actually obtained by diagonalizing the tridiagonal matrices

Table 5.3.: Device parameters defining the system Hamiltonian in Eq. (5.11). All energies are expressed in GHz with $\hbar = 1$. The CPBs are operated in the transmon regime with $E_{Ji}/E_{Ci} \approx 11$ (cf. Fig. 2.8) and their coupling to the detuned cavity is weak as $|\omega_i - \omega_r| \gg |g_i|$ for $i = 1, 2$.

	$E_{Ci}/2\pi$	$E_{Ji}/2\pi$	$\omega_i/2\pi$	$\delta_i/2\pi$	$\omega_r/2\pi$	$g_i/2\pi$
Transmon 1	1.204	13.349	5.350	-0.350	7	0.07
Transmon 2	1.204	12.292	5.120	-0.353	7	0.07

corresponding to $H_{\mathrm{Tr}i}$ given by Eq. (5.13a) in the charge basis. As the computational basis consists of the lowest transmon eigenstates $|m = 0\rangle_i$ and $|m = 1\rangle_i$, we prepare the qubits in various superpositions of these. The resonator is always initialized in its ground state of zero photons $|k = 0\rangle_{\mathrm{Res}}$. As before, the time step to solve the TDSE is set to 0.1 ps.

The device parameters for our two-qubit system are shown in Tab. 5.3. It contains the mandatory energies defining the Hamiltonian in Eq. (5.11). For reference, we also show the transition frequencies $\omega_i = \omega_i^{(0\to1)}$ between $|m = 0\rangle_i$ and $|m = 1\rangle_i$ and the anharmonicities $\delta_i = \omega_i^{(1\to2)} - \omega_i^{(0\to1)}$ obtained from diagonalizing $H_{\mathrm{Tr}i}$. These quantities are frequently used to characterize transmons in the literature (cf. [CGC+12; CGM+14; CMS+15]).

In the following sections, we first study the influence of different pulses for $n_{gi}(t)$ given by Eq. (5.14) on the accuracy of single-qubit gates, and then proceed to analyze the resonator-mediated two-qubit interaction between qubits of this type.

5.2.1. Single-qubit gates with various pulse shaping techniques

To realize single-qubit rotations, we need to specify a certain pulse shape for the external driving $n_{gi}(t)$ (see Eq. (5.14)). In particular, we need to choose the envelopes $n_{gxi}(t)$ and $n_{gyi}(t)$. As it turns out, the areas under these functions directly determine the angle of rotation [Gam13], and it is common to use Gaussian or tangential envelopes having simple pulse-shaping hardware requirements [MGR+09]. Unfortunately, due to the weak anharmonicity in the eigenspectrum of transmon systems, leakage into higher levels can be a limiting factor for the fidelity of single-qubit gates. Therefore, specific pulses have been devised to correct for this leakage. The essential idea is to keep the envelope on the first quadrature (say $n_{gxi}(t)$) and set the second quadrature proportional to its derivative (i.e., $n_{gyi}(t) \propto \dot{n}_{gxi}(t)$), going under the name *derivative removal by adiabatic gate* (DRAG) [MGR+09]. The technique has been tested in experiments [CDG+10; SBM+16; CKQ+16], and a comprehensive survey of the theory based on anharmonic oscillators is given in [GMM+11].

In the following, we first give a brief outline of the theory of optimized single-qubit rotations, and then present the results of our simulation based on the system defined by Eq. (5.11) and Tab. 5.3.

Theory of single-qubit pulses

The first step is to see how a transmon given by $H_{\mathrm{Tr}i}$ (see Eq. (5.13a)) can actually be approximated by an anharmonic oscillator. For that purpose, we introduce ladder operators $\hat{b}_i$ and $\hat{b}_i^\dagger$ such that

$$\hat{n}_i = -\sqrt[4]{\frac{E_{Ji}}{8E_{Ci}}}\left(\hat{b}_i + \hat{b}_i^\dagger\right) \tag{5.15a}$$

$$\hat{\varphi}_i = -i\sqrt[4]{\frac{E_{Ci}}{8E_{Ji}}}\left(\hat{b}_i - \hat{b}_i^\dagger\right) \quad . \tag{5.15b}$$

After substituting these expressions into $H_{\mathrm{Tr}i}$ given by Eq. (5.13a), expanding the cosine in $E_{Ci}/8E_{Ji}$, and making the RWA, one obtains [Gam13]

$$H_{\mathrm{Tr}i} \approx \tilde{\omega}_i \hat{b}_i^\dagger \hat{b}_i + \frac{\tilde{\delta}_i}{2}\hat{b}_i^\dagger \hat{b}_i(\hat{b}_i^\dagger \hat{b}_i - 1) \quad , \tag{5.16}$$

where $\tilde{\omega}_i = \sqrt{2E_{Ci}E_{Ji}} - E_{Ci}/4 \approx \omega_i$ and $\tilde{\delta}_i = -E_{Ci}/4 \approx \delta_i$ are good approximations to the qubit transition frequency and the anharmonicity, respectively. Since $|\tilde{\delta}_i| \ll |\tilde{\omega}_i|$, this Hamiltonian describes an oscillator of frequency $\tilde{\omega}_i$, where the transition frequency between successive levels m and $m+1$ is displaced by $m\tilde{\delta}_i$, and the corresponding eigenstates are generated by the ladder operator $\hat{b}_i^\dagger$. The driving Hamiltonian given by Eq. (5.13b) expressed in this basis reads

$$H_{\mathrm{Dr}i} = 2E_{Ci}\sqrt[4]{\frac{E_{Ji}}{8E_{Ci}}}n_{gi}(t)\left(\hat{b}_i + \hat{b}_i^\dagger\right) \quad . \tag{5.17}$$

In this frame, $H_{\mathrm{Dr}i}$ only generates single-qubit rotations about the x-axis since in the TLA, we have $\hat{b}_i + \hat{b}_i^\dagger \mapsto \sigma_i^x$. However, if the qubits are consistently defined in a frame rotating around the respective local z-axes at frequency $\tilde{\omega}_i$ (i.e. the change of basis is given by $R_i := \exp(-i\tilde{\omega}_i t\hat{b}_i^\dagger \hat{b}_i)$), we can generate a complete set of single-qubit rotations: Using the notation $H^R := R^\dagger H R - iR^\dagger \dot{R}$ and making the RWA, we obtain in the computational subspace [Gam13]

$$H_{\mathrm{Dr}i}^{R_i} = \frac{\beta_i n_{gxi}(t)}{2}\sigma_i^x + \frac{\beta_i n_{gyi}(t)}{2}\sigma_i^y \quad , \tag{5.18}$$

where $\beta_i = 2E_{Ci}\sqrt[4]{E_{Ji}/8E_{Ci}}$. Note that we have set the detuning between the microwave field and the qubit frequency to zero, i.e., $\omega_{di} = \tilde{\omega}_i$. So we can generate rotations on two independent quadratures and thus cover the entire Bloch sphere. From the expression of the unitary time evolution operator $\exp(-i\int_0^t H_{\mathrm{Dr}i}^{R_i}\,\mathrm{d}\tau)$ in conjunction with appendix D, we find that the total angle of rotation is given by the area under the envelopes $n_{gxi}(t)$ and $n_{gyi}(t)$. For instance, rotations of angle α_x about the x-axis must satisfy

$$\alpha_x \stackrel{!}{=} \int_0^t \beta_i n_{gxi}(\tau)\,\mathrm{d}\tau \quad . \tag{5.19}$$

We use this normalization condition on the pulses to engineer single-qubit rotations of various angles. For the particular shape of the pulse, we consider a set of four different

functions for $\beta_i n_{gxi}(t)$ or $\beta_i n_{gyi}(t)$, respectively:

$$\Omega^C(t) = A_C \qquad \text{(Constant)} \tag{5.20a}$$

$$\Omega^L(t) = A_L \left(\frac{t_g}{2} - \left| t - \frac{t_g}{2} \right| \right) \qquad \text{(Linear)} \tag{5.20b}$$

$$\Omega^G(t) = A_G \left(\exp\left(-\frac{(t-t_g)^2}{2\sigma_G^2} \right) - \exp\left(-\frac{t_g^2}{8\sigma_G^2} \right) \right) \qquad \text{(Gaussian)} \tag{5.20c}$$

$$\Omega^T(t) = A_T \left(\tanh \frac{t}{\sigma_T} + \tanh \frac{t_g - t}{\sigma_T} - \tanh \frac{t_g}{\sigma_T} \right) \qquad \text{(Tangential)} \tag{5.20d}$$

In these expressions, all functions are defined for $0 \leq t \leq t_g$, where t_g is the gate time. The normalization factors $A_{C/L/G/T}$ are determined by Eq. (5.19), and the standard deviation σ_G for the Gaussian pulse and the rise-time parameter σ_T for the tangential pulse are both set to $t_g/4$.

As mentioned above, the pulses given by Eqs. (5.20a)–(5.20d) can result in unwanted leakage into the third level $|m = 2\rangle_i$ [MGR+09]. Based on an anharmonic oscillator defined by Eq. (5.16), the theory of DRAG proposes a driving of the other quadrature proportional to the derivative of the pulse. As the pulses are all symmetric w.r.t. $t_g/2$, their derivatives are antisymmetric such that their integral over the gate duration vanishes. Thus the net angle of rotation on this quadrature is not changed (see Eq. (5.19)). However, the leakage into the third level is expected to reduce such that the gate's accuracy can improve [GMM+11].

In particular, we consider three kinds of DRAG corrections for a given shape $\Omega(t)$ chosen from Eqs. (5.20a)–(5.20d). They are called the Y-only first-order correction, the optimal first-order correction, and the Y-only second-order correction, respectively [GMM+11]. All of them are characterized by a pulse $\Omega_1(t)$ on one quadrature, a derivative pulse $\Omega_2(t)$ on the other quadrature, and a phase $\delta(t)$:

$$\textbf{(DRAG1Y)} \quad \Omega_1(t) = \Omega(t), \qquad \Omega_2(t) = -\frac{\dot{\Omega}(t)}{2\delta_i}, \quad \delta(t) = 0, \tag{5.21a}$$

$$\textbf{(DRAG1O)} \quad \Omega_1(t) = \Omega(t), \qquad \Omega_2(t) = -\frac{\dot{\Omega}(t)}{\sqrt{2}\delta_i}, \quad \delta(t) = \frac{\Omega(t)^2}{2\delta_i}(1 - \sqrt{2}), \tag{5.21b}$$

$$\textbf{(DRAG2Y)} \quad \Omega_1(t) = \Omega(t) + \frac{\Omega(t)^3}{8\delta_i^2}, \quad \Omega_2(t) = -\frac{\dot{\Omega}(t)}{2\delta_i}, \quad \delta(t) = 0. \tag{5.21c}$$

The phase $\delta(t)$ originally represents the detuning between the driving and the qubit frequency. However, since we have fixed-frequency qubits with $\omega_{di} = \tilde{\omega}_i$, we need to apply phase ramping to achieve the same effect [GMM+11]. Thus the mapping between these pulses and the envelopes $n_{gxi}(t)$ and $n_{gyi}(t)$ for rotations about the x-axis is

$$n_{gxi}(t) = \frac{1}{\beta_i} \left(\Omega_1(t) \cos\left(\int_0^t \delta(s)\,\mathrm{d}s \right) + \Omega_2(t) \sin\left(\int_0^t \delta(s)\,\mathrm{d}s \right) \right) \tag{5.22a}$$

$$n_{gyi}(t) = \frac{1}{\beta_i} \left(\Omega_2(t) \cos\left(\int_0^t \delta(s)\,\mathrm{d}s \right) - \Omega_1(t) \sin\left(\int_0^t \delta(s)\,\mathrm{d}s \right) \right) \quad . \tag{5.22b}$$

If $\delta(t) = 0$, phase ramping simply falls back to identifying $n_{gxi}(t) = \Omega_1(t)/\beta_i$ and $n_{gyi}(t) =$

$\Omega_2(t)/\beta_i$. To realize rotations about the y-axis, we just need to replace $(n_{gxi}, n_{gyi}) \mapsto (n_{gyi}, -n_{gxi})$; otherwise, the relations stay the same.

Simulation

We study the universal set of single-qubit rotations $\bigcup_{i=1}^{2}\{X_\pi^i, X_{\pi/2}^i, X_{\pi/4}^i, X_{\pi/8}^i, Y_\pi^i, Y_{\pi/2}^i\}$ [CGC+12] using the notation from appendix D. The various pulse shapes are defined in Eqs. (5.20a)–(5.20d) and the DRAG corrections are given by Eqs. (5.21a)–(5.21c). We consider three different gate times $t_g \in \{4\,\text{ns}, 8\,\text{ns}, 40\,\text{ns}\}$ representing short, intermediate, and long single-qubit gates [SBM+16]. For each gate, we compute the gate fidelity given by Eq. (5.6) with $d = 2^2 = 4$ and monitor the leakage. This leakage is defined as the probability to find the qubit in the primary non-computational state $|m = 2\rangle$ since the corresponding transition is expected to be suppressed by the design of the DRAG pulses [GMM+11]. To study the influence of the experimentally always-on coupling between both qubits, we first run every setup with the resonator Hamiltonian (see Eq. (3.1)) switched off, and then repeat the experiment with the coupling switched on. The results are presented in Figs. 5.5–5.5. We only show the results of the various single-qubit gates on the first qubit, since the difference to applying the same gates to the second qubit is insignificant.

We find that for short pulses of $t_g = 4\,\text{ns}$ (see Figs. 5.5 and 5.6), simple Gaussian pulses produce the worst results. Correcting them with DRAG substantially improves the fidelities and reduces the leakage, suggesting that leakage to higher levels is indeed an essential source of errors. The second-order Y-only correction produces the best results in terms of fidelity (recall, though, that a fidelity of almost 95% can still mean that the spin does not point in the right direction as shown in Fig. F.2). The best result in terms of leakage, however, is achieved by the optimal first-order correction. This agrees with the recent experimental finding that these DRAG pulses always have a trade-off between total fidelity and leakage errors [CKQ+16]. In general, tangential pulse shapes tend to perform slightly better than Gaussians. Interestingly, reducing the angle of rotation always increases the gate fidelity and reduces leakage. Since smaller angles directly correspond to smaller amplitudes of the voltages (see Eq. (5.19)), this indicates that a Bloch-Siegert shift [BS40] resulting from the counter-rotating terms of the RWA may play a role. We also observe a related behavior in the spins' motion on the Bloch sphere (see section 4.3). The presence of the always-on coupling through the resonator is not evident for short gates.

The results for intermediate gate durations of $t_g = 8\,\text{ns}$ are shown in Fig. 5.7. The leakage into the third level has been reduced by a factor of 10 w.r.t. Fig. 5.5, which is in agreement with the populations predicted by the theory [GMM+11]. Consequently, the single-qubit fidelities have improved significantly. Furthermore, as a consequence of the reduced amplitudes of the control pulses, we find that the spin's path on the Bloch sphere has become smoother. The second-order DRAG correction still produces the best fidelities above 99% in all cases, with the winner again being the tangential pulse shape.

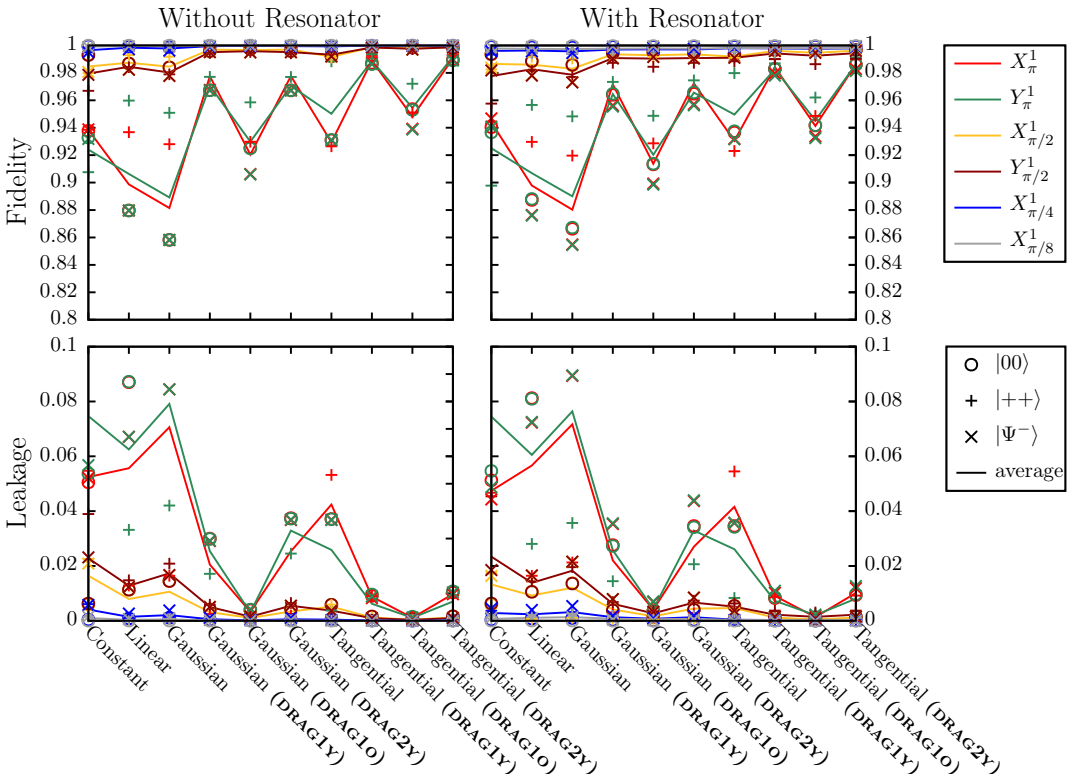

Figure 5.5.: Gate fidelity and leakage for short gates ($t_g = 4\,\mathrm{ns}$) dependent pulse shape and the presence of the resonator. Different colors correspond to different gates. For each gate and pulse shape, the markers "o", "+", and "x" correspond to the initial states $|00\rangle$, $|{+}{+}\rangle$, and $|\Psi^-\rangle$, respectively. The averages are represented by solid lines.

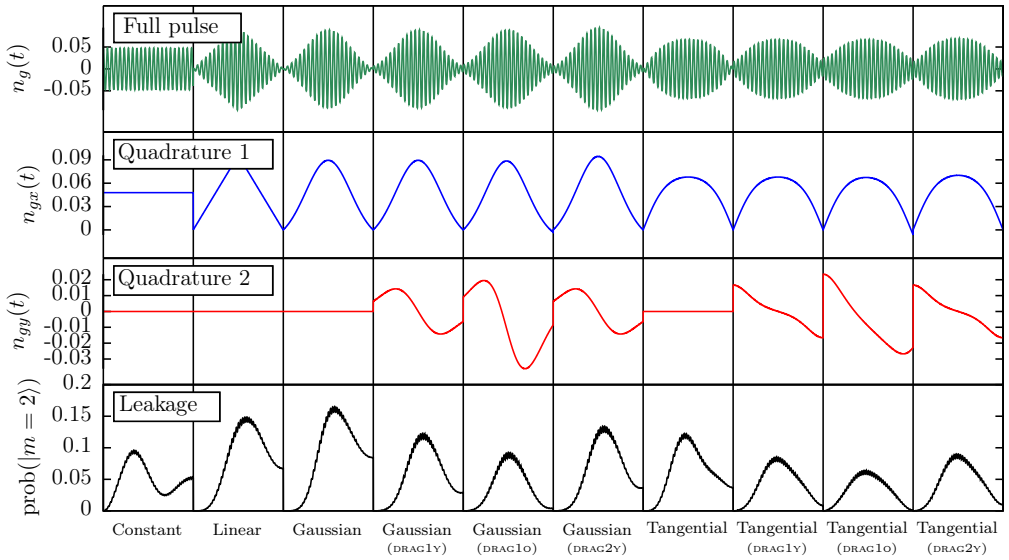

Figure 5.6.: Pulse shapes and time evolution of the leakage for the operation $X^1_\pi\,|\Psi^-\rangle$ and a gate duration of $t_g = 4\,\mathrm{ns}$. The first control (blue) resembles the pulse shape chosen from Eqs. (5.20a)–(5.20d), and for the DRAG corrections, the second control (red) resembles its derivative. The intermediate population of the level $|m = 2\rangle_1$ is shown in black. For each pulse, it is on the order of 10%. The corresponding results for the other gates (not shown) are the same with and without resonator; however, the scale of the leakage for smaller angles goes down to 0.1% for $X^1_{\pi/8}$.

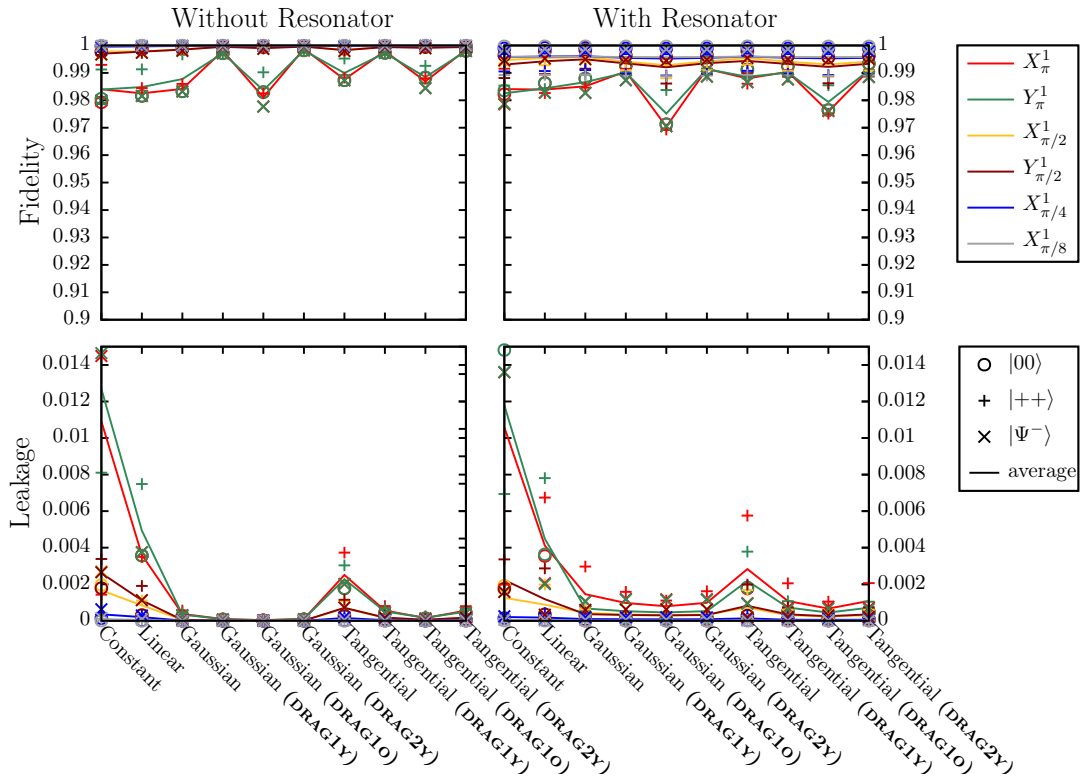

Figure 5.7.: The same as Fig. 5.5 for intermediate gate times $t_g = 8\,\text{ns}$. For all pulses, the gate fidelities and the leakage have improved substantially. The effect of the resonator on the single-qubit gates is still not directly visible.

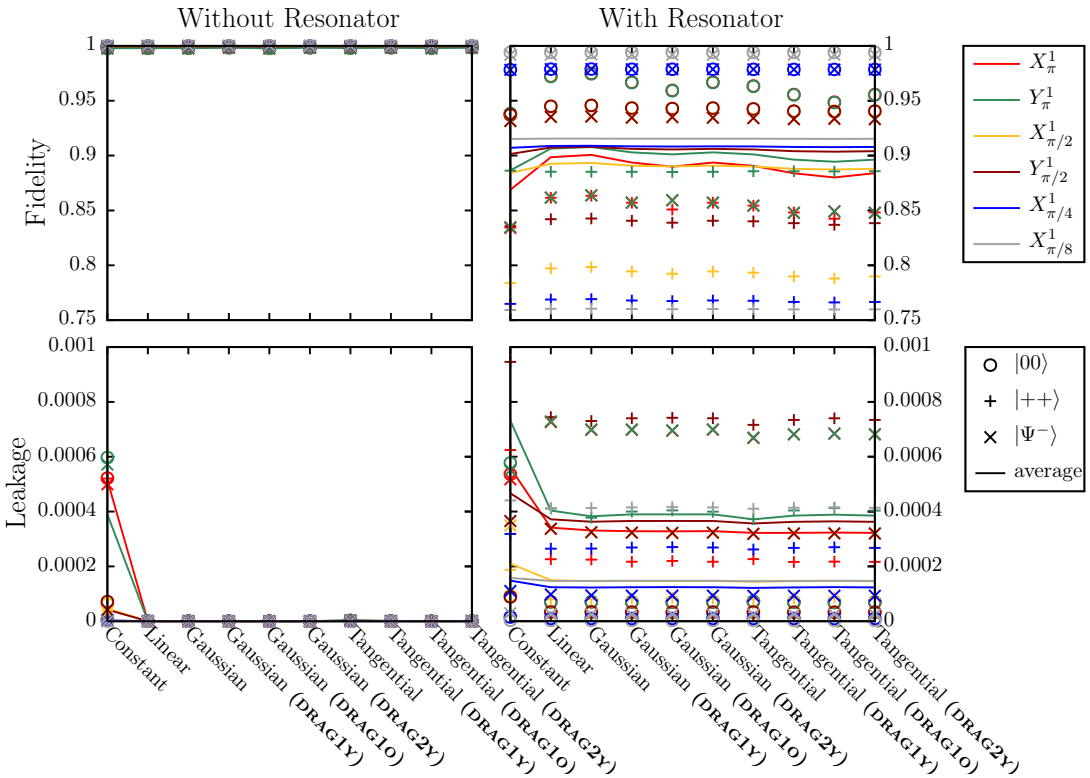

Figure 5.8.: The same as Fig. 5.5 for long gate times $t_g = 40\,\text{ns}$. Without the resonator, all single-qubit gates are nearly perfect. With the coupling between both qubits switched on, a strong dependence of the fidelity on the prepared initial state can be observed.

For long gate times with the resonator switched off, the single-qubit gates are nearly perfect (see Fig. 5.8), all reaching fidelities above 99.7%. The specific shapes of the pulses and the usage of DRAG make no difference since the spectral weight of the pulses at the transmon anharmonicity is negligible [Gam13]. This has also been experimentally confirmed [CDG+10]. Interestingly, with the resonator switched on, simple Gaussian pulses perform best on average. However, this slightly better performance is not very significant due to the large spread in the fidelity for different initial states (for $X^1_{\pi/8}$ we have $F_g \approx 75\%$ for $|{+}{+}\rangle$, while $F_g \approx 100\%$ for $|00\rangle$). The reason for the almost constant displacement in fidelity lies in the cavity-induced Lamb shift of the qubit's frequency: On the Bloch sphere, we observe an additional rotation of the spins about the z-axis of approx. $g_i^2/(\omega_i - \omega_r) \times t_g \approx -\pi/4$. A solution would be to adjust the pulses to the Lamb-shifted energy levels or to use control calibration techniques to optimize for the systematic over- and underrotations [SBM+16]. Errors due to the always-on interaction can also be tackled using dynamical decoupling with refocusing pulses known from NMR [DP14].

The long gate durations have also been used in current experiments on quantum error correction [CGM+14; CMS+15; TCM+16] due to the long coherence times of transmons and the high fidelity of the operations. However, eventually the speed of single-qubit gates should not be restricted to these time scales. To make the single-qubit gates faster, additional techniques refining the simple DRAG pulses should be taken into account [SDE+13; CKQ+16]. It would be an interesting project to further analyze these ideas.

5.2.2. Two-qubit interaction and the cross-resonance gate

For a high-fidelity two-qubit gate, one needs to have a good understanding of the effective interaction between the single transmon qubits. In the circuit QED architecture that we consider (see section 2.3 and Eq. (5.11)), this interaction is mediated by the resonator that both transmons are weakly coupled to. Since the resonator is described by a separate subspace of the Hilbert space, this setup represents an ideal candidate to apply the effective Hamiltonian procedure outlined in section 4.4. From the theory that we briefly summarize first, we expect a two-qubit exchange interaction in terms of a spin Hamiltonian. Since the theory involves quite a few approximations, we will need to deepen our understanding of the reliability of such effective Hamiltonians in general. Finally, we consider a popular scheme for a two-qubit gate by studying the cross-resonance effect [CCG+11; SMC+16].

Since the coupling of both qubits to the resonator is weak (see Tab. 5.3), common two-qubit gates in this setup usually take about ten times as long as the single-qubit gates [CGM+14; CMS+15; TCM+16]. Consequently, to make the global error of the product-formula algorithm negligible (cf. section 4.2), we reduce the time step to solve the TDSE again by a factor of 10, corresponding to 0.01 ps. We have verified that all experiments we run are independent of this time step and the dimensions of the Hilbert space, implying that numerical errors do not play a role in the results.

Theory of two-qubit exchange interaction

In the last section, we introduced the raising and lowering operators $\hat{b}_i^\dagger$ and $\hat{b}_i$ to describe the eigenstates of the transmons and to expose their anharmonic oscillator character. Now we extend this view to the resonator Hamiltonian given by Eq. (5.12b): By substituting

Eq. (5.15a), we obtain

$$H_{\mathrm{Res}} = \omega_r \hat{a}^\dagger \hat{a} - \sum_{i=1}^{2} \sqrt[4]{\frac{E_{Ji}}{8E_{Ci}}} g_i (\hat{a} + \hat{a}^\dagger)(\hat{b}_i + \hat{b}_i^\dagger)$$
$$\approx \omega_r \hat{a}^\dagger \hat{a} + \sum_{i=1}^{2} G_i (\hat{a}\hat{b}_i^\dagger + \hat{a}^\dagger \hat{b}_i) \quad . \tag{5.23}$$

where in the last line, the RWA has been made [Gam13], and $G_i = -\sqrt[4]{E_{Ji}/8E_{Ci}}\, g_i$ is the resulting coupling constant between the transmon states and the resonator photons. H_{Res} resembles a multi-level version of the well-known Jaynes-Cummings model [JC63] of atoms interacting with an optical cavity. The next step is to eliminate the resonator to see which form of effective two-qubit interaction emerges. This step has been done in NMR setups and cavity QED architectures [SM99; ZG00; RBH01] and in circuit QED architectures [BHW+04; MCG+07; LCP08; Cho10; Gam13; SMO+15] using various techniques such as the Schrieffer-Wolff transformation to go to the dressed frame. The resulting two-qubit exchange interaction is of the form $J(\hat{b}_1\hat{b}_2^\dagger + \hat{b}_1^\dagger\hat{b}_2)$. In the TLA, this results in $J(\sigma_1^-\sigma_2^+ + \sigma_1^+\sigma_2^-) = J(\sigma_1^x\sigma_2^x + \sigma_1^y\sigma_2^y)/2$. With the number of photons in the resonator set to zero, the effective Hamiltonian of the total undriven system $H_{\mathrm{Tr1}} + H_{\mathrm{Tr2}} + H_{\mathrm{Res}}$ then reads

$$H_{\mathrm{Theory}}^{\mathrm{eff}} = -\frac{\omega_{L1}}{2}\sigma_1^z - \frac{\omega_{L2}}{2}\sigma_2^z + \frac{J}{2}(\sigma_1^x\sigma_2^x + \sigma_1^y\sigma_2^y) \quad , \tag{5.24}$$

where $J = G_1G_2(\omega_1 + \omega_2 - 2\omega_r)/2(\omega_1 - \omega_r)(\omega_2 - \omega_r)$ is the effective two-qubit coupling strength, and $\omega_{Li} = \omega_i + G_i^2/(\omega_i - \omega_r)$ is the qubit transition frequency shifted by its interaction with the resonator (usually called *Lamb shift*). It is worth mentioning that sometimes also other types of transverse coupling are assumed such as only $J\sigma_1^x\sigma_2^x$ [War15].

Finally, it is helpful to keep an overview of the required approximations to obtain the simple spin Hamiltonian in Eq. (5.24) [Gam13]:

(a) Approximating the transmon as an anharmonic oscillator for $E_{Ji} \gg E_{Ci}$

(b) Expansion to second order in the couplings $G_i/(\omega_i - \omega_r)$

(c) RWA: $(\hat{a} + \hat{a}^\dagger)(\hat{b}_i + \hat{b}_i^\dagger) \approx \hat{a}\hat{b}_i^\dagger + \hat{a}^\dagger\hat{b}_i$

(d) TLA: $\hat{b}_i \approx \sigma_i^-$ and $\hat{b}_i^\dagger \approx \sigma_i^+$

(e) Assuming the dynamics in the total Hilbert space can be covered by a 4×4 matrix

Especially the last assumption corresponding to Eq. (4.45) is usually made without further consideration; but as is known from the Kraus representation (see also the discussion below Eq. (4.43)) and as we have seen in the example in section 5.1.2, this is not necessarily to be taken for granted.

Measuring the effective Hamiltonian

As the effective Hamiltonian given in Eq. (5.24) is the foundation for many gate proposals [Gam13], it is worth analyzing to which degree it can reproduce the free evolution of the

system. We do this by applying the procedure described in section 4.4. It will not only allow us to compute the Lamb shift and the effective qubit coupling, but also to test whether the optimal effective coupling is actually of the form $\sigma_1^x\sigma_2^x + \sigma_1^y\sigma_2^y$. After that, we further analyze on which time scale such effective Hamiltonians can describe the time evolution accurately.

The parameters for the procedure in Eq. (4.47) are set to $\tau = 0.1$, $m = 4000$, and $r = 12$ such that a free evolution over 400 ns is used to infer the optimal effective Hamiltonian. Note that τ corresponds to 0.1 ns and is thus much larger than the time step used to solve the TDSE. This is done to ensure that intermediate entanglement between the systems on short time scales is not given too much weight. Under this condition, the purity of the reduced density matrices is always very close to 1, and the procedure's results are robust against variations in the parameters. The resulting coefficients of the effective Hamiltonian in comparison with those of the Hamiltonian given in Eq. (5.24) are shown in Tab. 5.4.

The first thing to note is that the failure rate $\gamma = 2.625 \times 10^{-5}$ defined by Eq. (4.48) is very low, indicating that the dynamics can indeed be described by an effective Hamiltonian. Next, the coefficients of σ_i^z almost exactly match those predicted by the theory, meaning that the Lamb shifts $G_i^2/(\omega_i - \omega_r) \in \{2\pi \times -0.0035\,\mathrm{GHz}, 2\pi \times -0.0029\,\mathrm{GHz}\}$ have also been found by the procedure. However in the last digits, there is still a difference of the same order of magnitude as the Bloch-Siegert shift $-G_i^2/(\omega_i + \omega_r)$ which is a consequence of the counter-rotating terms dropped in the RWA (see also [BS40], [Rig09], and [RGP+12]). In addition to this, we observe a dominance of $\sigma_1^x\sigma_2^x$ as opposed to $\sigma_1^x\sigma_2^x + \sigma_1^y\sigma_2^y$ with a coupling strength about twice as high. Note that these types of transverse couplings are usually considered equal under the RWA. Apart from the dominant transverse couplings, there is also a longitudinal contribution of the type $\sigma_1^z\sigma_2^z$.

To measure the time scale on which these seemingly negligible differences become important, we evaluate the time-dependent fidelity given by Eq. (5.9) for four different effective Hamiltonians: The first case is $H^{\mathrm{eff}}_{\mathrm{Theory}}$ given by Eq. (5.24), and the second case corresponds to the optimal Hamiltonian $H^{\mathrm{eff}}_{\mathrm{Fit}}$ shown on the left-hand side in Tab. 5.4. In addition to this, we define $H^{\mathrm{eff}}_{\mathrm{SQ}}$ as $H^{\mathrm{eff}}_{\mathrm{Theory}}$ with only the single-qubit coefficients of σ_i^z taken from the fit (thus measuring effects beyond the Lamb shift). Finally, we measure the effect of also including the longitudinal coupling, i.e., $H^{\mathrm{eff}}_{\mathrm{Long}} = H^{\mathrm{eff}}_{\mathrm{SQ}} + h_{33}\sigma_1^z\sigma_2^z$. The fidelities for four different initial states over a total time evolution of 400 ns (corresponding to common two-qubit gate lengths) are shown in Fig. 5.9.

We find that for the computational basis states, there is no observable difference among the effective Hamiltonians in the description of the time evolution. However, this does not necessarily mean that this also holds for superpositions of the basis states. For the states $|{\pm}{\pm}\rangle$ of the Hadamard basis, for instance, $H^{\mathrm{eff}}_{\mathrm{Theory}}$ loses almost 5% in fidelity after 400 ns, which results in the spins pointing up to 30° away from where they are supposed to be (cf. Fig. F.2). By replacing the single-qubit contributions in $H^{\mathrm{eff}}_{\mathrm{Theory}}$ with those from the fit (i.e., going from the red to the navy blue curve in Fig. 5.9), we can remove most of this error. Hence, even the minuscule difference beyond the Lamb shift in the last two digits of the coefficients of σ_i^z (see Tab. 5.4) becomes significant. By further including the longitudinal coupling strength $h_{33}/2\pi = 0.044\,\mathrm{MHz}$ (from the navy blue to the turquoise curve in Fig. 5.9), also the remaining difference in the fidelity can be explained. However, a difference between the transverse couplings is not observable within the first 400 ns.

Table 5.4.: Effective Hamiltonian obtained from the free evolution (left) in comparison with the theoretical result given in Eq. (5.24) (right). The numbers are the expansion coefficients $h_{ij}/2\pi$ in GHz defined by Eq. (4.46). Only the nonzero coefficients are shown. The single-qubit coefficients are almost equal to those predicted by the theory, but as we see below, the differences in the last digits becomes important for long evolutions. Furthermore, the dominant coupling is of the type $\sigma_1^x\sigma_2^x$ and not $\sigma_1^x\sigma_2^x + \sigma_1^y\sigma_2^y$.

$H_{\text{Fit}}^{\text{eff}}$					$H_{\text{Theory}}^{\text{eff}}$				
	$\mathbb{1}_2$	σ_2^x	σ_2^y	σ_2^z		$\mathbb{1}_2$	σ_2^x	σ_2^y	σ_2^z
$\mathbb{1}_1$				-2.558469	$\mathbb{1}_1$				-2.558525
σ_1^x		-0.003395	-0.000077		σ_1^x		-0.001608		
σ_1^y		-0.000066	-0.000051		σ_1^y			-0.001608	
σ_1^z	-2.673194			0.000044	σ_1^z	-2.673244			
		$\gamma = 2.625 \times 10^{-5}$							

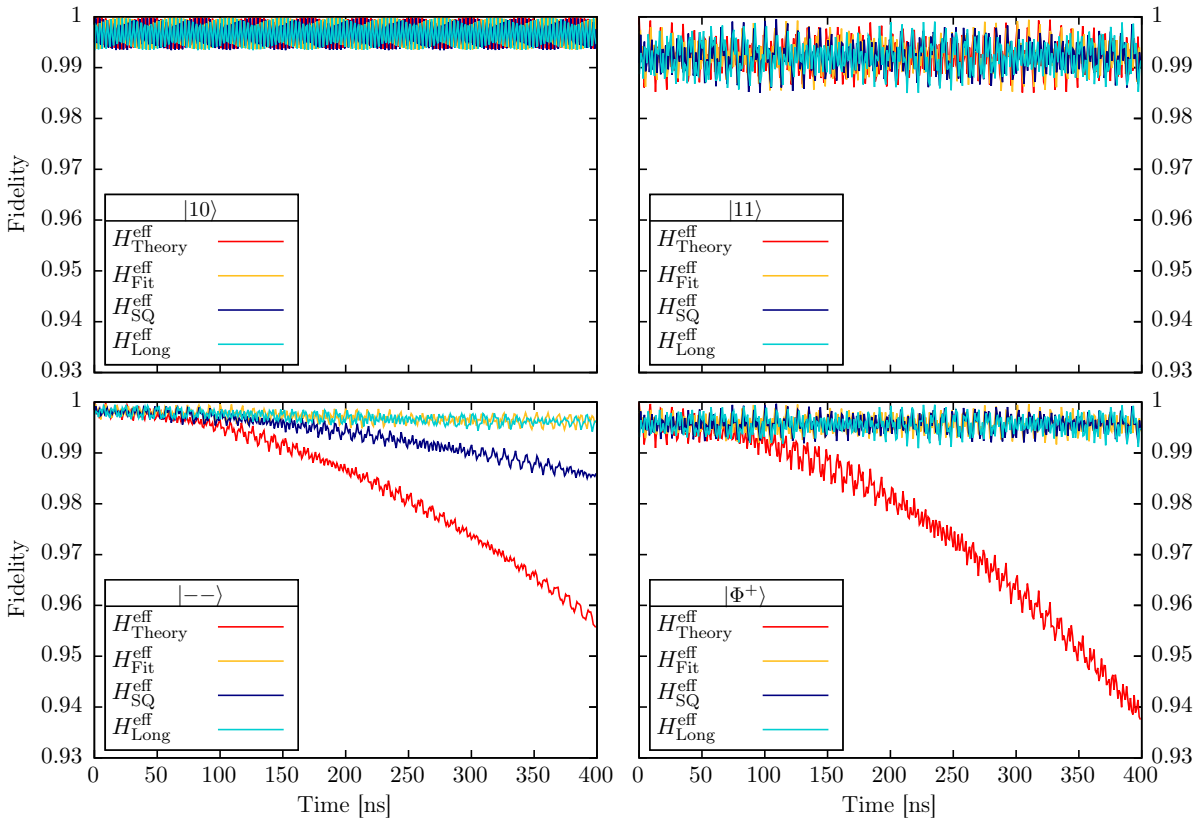

Figure 5.9.: Time evolution of the fidelity given in Eq. (5.9) for four different effective Hamiltonians, namely the theoretical result given by Eq. (5.24) (red), the fit (yellow), the theory with σ_i^z taken from the fit (navy blue), and the theory with σ_i^z and $\sigma_1^z\sigma_2^z$ taken from the fit (turquoise). The four plots correspond to different initial states in the two-qubit subspace. For the computational basis states, the effective evolutions are all equal, but for the superposition states $|{-}{-}\rangle$ and $|\Phi^+\rangle$ (bottom), we observe differences.

Motivated by the slow linear growth of the difference in both time evolution operators $\|\exp(-itH^{\text{eff}}_{\text{Fit}}) - \exp(-itH^{\text{eff}}_{\text{Long}})\|_2 \approx 0.04\,\text{MHz} \cdot t$, we have extended the time evolution to 4000 ns (data not shown). The resulting fidelity of $\sigma_1^x\sigma_2^x$ is about 1% better on average, yet there is still no significant difference. The reason for this lies in the rapid oscillations in the fidelities, which stem from intermediate entanglement between the resonator and the transmons, where the time evolution in the two-qubit subspace cannot be exactly reproduced by a unitary evolution (see Eq. (4.43)).

So although the evolution in the reduced two-qubit space can be very well approximated by a unitary evolution, the complete two-transmon evolution is too complicated to discriminate between the different types of transverse couplings $\sigma_1^{x/y}\sigma_2^{x/y}$ in the reduced two-qubit space. Therefore, for the relevant two-qubit gate types, it can only be said that there is a dominant transverse two-qubit coupling. And indeed, it may be this fact that makes the cross-resonance gate the preferred two-qubit gate for these systems [SMC+16], namely that the principle of the method works for all effective Hamiltonians with any combinations of $\sigma_1^{x/y}\sigma_2^{x/y}$ coupling terms [GAL+12]. Therefore, we now proceed to investigate the underlying effects of this gate.

The cross-resonance effect

The idea of the cross-resonance (CR) effect is quite simple: By irradiating the first qubit (control qubit) at the frequency of the second qubit (target qubit), we can generate an interaction that grows linearly in the irradiation's amplitude. A weak transverse coupling between the qubits can thus be enhanced to generate an entangling gate. The principle can already be demonstrated for a simple two-qubit setting: Assume the system is described in the lab frame by

$$H_{\text{TQS}} = -\frac{\omega_{L1}}{2}\sigma_1^z - \frac{\omega_{L2}}{2}\sigma_2^z + J\sigma_1^x\sigma_2^x + \Omega\cos\omega_{L2}t\,\sigma_1^x \quad . \tag{5.25}$$

This Hamiltonian resembles the effective Hamiltonian for our transmon system (see Eq. (5.24)) with an additional driving of the first qubit at frequency ω_{L2} and amplitude Ω. Since we are in the lab frame, such a driving can immediately be realized by choosing the voltage $n_{g1}(t)$ in Eq. (5.17). We have adjusted the resonator-mediated coupling as a consequence of the results obtained in the last section; note, however, that the principle works for any transverse coupling [GAL+12]. Since the qubits are usually defined in a reference frame following the drive frequency (cf. section 5.2.1), we move to a rotating frame defined by $R = \exp(-i\omega_{L2}t(\sigma_1^z + \sigma_2^z)/2)$. In this frame, one can show [RD10] that for $|\Omega|, |J| \ll |\omega_{L1} - \omega_{L2}|$, the dominant coupling is $\sigma_1^z\sigma_2^x$ with a coupling strength proportional to Ω. As this coupling becomes $+\sigma_2^x$ if the control qubit is $|0\rangle$ and $-\sigma_2^x$ if the control qubit is $|1\rangle$, this term generates a conditional rotation of the target qubit about the x-axis, thereby having the potential to entangle both qubits. Together with the other dominant terms, the system is thus approximately described by [Ric13]

$$H^R_{\text{TQS}} \approx -\frac{\Delta_{12}}{2}\sigma_1^z + \frac{\Omega}{2}\sigma_1^x - \frac{\Omega J}{2\Delta_{12}}\sigma_1^z\sigma_2^x \quad , \tag{5.26}$$

where $\Delta_{12} = \omega_{L1} - \omega_{L2}$ is the detuning between both qubits. Note that we have again made use of the notation $H^R = R^\dagger H R - iR^\dagger\dot{R}$ representing the Hamiltonian if the computational basis is defined in the rotating frame.

In experiments on transmon systems, however, an additional unconditional rotation

of the second qubit about the x-axis needs to be taken into account [CGC+13]. This term is of the form σ_2^x and is sometimes considered a consequence of spurious electromagnetic crosstalk [War15]. Furthermore, it is reasonable to assume that the presence of higher energy levels influences the coupling strengths if certain resonance conditions are met. Indeed, a deeper theoretical analysis starting from Eq. (5.17) and Eq. (5.23) yields [Gam13]

$$H_{\text{Sys}}^R = -\frac{\Delta_{12}}{2}\sigma_1^z + \frac{\Omega}{2}\sigma_1^x + J_{ZX}^{\text{eff}}\,\sigma_1^z\sigma_2^x + J_{IX}^{\text{eff}}\,\sigma_2^x \quad , \tag{5.27}$$

where

$$J_{IX}^{\text{eff}} = -\frac{\Omega}{2}\frac{J}{\Delta_{12}}\frac{\Delta_{12}}{(\Delta_{12}+\delta_1)} \tag{5.28a}$$

$$J_{ZX}^{\text{eff}} = -\frac{\Omega}{2}\frac{J}{\Delta_{12}}\frac{\delta_1}{(\Delta_{12}+\delta_1)} \quad . \tag{5.28b}$$

Thus the higher energy levels of the transmon enter through the anharmonicity δ_1, which can be physically interpreted in two instructive limits: For $\delta_1 = 0$, the transmon becomes a harmonic oscillator and the entangling properties of the system vanish. For $|\delta_1| \to \infty$, however, the transmon simplifies to a two-level system and we recover Eq. (5.26). Observe also that the coupling strengths exhibit divergences at $\Delta_{12} = -\delta_1$ (and J_{ZX}^{eff} additionally at $\Delta_{12} = 0$). This means that the higher level transitions of the first transmon become aligned with the transitions of the second, thus boosting the microwave-induced interaction. This is favorable since in theory, a higher interaction strength allows shorter gate durations. The effect has been measured in experiments [War15], and it is one of our motivations to study to which degree the interaction can be enhanced by matching these resonance conditions. Of course, since the transmon is not a perfect anharmonic oscillator, these divergences are cut off in the general case.

Despite the theoretical understanding of the CR effect, experiments suffer from difficulties in pushing the speed and the fidelity of the gate to the coherence limit. In [SMC+16], the authors have therefore developed a procedure to measure additional contributions to the system Hamiltonian that have not been found using the perturbative treatment leading to Eq. (5.27). In the following, we apply the same method of Hamiltonian tomography to our system to assess which of the additional terms emerge from the pure Hamiltonian evolution of the system, and which can be attributed to additional environmental influences.

The procedure in [SMC+16] is based on a CR Hamiltonian of the form

$$H_{CR}^R = J_{IX}^{\text{eff}}\,\sigma_2^x + J_{IY}^{\text{eff}}\,\sigma_2^y + J_{IZ}^{\text{eff}}\,\sigma_2^z + J_{ZX}^{\text{eff}}\,\sigma_1^z\sigma_2^x + J_{ZY}^{\text{eff}}\,\sigma_1^z\sigma_2^y + J_{ZZ}^{\text{eff}}\,\sigma_1^z\sigma_2^z \quad . \tag{5.29}$$

Projected onto the eigenspace of H_{CR}^R where the control qubit is in $|C=0\rangle$, this Hamiltonian takes the typical Zeeman form $\vec{B}_C \cdot \vec{\sigma}_2/2$. The same holds in the other eigenspace where the control qubit is set to $|C=1\rangle$. Hence we have $(H_{CR}^R)_C = \vec{B}_C \cdot \vec{\sigma}_2/2$ where the

coefficients of $\vec{B}_{C=0,1}$ obey

$$J_{IX}^{\text{eff}} = \frac{B_0^x + B_1^x}{4} \quad , \qquad J_{ZX}^{\text{eff}} = \frac{B_0^x - B_1^x}{4} \quad , \tag{5.30a}$$

$$J_{IY}^{\text{eff}} = \frac{B_0^y + B_1^y}{4} \quad , \qquad J_{ZY}^{\text{eff}} = \frac{B_0^y - B_1^y}{4} \quad , \tag{5.30b}$$

$$J_{IZ}^{\text{eff}} = \frac{B_0^z + B_1^z}{4} \quad , \qquad J_{ZZ}^{\text{eff}} = \frac{B_0^z - B_1^z}{4} \quad . \tag{5.30c}$$

To find the interaction strengths J^{eff}, we thus need to know the coefficients of $\vec{B}_{C=0,1}$. They can be obtained from the data generated by the time evolution of the second spin $\langle\vec{\sigma}_2\rangle$: Using the Ehrenfest theorem in the Heisenberg picture, we have

$$\frac{\mathrm{d}}{\mathrm{d}t}\langle\vec{\sigma}_2\rangle_C = i\langle[\tfrac{1}{2}\vec{B}_C\cdot\vec{\sigma}_2, \vec{\sigma}_2]\rangle_C = \vec{B}_C \times \langle\vec{\sigma}_2\rangle_C = \underbrace{\begin{pmatrix} 0 & -B_C^z & B_C^y \\ B_C^z & 0 & -B_C^x \\ -B_C^y & B_C^x & 0 \end{pmatrix}}_{A_C} \langle\vec{\sigma}_2\rangle_C \quad . \tag{5.31}$$

Thus the time evolution of the second spin is governed by two separate Bloch equations

$$\langle\vec{\sigma}_2(t)\rangle_C = e^{A_C t}\langle\vec{\sigma}_2(0)\rangle_C \quad , \tag{5.32}$$

dependent on whether the control qubit is in $|C=0\rangle$ or $|C=1\rangle$. By fitting the coefficients of $\vec{B}_{C=0,1}$ through Eq. (5.32) to the expectation values of the second spin, we can then use Eqs. (5.30a)–(5.30c) to infer the parameters J^{eff} of H_{CR}^R.

The CR pulses that we apply to the control qubit are of three different kinds: The first is a constant irradiation of amplitude Ω, as defined in Eq. (5.25). The second pulse additionally uses the first 15 ns for a Gaussian turn-on and the last 15 ns for a Gaussian turn-off of width $\sigma = 5\,\text{ns}$ (cf. [SMC+16]). In addition to this, the third pulse uses the DRAG Y-only correction on the other quadrature as done in [CCG+11] (see also Eq. (5.21a)). Each pulse is applied for a time $t_g \in \{50\,\text{ns}, 100\,\text{ns}, 400\,\text{ns}\}$, and we sweep different amplitudes Ω up to $2\pi \times 160\,\text{MHz}$ which is necessarily smaller than the detuning Δ_{12} (see Tab. 5.3). As done in [SMC+16], we generate two data sets from the initial states $|00\rangle$ and $|10\rangle$.

One example of the time evolution of the second spin in a frame rotating at its Lamb-shifted frequency ω_{L2} together with the Bloch model fit is shown in Fig. 5.10. The gate time in this case is $t_g = 400\,\text{ns}$ and the CR amplitude is approx. $2\pi \times 130\,\text{MHz}$. The first thing to note is that the CR effect is clearly visible: If the control qubit is in $|0\rangle$ (first row), the target qubit rotates towards the negative y-axis (blue curve), and if the control qubit is in $|1\rangle$, the target rotates in the opposite direction. Hence the conditionality of the motion of the target qubit can be used for an entangling gate. Note also that the frequency of rotation is faster in the latter case. Comparing the constant (left) and the Gaussian-shaped (right) envelope of the CR drive, we further observe that a Gaussian rise and fall makes the evolution of the second spin a lot smoother. So in the case of a Gaussian-shaped pulse, the Bloch model given by Eq. (5.32) fits very well, even though the CR amplitude is relatively large. The reason for the deviation in the constant pulse case can be found by examining the immense leakage of the control qubit into the non-computational state $|2\rangle$ (last row of plots in Fig. 5.10). Interestingly, the leakage is still

quite high in the Gaussian-shaped case without compromising the CR effect. However, even though the leakage returns to 0 when the CR pulse is turned off, the difference between the cases $|C = 0\rangle$ and $|C = 1\rangle$ may cause problems if the gate is applied to superpositions of both states on the control qubit (note that the mathematical concept of unitary gates does not necessarily apply to faulty operations on the reduced two-qubit subspace, see also [DMH+02]). The DRAG correction does not significantly change this excitation. This is reasonable since the Gaussian makes up 30 ns of the pulse, which is too long for this DRAG correction to make a significant difference (see also the results of section 5.2.1). Furthermore, since the Gaussian turn-on is not symmetric, applying the derivative of the pulse to the other quadrature induces an additional rotation of the control qubit about the y-axis during the flattop of the CR pulse, so DRAG cannot be applied as easily as for the single-qubit gates. A solution would be to reduce the CR amplitude, although this further decreases the upper bound to the possible speed of the gate.

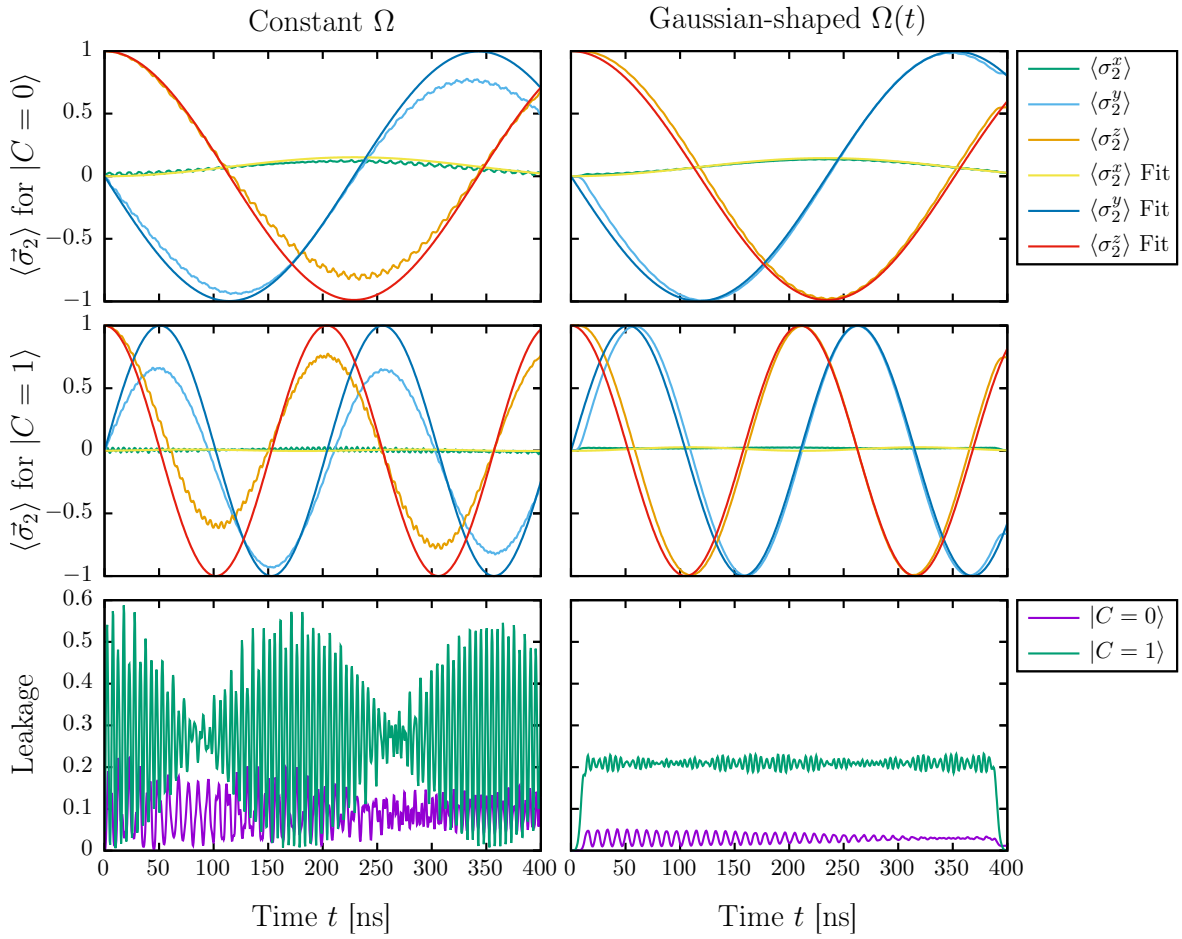

Figure 5.10.: Time evolution of the system during the application of a CR pulse for $t_g = 400\,\text{ns}$ and $\Omega = 2\pi \times 130\,\text{MHz}$, along with the fit defined by the Bloch model in Eq. (5.32). The first row shows the time evolution of the target qubit if the control qubit is in $|C = 0\rangle$, and the second row corresponds to $|C = 1\rangle$. The left plots correspond to CR pulses with a constant envelope, and the right plots correspond to a Gaussian-shaped envelope. In the last row, the respective leakage of the control qubit in terms of the probability to measure it in the non-computational state $|2\rangle$ is shown for both cases.

As explained above, the Bloch model fits yield the coefficients of the CR Hamiltonian given by Eq. (5.29). To compare the results with the two-level case, the procedure is also applied to the two-level spin model introduced in section 3.2. The resulting coefficients of the Hamiltonian as a function of the CR drive amplitude Ω for some representative configurations are shown in Fig. 5.11. We find that both the transmon and the spin model exhibit a clear dominance of the ZX term. The crosstalk term IX that is only present in the full transmon system is of similar magnitude. For smaller CR amplitudes, the perturbative result given by Eq. (5.28a) and Eq. (5.28b) describes the interaction strength reasonably well. The deviation from the linear increase for higher amplitudes has two reasons, namely Ω reaching the detuning Δ_{12} and the gradually increasing leakage shown in Fig. 5.10. For shorter gates with $t_g = 50\,\mathrm{ns}$ (the lower plots in Fig. 5.11), the effective interaction strengths J^{eff} deviate even more from the expectation given in Eq. (5.27). This can be traced back to the effect of the Gaussian turn-on and turn-off, each of which covering 15 ns of the total CR pulse. The higher ratio of rise/fall time to the actual flattop also results in a constant ZZ contribution independent of Ω. As expected, applying a DRAG correction does not significantly influence the performance. This might, however, be different for shorter rise times of the pulse [CDG+10]. Finally, the unexpected IY contribution measured in [SMC+16] is only marginally observable for shorter gate times. This suggests that the observed effect is indeed beyond the Hamiltonian evolution of the system.

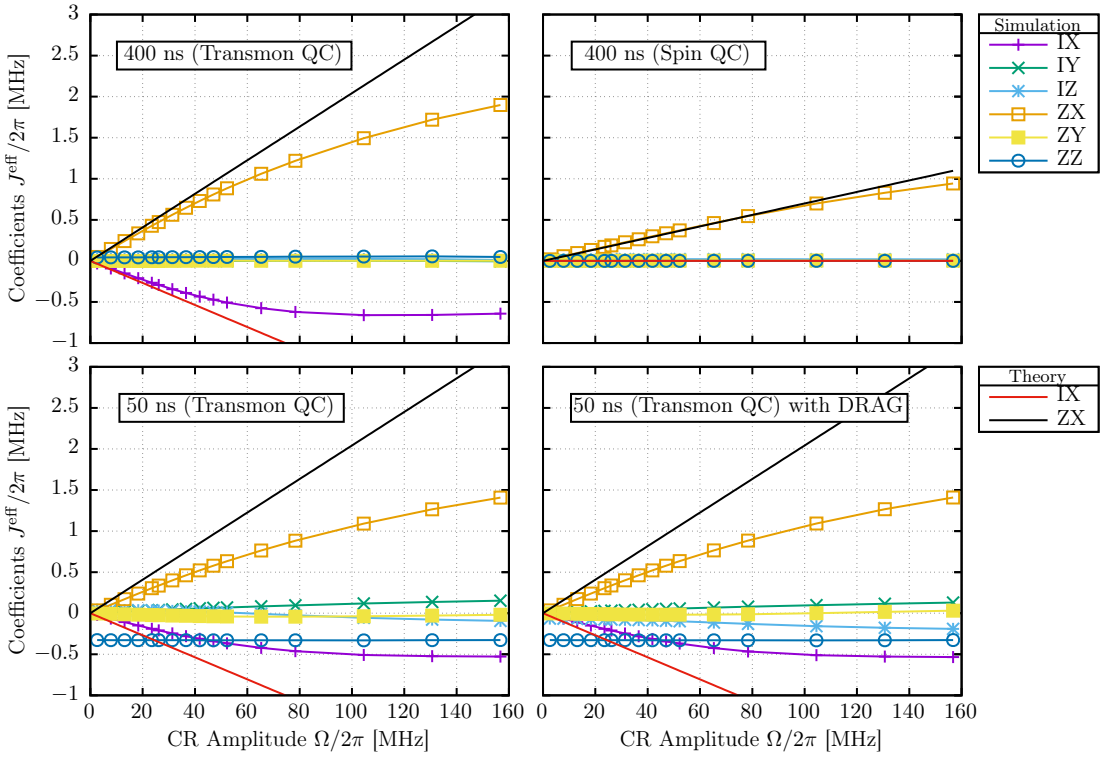

Figure 5.11.: Coefficients of the CR Hamiltonian given by Eq. (5.29) dependent on the drive amplitude. The upper plots correspond to the long Gaussian-shaped pulses ($t_g = 400\,\mathrm{ns}$) applied to the transmon quantum computer (left) and the simple two-qubit model (right). The lower plots are the results for shorter pulses ($t_g = 50\,\mathrm{ns}$), the right of which includes an additional DRAG correction as defined by Eq. (5.21a). The theoretical curves for the transmons are given by Eq. (5.28a) and Eq. (5.28b), and those for the spin model are given by Eq. (5.26).

As a last experiment, we analyze to which extent the effective interaction rate can be boosted by matching the resonance conditions mentioned above, i.e., when the detuning Δ_{12} between the transmons approaches the negative anharmonicity $-\delta_1$ of the control transmon (see Eq. (5.28b)). A stronger interaction rate J_{ZX}^{eff} is desirable since this decreases the entangling time $\pi/4J_{ZX}^{\text{eff}}$ such that the gate becomes faster. Therefore, we now vary the Josephson energy E_{J1} of the control transmon between $2\pi \times 10\,\text{GHz}$ and $2\pi \times 17\,\text{GHz}$ (cf. Tab. 5.3). This corresponds to detunings $\Delta_{12} = \omega_1 - \omega_2$ between $-2\pi \times 0.5\,\text{GHz}$ and $2\pi \times 0.9\,\text{GHz}$, including the critical points at $\pm\delta_{1/2}$ and 0 where most of the higher transmon levels of both transmons become aligned. For each detuning, we apply a CR pulse of $t_g = 400\,\text{ns}$ and $\Omega = 2\pi \times 26\,\text{MHz}$ and use the same procedure as before to measure H_{CR}^R given by Eq. (5.29). The results are shown in Fig. 5.12.

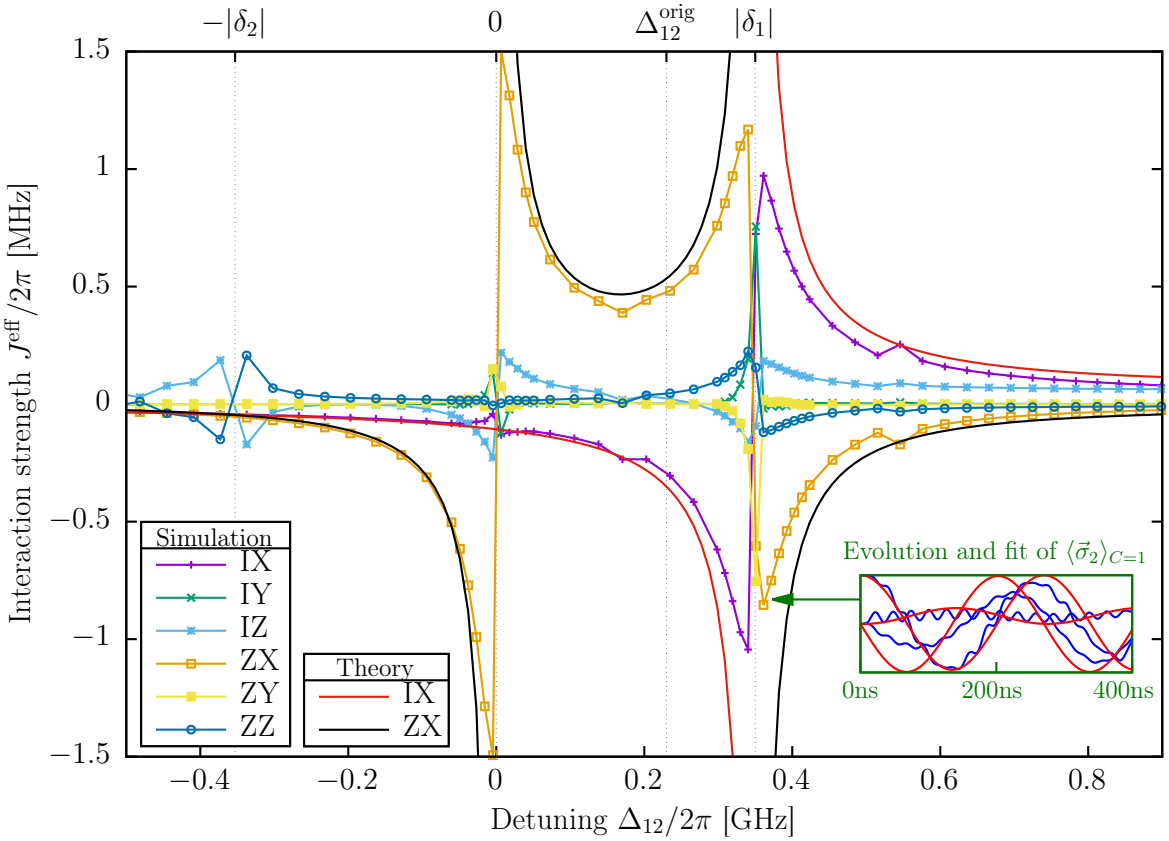

Figure 5.12.: Coefficients of the CR Hamiltonian given by Eq. (5.29) dependent on the qubit-qubit detuning $\Delta_{12} = \omega_1 - \omega_2$. The strongest contributions are ZX and IX, for which the perturbative predictions are taken from Eq. (5.28a) (red) and Eq. (5.28b) (black). Critical behavior can be observed at $\Delta_{12} \in \{0, |\delta_1|, -|\delta_2|\}$, hinting at specific resonance conditions. The additional label $\Delta_{12}^{\text{orig}}$ indicates the detuning of the original transmon frequencies used in all previous simulations (see Tab. 5.3). Inset: Time evolution of the three components of $\langle\vec{\sigma}_2\rangle_1$ (blue curves) and the three corresponding Bloch model fits given by Eq. (5.32) (red curves). Here we see that close to the critical detuning $\Delta_{12} = |\delta_1|$, there are additional sinusoidal modulations in the time evolution that cannot be accurately described by the Bloch model.

As predicted by the perturbative result for J_{IX}^{eff} in Eq. (5.28a) and J_{ZX}^{eff} in Eq. (5.28b), the interaction strength grows significantly around the critical detuning $\Delta_{12} = |\delta_1|$. At this point, the transition frequencies between $|m\rangle$ and $|m+1\rangle$ of the control transmon

match those between $|m-1\rangle$ and $|m\rangle$ of the target transmon, which is the resonance condition causing the divergence. The reason that the actual divergence is a bit weaker and is eventually cut off lies in the transmons not being perfect anharmonic oscillators, so the resonances dissolve for higher m. However, a look at the Bloch model fit shown in the inset of Fig. 5.12 reveals that the evolution of the second spin is not accurately described by H_{CR}^R anymore. Thus, for transmons produced around this critical detuning, it may be hard to calibrate the CR gate to high fidelity.

Additional care is also required between transmons whose detuning Δ_{12} is too close to 0. Despite the increased ZX contribution that Fig. 5.12 suggests, one still has to meet the requirement $\Omega < |\Delta_{12}|$. Again, this reduces the upper bound on the CR amplitude and thus limits the speed of the gate. Moreover, the driving of the control qubit becomes resonant, thereby tilting it away from $|C=0\rangle$ or $|C=1\rangle$ (note that this tilting is caused by the σ_1^x term from Eq. (5.27), which has been neglected in Eq. (5.29)). In this case, the projection of the CR Hamiltonian onto the two eigenspaces of the control qubit becomes invalid. However, this only means that this method of Hamiltonian tomography leaves its range of application; a suitable CR gate may still be realized under these circumstances.

The other regions around $\pm\delta_1/2$ or $3|\delta_1|/2$, however, show good agreement with the Bloch model and can be used to realize CR gates without further investigation.

The study of the CR Hamiltonian in Fig. 5.12 reveals another interesting physical feature, namely the occurrence of divergences in the other expansion coefficients of the CR Hamiltonian. These are obviously higher-order effects w.r.t. the perturbative results in Eq. (5.27). At $\Delta_{12} = \delta_2 \approx -2\pi \times 0.35\,\mathrm{GHz}$, the IZ and ZZ terms can even surpass the ZX and IX contributions. Physically, this condition expresses the point where the frequency of the control transmon matches the transition frequency between the states $|1\rangle$ and $|2\rangle$ of the target transmon.

So with all the additional effects occurring for transmons as opposed to the simple two-level spin system, how does one realize a proper CNOT gate? The first step is to precisely tune the amplitude and the gate time to the specific two sets of qubits. As we have seen, the CR effect is very sensitive to the frequencies of the transmons, so this must be done carefully for each of the interacting qubits in the gate calibration procedure. After that, the goal is to single out the ZX interaction as a primitive of the CNOT (more precisely, we have $\mathrm{CNOT} \propto \exp(i\pi\sigma_1^z\sigma_2^x/4)\,(Z_{-\pi/2} \otimes X_{-\pi/2})$ using the notation from appendix D). For this purpose, one needs to get rid of the IX contribution shown in Figs. 5.11 and 5.12. This is usually done using a simple spin-echo technique [CGC+13]. The additional contribution along ZZ occurring for smaller gate times and specific detunings are also addressed by this scheme [Gam13], as well as a ZI term resulting from off-resonant driving of the first qubit. Finally, to handle the IY and ZY contributions that do not commute with ZX, an additional driving of the target qubit is required [SMC+16]. It is an interesting subject of further research to apply all of these techniques to our system, in order to eventually identify all remaining sources of coherent errors in the realization of a high-fidelity CNOT gate between two fixed-frequency transmon qubits.

6. Conclusion

In this project, we have developed an implementation of efficient and unconditionally stable algorithms to solve the TDSE for various kinds of quantum computer hardware, accessible through an easy-to-use interface offering different types of visualizations. The algorithms are specifically tailored to key properties of the Hamiltonians. Thus we are able to simulate representative superconducting devices on the sub-picosecond scale, which is far out of reach for present diagonalization techniques. At the same time, the simulation results can be made arbitrarily precise such that they are only limited by double-precision floating-point arithmetic (15-16 significant decimal digits) [08]. Of course, since the Hilbert space grows exponentially in the number of qubits, a simulation at this level is only feasible for small systems of less than ten qubits, which is also the current state of the art in experimental implementations [KBF+15].

The Hamiltonians of our systems were chosen to model a large class of superconducting CPB qubits and ideal spin qubits. Special emphasis has been put on not making any approximation to the initial Hamiltonians. We want to stress that the simulated systems considered in this thesis work, by construction, exactly as quantum theory predicts. The software developed here is thus ideally suited to locate fundamental limitations and examine possible solutions in currently popular technologies. Examinations of these systems can thus be cheaply done without suffering from the fundamental limitations present in laboratories. For instance, couplings in a qubit system can be turned off at the push of a button, and different pulse-shaping techniques can be compared, with full access to the data produced in the entire time evolution. Analyzing this data can then provide the crucial insights that eventually lead to the right knowledge about how to achieve high-fidelity quantum gates.

On the other hand, effects observed in the simulation can give further inspiration about what to focus on in order to derive new analytical statements. Furthermore, it can be used to study the range of validity of common approximations done in analytical calculations. In that sense, analytical and computational work complement each other very well.

The particular kinds of superconducting systems that we studied were based on charge qubits and transmon qubits, controlled by capacitively coupled electric fields and inductively coupled magnetic fields. The coupling among the qubits was mediated by their capacitive interaction, transmission line resonators, and nonlinear inductances.

For charge qubits, we first examined a form of capacitive coupling that was the original motivation for the famous CR gate. Under a coherent Hamiltonian evolution, the system performed almost perfectly, showing the potential to realize high-fidelity universal two-qubit gates and to be accurately described in terms of an effective two-qubit Hamiltonian. This last fact is often taken for granted, but as we have seen for a type of strong Josephson-inductive coupling, this is not necessarily the case. The mathematical reason for that was found in the effective time evolution in the reduced two-qubit subspace where the coupling part was traced out. In general, this reduced evolution needs to be described in terms of Kraus operators and is not necessarily unitary if the system is too complex to be well

described in the reduced Hilbert space [KBD+83]. Furthermore, even if the description works reasonably well for the computational basis states (i.e. showing fidelities above a certain threshold), there may be superposition states pushing the error in fidelity far below this threshold. Similarly, the concept of unitarity w.r.t. faulty operations is nontrivial: A gate can perform almost perfectly on the basis states, while still producing big errors on superposition states.

For transmon qubits, we have investigated various techniques to shape the voltage pulses used to induce single-qubit rotations. The shapes were selected from constant, linear, Gaussian, and tangential envelopes. We verified that, due to the reduced anharmonicity of the transmon, constant pulses and simple Gaussian pulses for fast gate operations below 10 ns can excite higher energy levels of the transmon, thereby pushing the qubit out of its computational subspace. Analytic control methods such as DRAG [GMM+11] can be used to reduce this leakage. However, for the three types of DRAG corrections that we tested, a reduction of the leakage did not improve the fidelity of the gate in all cases. Especially for fast single-qubit gates, we found a trade-off between fidelity and leakage errors that has also been observed in recent experiments [CKQ+16]. However, by slowing down the gates to about 40 ns, all techniques performed equally well, scoring gate fidelities close to 100%. This is necessary since the gate fidelity is not a strong measure for the success of a gate: In terms of the spins on the Bloch sphere, we observed that fidelities about 95% can still mean that the spins are pointing about 30° away from the ideal result. It is worth mentioning that among all pulses we compared, a tangential shape always gave the best fidelities.

In addition to single-qubit gates for fixed-frequency transmons, we have made a deep study of the static coupling mediated by a transmission line resonator. By using a procedure to extract the optimal effective Hamiltonian describing the time evolution in the reduced two-qubit subspace, we computed the Lamb shift and the Bloch-Siegert shift of the qubit frequencies. We used the same procedure to find the optimal form of the exchange coupling between the qubits. This coupling is often assumed to be purely transverse of the type $\sigma_1^x\sigma_2^x + \sigma_1^y\sigma_2^y$, which can be derived under several approximations such as the RWA and the TLA. In contrast, for the transmon system under consideration, we found that the optimal description is dominated by $\sigma_1^x\sigma_2^x$ and contributions of the type $\sigma_1^y\sigma_2^y$ and $\sigma_1^z\sigma_2^z$ are smaller by almost two orders of magnitude. However, since the evolution in the reduced space is not perfectly unitary, these different types of couplings are hardly distinguishable in terms of fidelity during the first 400 ns.

Under a CR drive, we observed an entangling two-qubit interaction of the type $\sigma_1^z\sigma_2^x$ growing linearly in the amplitude of the driving field. For transmons, as opposed to a simple spin system with exchange interaction, the driving also induced an unconditional rotation of the type σ_2^x of similar magnitude. The strengths of both terms was found to saturate at higher amplitudes, thereby setting a limit to the speed of the gate. Although a Gaussian-shaped CR pulse can be successfully used to extend this limit, we also observed unexpected interactions emerging from the Hamiltonian evolution, especially for very short gate durations. Finally, we studied the CR Hamiltonian as a function of the detuning between the two transmons, where we found specific resonance conditions causing divergences in several interactions. Some of these are beyond first-order perturbative results, showing interesting new physical effects. However, due to the high sensitivity of the CR effect to the qubit-qubit detuning, there are two sides of the coin: As the detuning between two fabricated transmons is hard to determine in advance, they may either be located at a point where fast CNOT gates in both directions are easily doable, or where

optimizing such a gate to high fidelity remains a challenge requiring further research.

There are many directions in which the present work can be extended:

Regarding transmon qubits, it would be interesting to test new techniques to speed up single-qubit gates for weakly anharmonic systems [CKQ+16], possibly also including approaches from quantum control theory [PK02]. Similarly, both analytical and numerical studies can be made to find a deeper characterization of the actual resonator-mediated coupling between the transmons. Relating to this, as we have only studied single-mode resonators, it is certainly compelling to analyze the effects of other spurious modes in the resonator. For the CR gate and other popular schemes [MG14; MFM+16], the final objective would then be to identify and characterize all sources of coherent errors preventing high-fidelity fast CNOT gates between arbitrary transmons.

Another attractive option would be to extend our simulation algorithms to arbitrary linear and quadratic terms in the superconducting phase operator. In addition to CPB qubits, we could then also model promising flux qubit devices such as the fluxonium [MKG+09] which does not suffer from weak anharmonicity as much as the transmon. This also includes a fascinating recent design based on longitudinal coupling promising easy scalability [RD16a], as well as other classes of tunable inductive coupling schemes [KQC+16].

A typical qubit experiment comprises the three stages of initialization, computation, and measurement. As we have mainly focused on the computation part and the realization and evaluation of certain gate schemes, it would be an interesting project to add support for deeper studies of the other two stages to the program. This would allow a more accurate modeling of quantum computer hardware, providing the opportunity to optimize projective measurement or readout techniques or to study quantum feedback control [RD16b]. Additionally, the performance of small quantum error correction protocols under more realistic hardware conditions could be investigated.

Finally, a profitable complementary direction would be to adjust the software to employ the resources of massively parallel supercomputers. By making use of sophisticated optimization and parallelization techniques as done in [DMD+07], it would become feasible to simulate larger superconducting qubit systems. Such systems are now also seen within reach of experimental expertise [GCS15].

Appendices

A. The Josephson effects obtained from the simple tunneling Hamiltonian

In the following, we demonstrate how the Josephson effects in Eq. (2.6) and Eq. (2.7) can be derived from the simple tunneling Hamiltonian $H = -E_J \cos\hat{\varphi}$. There are of course many other derivations of the same equations (cf. [Jos62], [WS65], [FLS65] or [Mar04]); we have chosen this version because it is quite straightforward and follows standard concepts of Hamiltonian dynamics.

(DC) The DC Josephson effect makes a statement about the current I that we can measure across a Josephson junction. In quantum theory, it seems natural to understand it as the expectation value of some current operator $\hat{I}$ in an eigenstate of the Hamiltonian $|\varphi\rangle$. Thereby, the current operator is chosen as $\hat{I} = -2e\,\mathrm{d}\hat{n}/\mathrm{d}t$, measuring the number of Cooper pairs traveling across the junction and weighted with a charge of $-2e$. Thus we find in the Heisenberg picture

$$\begin{aligned}
\langle\varphi|\hat{I}|\varphi\rangle &= -2e\,\langle\varphi|\,\frac{\mathrm{d}\hat{n}}{\mathrm{d}t}\,|\varphi\rangle \\
&= \frac{2e}{\hbar} i\,\langle\varphi|\,[\hat{n}, H]\,|\varphi\rangle \\
&= \frac{eE_J}{\hbar} i\,\langle\varphi|\,\left(\left[\hat{n}, e^{i\hat{\varphi}}\right] + \left[\hat{n}, e^{-i\hat{\varphi}}\right]\right)|\varphi\rangle \\
&= \frac{eE_J}{\hbar} i\,\langle\varphi|\,\left(e^{i\hat{\varphi}} - e^{-i\hat{\varphi}}\right)|\varphi\rangle \\
&= \frac{2eE_J}{\hbar}\sin\varphi \quad ,
\end{aligned}$$

where we can identify the critical current $I_c = 2eE_J/\hbar$ such that $I = I_c \sin\varphi$ as in Eq. (2.6).

(AC) The AC Josephson effect describes the time dependence of $\varphi(t)$ under an external voltage bias V. This causes an additional linear term in the Hamiltonian given by the electrostatic interaction energy of a charge in an external electric field:

$$H = -E_J \cos\hat{\varphi} + 2eV\hat{n} \quad .$$

The desired effect can then be obtained from solving the TDSE for an initial state $|\Psi(0)\rangle = |\varphi_0\rangle$, and it corresponds to the expectation value $\varphi(t) = \langle\Psi(t)|\hat{\varphi}|\Psi(t)\rangle$. Hence we start from the TDSE

$$i\hbar\frac{\partial}{\partial t}\,|\Psi(t)\rangle = \left(-\tfrac{E_J}{2}\left(e^{i\hat{\varphi}} + e^{-i\hat{\varphi}}\right) + 2eV\hat{n}\right)|\Psi(t)\rangle \quad .$$

To get rid of the linear term, we make an ansatz of the form $|\Psi(t)\rangle = e^{-i\omega t\hat{n}}\,|\widetilde{\Psi}(t)\rangle$ with $\omega = 2eV/\hbar$. Note that, in quantum information terminology, this transformation is equivalent to moving to a rotating frame by means of the rotation $R = e^{-i\omega t\hat{n}}$ such that

$H \mapsto R^\dagger H R - i\hbar R^\dagger \dot{R}$. Using the similarity relation

$$R^\dagger e^{i\hat{\varphi}} R = e^{i\omega t\hat{n}}\, e^{i\hat{\varphi}}\, e^{-i\omega t\hat{n}} = e^{[i\omega t\hat{n},\,\cdot\,]} e^{i\hat{\varphi}} = \sum_{k=0}^{\infty} \frac{(i\omega t)^k}{k!} \underbrace{\left[\hat{n}, e^{i\hat{\varphi}}\right]_k}_{e^{i\hat{\varphi}}} = e^{i(\hat{\varphi}+\omega t)} \quad ,$$

where $[A,B]_k := [A,\,\cdot\,]^k(B) = [A,[A,\cdots[A,B]]]$, we thus obtain a modified TDSE for $|\widetilde{\Psi}(t)\rangle$ where the linear dependence on $\hat{n}$ has gone, i.e.

$$i\hbar\frac{\partial}{\partial t}|\widetilde{\Psi}(t)\rangle = -\tfrac{E_J}{2}\left(e^{i(\hat{\varphi}+\omega t)} + e^{-i(\hat{\varphi}+\omega t)}\right)|\widetilde{\Psi}(t)\rangle \quad .$$

Since the only operator occurring on the right-hand side is $\hat{\varphi}$, and the initial state $|\widetilde{\Psi}(0)\rangle = |\varphi_0\rangle$ is an eigenstate of it, the solution can easily be calculated from the time evolution operator (note that the corresponding Hamiltonians for different times commute):

$$\begin{aligned}|\widetilde{\Psi}(t)\rangle &= e^{-\frac{i}{\hbar}\int_0^t -\frac{E_J}{2}\left(e^{i(\hat{\varphi}+\omega\tau)}+e^{-i(\hat{\varphi}+\omega\tau)}\right)\mathrm{d}\tau}|\varphi_0\rangle \\ &= e^{\frac{i}{\hbar}E_J\int_0^t \cos(\varphi_0+\omega\tau)\,\mathrm{d}\tau}|\varphi_0\rangle\end{aligned}$$

The integration in the prefactor could be carried out explicitly; but as it is only a phase that drops out in the expectation values, we just leave it there. Using the translation relation $e^{-i\omega t\hat{n}}|\varphi_0\rangle = |\varphi_0+\omega t\rangle$ that can be derived from Eq. (2.14), we finally obtain

$$|\Psi(t)\rangle = e^{\frac{i}{\hbar}E_J\int_0^t \cos(\varphi_0+\omega\tau)\,\mathrm{d}\tau}|\varphi_0+\omega t\rangle \quad .$$

So the voltage bias made the system evolve as $|\Psi(t)\rangle \propto |\varphi_0+\omega t\rangle$, which yields the expectation value $\varphi(t) = \varphi_0 + \omega t$ and thus the AC Josephson effect $\dot{\varphi} = \omega = 2e/\hbar V$ as in Eq. (2.7).

B. Dirac's notation and the domains of number and phase operators

Using Dirac's notation, we have the freedom of representation independence to formulate physical laws. Thus we distinguish between the abstract ket $|\psi\rangle \in \mathcal{H}$ and, e.g., its representations in the phase space $\psi(\varphi) = \langle\varphi|\psi\rangle$ or in the number space $\psi_n = \langle n|\varphi\rangle$. By inserting completeness relations $\mathbb{1} = \sum_n |n\rangle\langle n| = \int d\varphi\, |\varphi\rangle\langle\varphi|$, we can easily convert between different representations, thereby implicitly switching between Hilbert spaces isomorphic to $\mathcal{H}$. Especially for the evaluation of inner products for matrix elements, we can choose the representation that allows the easiest calculation.

A problem arises now when we work in infinite-dimensional Hilbert spaces, for which not all operators we use are immediately well-defined on the entire Hilbert space. In such a case, we can arrive at different results depending on which representation we use to perform our calculation. This can produce apparent paradoxes such as the one we encountered in Eq. (2.19).

An elaborate treatment of the problem can be found in [Rei14], and for other interesting kinds of apparent paradoxes we refer to [Gie00]. To explain and avoid the paradox in Eq. (2.19), we need to consider the concept of a domain of an operator as used in functional analysis. In the following, we thus review the concepts of functional analysis as presented in [GS03].

Definition 1 (Domain)**.** For a linear operator $A : \mathcal{D}(A) \to \mathcal{H}$, the domain $\mathcal{D}(A) \leq \mathcal{H}$ is a dense linear subspace including only states $|\psi\rangle$ for which the image $A|\psi\rangle$ is well-defined and still belongs to the Hilbert space. This means that $\mathcal{D}(A)$ is a subspace of the maximal domain of definition, i.e.

$$\mathcal{D}(A) \leq \mathcal{D}_{\max}(A) := \{|\psi\rangle \in \mathcal{H} \,:\, A|\psi\rangle \in \mathcal{H}\} \quad .$$

In infinite-dimensional Hilbert spaces, also the self-adjointness that we so naturally assume for any physical observable (and the simplicity of working with Dirac's notation suggests that) is not necessarily given. There is a sharp difference between self-adjointness and Hermiticity. Before we get to that, we need to first fix the definition of an operator's adjoint.

Definition 2 (Adjoint)**.** The adjoint $A^\dagger$ of an operator A is the unique operator satisfying $\langle\psi|A^\dagger|\phi\rangle = \langle\phi|A|\psi\rangle^*$ for all $|\psi\rangle \in \mathcal{D}(A)$, where $|\phi\rangle$ lies in the domain

$$\mathcal{D}(A^\dagger) := \{|\phi\rangle \in \mathcal{H} \,:\, |\langle\phi|A|\psi\rangle| \leq \text{const}(\phi)\, |\langle\psi|A|\psi\rangle| \text{ for all } |\psi\rangle \in \mathcal{D}(A)\} \quad .$$

For the previous statements to make sense, we have to understand a matrix element $\langle\phi|A|\psi\rangle$ in bra-ket notation always as the inner product of $|\phi\rangle$ and $A|\psi\rangle$, i.e., A always acts on the right. This is one of the drawbacks in the notation that can lead to apparent contradictions. This problem does not arise in the common notation used by mathematicians to define the adjoint, namely $\langle A^\dagger\phi, \psi\rangle = \langle\phi, A\psi\rangle$. Therefore we will allow this notation in the following.

Definition 3 (Hermitian)**.** An operator A is Hermitian if for all $|\psi\rangle, |\phi\rangle \in \mathcal{D}(A)$:

$$\langle A\phi, \psi\rangle = \langle\phi, A\psi\rangle \quad .$$

Definition 4 (Self-adjoint)**.** An operator A is self-adjoint if it is Hermitian and

$$\mathcal{D}(A) = \mathcal{D}(A^\dagger) \quad .$$

Thus an operator can be Hermitian without being self-adjoint. The important thing to check here is the domain. In fact, it may happen that $\mathcal{D}(A^\dagger) = \{0\}$ even if the operator is well-defined on $\mathcal{D}(A) \neq \{0\}$.

The question is now, which domain is the proper domain for the operators that we work with? Since the operators we have in mind are eventually needed to be self-adjoint (and thus Hermitian) for the interpretation of observables to make sense, a reasonable choice is the largest subspace of $\mathcal{D}_{\max}(A)$ on which the operators are Hermitian. Hence, the proper domain for the operator A representing a physical observable is

$$\mathcal{D}(A) := \{|\psi\rangle \in \mathcal{D}_{\max}(A) \,:\, \langle A\phi, \psi\rangle = \langle \phi, A\psi\rangle \text{ for all } |\phi\rangle \in \mathcal{D}_{\max}(A)\} \quad .$$

One can easily prove that this space is a dense linear subspace of $\mathcal{H}$, and we have the following composition rules for sums and products of operators:

$$\begin{aligned} \mathcal{D}(A+B) &= \mathcal{D}(A) \cap \mathcal{D}(B) \\ \mathcal{D}(AB) &= \{|\psi\rangle \in \mathcal{D}(B) \,:\, B\,|\psi\rangle \in \mathcal{D}(A)\} \quad . \end{aligned}$$

Regarding the operators in question, we now proceed to compute the domains of $\hat{\varphi}$, $\hat{n}$, and combinations thereof.

The Hilbert space $\mathcal{H}$ we use is the space of all states $|\psi\rangle$ whose complex-valued wave function ψ given by $\psi(\varphi) = \langle \varphi|\psi\rangle$ is square-integrable on the domain $[0, 2\pi]$, i.e. $\psi \in L^2([0,2\pi]) \stackrel{\sim}{=} \mathcal{H}$. This restriction has to be put on $\mathcal{H}$ for physical expectation values defined by inner products to make sense.

Since $\hat{\varphi}$ is a bounded operator, its domain is the entire Hilbert space $\mathcal{H}$. The same holds for its adjoint $\hat{\varphi}^\dagger$, so we have $\mathcal{D}(\hat{\varphi}) = \mathcal{D}(\hat{\varphi}^\dagger) = \mathcal{H}$. The number operator $\hat{n}$, however, works as a derivative $i\frac{\partial}{\partial\varphi}$ on ψ which imposes additional conditions on ψ. The obvious one is $\psi' \in L^2([0,2\pi])$. For the other condition, we examine the Hermiticity of $\hat{n}$:

$$\begin{aligned} \langle \hat{n}\phi, \psi\rangle - \langle \phi, \hat{n}\psi\rangle &= \int_0^{2\pi} d\phi \, (i\phi'(\varphi)^*\psi(\varphi) - i\phi(\varphi)^*\psi'(\varphi)) \\ &= i\,(\phi(2\pi)^*\psi(2\pi) - \phi(0)^*\psi(0)) \quad . \end{aligned}$$

Hence we also need the wave functions to fulfill periodic boundary conditions, and we have

$$\mathcal{D}(\hat{n}) = \left\{|\psi\rangle \in \mathcal{H} \,:\, \psi, \psi' \in L^2([0,2\pi]) \text{ and } \psi(0) = \psi(2\pi)\right\} \quad .$$

To obtain the proper domains of $\hat{\varphi}\hat{n}$ and $\hat{n}\hat{\varphi}$, we need to apply the composition rules:

$$\begin{aligned}
\mathcal{D}(\hat{\varphi}\hat{n}) &= \{|\psi\rangle \in \mathcal{D}(\hat{n}) \,:\, \hat{n}\,|\psi\rangle \in \mathcal{D}(\hat{\varphi})\} \\
&= \{|\psi\rangle \in \mathcal{D}(\hat{n}) \,:\, \hat{n}\,|\psi\rangle \in \mathcal{H}\} \\
&= \mathcal{D}(\hat{n}) \\
\mathcal{D}(\hat{n}\hat{\varphi}) &= \{|\psi\rangle \in \mathcal{D}(\hat{\varphi}) \,:\, \hat{\varphi}\,|\psi\rangle \in \mathcal{D}(\hat{n})\} \\
&= \left\{|\psi\rangle \in \mathcal{H} \,:\, \varphi\psi, (\varphi\psi)' \in L^2([0,2\pi]) \text{ and } 0\psi(0) = 2\pi\psi(2\pi)\right\} \\
&= \left\{|\psi\rangle \in \mathcal{H} \,:\, \varphi\psi, \varphi\psi' \in L^2([0,2\pi]) \text{ and } 0 = \psi(2\pi)\right\} \quad .
\end{aligned}$$

Now there is already a big restriction since many wave functions do not vanish at 2π. Note that, interestingly, the periodic boundary condition we needed for $\hat{n}$ is not required for the product operator $\hat{n}\hat{\varphi}$ anymore. However, due to the composition rule for sums of operators, it reappears in the commutator $[\hat{n}, \hat{\varphi}] = \hat{n}\hat{\varphi} - \hat{\varphi}\hat{n}$:

$$\begin{aligned}
\mathcal{D}([\hat{n}, \hat{\varphi}]) &= \mathcal{D}(\hat{n}\hat{\varphi}) \cap \mathcal{D}(\hat{\varphi}\hat{n}) \\
&= \left\{|\psi\rangle \in \mathcal{H} \,:\, \psi, \psi' \in L^2([0,2\pi]) \text{ and } \psi(0) = \psi(2\pi) = 0\right\} \quad .
\end{aligned}$$

In summary:

$$\begin{aligned}
\mathcal{D}(\hat{\varphi}) &= \mathcal{D}\left(\hat{\varphi}^\dagger\right) = \mathcal{H} \\
\mathcal{D}(\hat{n}) &= \left\{|\psi\rangle \,:\, \psi, \psi' \in L^2([0,2\pi]) \text{ and } \psi(0) = \psi(2\pi)\right\} \\
\mathcal{D}(\hat{\varphi}\hat{n}) &= \left\{|\psi\rangle \,:\, \psi, \psi' \in L^2([0,2\pi]) \text{ and } \psi(0) = \psi(2\pi)\right\} = \mathcal{D}(\hat{n}) \\
\mathcal{D}(\hat{n}\hat{\varphi}) &= \left\{|\psi\rangle \,:\, \varphi\psi, \varphi\psi' \in L^2([0,2\pi]) \text{ and } \psi(2\pi) = 0\right\} \\
\mathcal{D}([\hat{n}, \hat{\varphi}]) &= \left\{|\psi\rangle \,:\, \psi, \psi' \in L^2([0,2\pi]) \text{ and } \psi(0) = \psi(2\pi) = 0\right\} \quad .
\end{aligned}$$

As described in section 2.1.3, this result explains the apparent paradox.

C. Matrix norms on finite-dimensional vector spaces

For the sake of completeness, we recite some of the properties of elementary matrix norms from basic linear algebra [Mey07]. They are mainly used in the description of numerical algorithms in section 4.1.

For a complex matrix $A \in \mathbb{C}^{n\times n}$, a norm $\|A\|$ is a non-negative real number measuring the "size" of the matrix. It has to satisfy certain properties such as being positive definite and homogeneous, and it needs to fulfill the triangle inequality.

It is useful to distinguish between operator norms that are induced by appropriate vector norms (hence also called *induced norms*), and *entry-wise norms* that are defined by direct arithmetic operations on the matrix coefficients.

Induced norms: The induced norm $\|A\|_p$ for $p \in \mathbb{N}$ is defined as

$$\|A\|_p := \sup_{\vec{x}\in\mathbb{C}^{n\times n}\setminus\{0\}} \frac{\|A\vec{x}\|_p}{\|\vec{x}\|_p} \quad ,$$

where $\|\vec{x}\|_p = (\sum_{i=1}^{n}|x_i|^p)^{1/p}$ is the inducing vector norm. From the definition, we immediately see that the matrix norm and its corresponding vector norm are compatible, in the sense that

$$\|Ax\|_p \leq \|A\|_p \|x\|_p \quad .$$

The special case of $p = 1$ produces the maximum absolute column sum of A, and the definition can be extended to $p = \infty$ resulting in the maximum absolute row sum. The important case for the algorithms in section 4.1 is $p = 2$, which is also called the *spectral norm* with the corresponding vector norm simply being the *Euclidean norm*. It is given by the largest singular value of A, i.e., the square root of the largest eigenvalue of $A^\dagger A$

$$\|A\|_2 = \sqrt{\max\{\mathrm{spec}(A^\dagger A)\}} \quad .$$

If A is Hermitian ($A = A^\dagger$), this expression simply amounts to the largest absolute eigenvalue of A. So $\|A\|_2$ can be used as a tight upper bound on the action of A on a vector.

Entry-wise norms: An entry-wise norm $\|A\|_p^{\mathrm{ew}}$ can be computed by putting all coefficients of A in one vector $\vec{a} \in \mathbb{C}^{n^2}$ and evaluating its vector norm $\|\vec{a}\|_p$, so we have

$$\|A\|_p^{\mathrm{ew}} = \left(\sum_{i,j=1}^{N}|a_{ij}|^p\right)^{\frac{1}{p}} \quad .$$

The important case here is again $p = 2$, which defines the *Frobenius norm* $\|\cdot\|_F = \|\cdot\|_2^{\mathrm{ew}}$ that is also known as the *Hilbert-Schmidt norm*. It satisfies $\|A\|_F = \sqrt{\mathrm{Tr}\, A^\dagger A}$ and one can further show that $\|A\|_2 \leq \|A\|_F$. Thus it is also compatible with the Euclidean vector norm $\|A\vec{x}\|_2 \leq \|A\|_F \|\vec{x}\|_2$.

D. Summary of single-qubit rotations

In the following, we present the definition of the matrices and transformations of common single-qubit rotation gates $R^{\vec{n}}(\varphi)$ on the Bloch sphere, relevant in the development of the application described in chapter 4. It can also be used as a lookup table to easily verify quantum circuits.

The gate $R^{\vec{n}}(\varphi) = e^{i\varphi\vec{n}\cdot\vec{S}}$ (where $\vec{S} = \vec{\sigma}/2$ is the spin vector of Pauli matrices) rotates an arrow about the unit vector $\vec{n}$ on the Bloch sphere. The angle of rotation is given by φ, and the sense of rotation is clockwise when looking onto the arrow head from above. This means that, in a right-handed coordinate system, if we use the left thumb to point along $\vec{n}$, then the curl of the fingers represents the motion. This convention is known as the *left-hand rule*. Conversely, the expression $e^{-i\varphi n\cdot\vec{S}}$ corresponds to the *right-hand rule*.

Using the algebraic analog to Euler's formula in the Pauli algebra

$$R^{\vec{n}}(\varphi) = e^{i\varphi\vec{n}\cdot\vec{S}} = e^{i\frac{\varphi}{2}\vec{n}\cdot\vec{\sigma}} = \cos\frac{\varphi}{2} + i\sin\frac{\varphi}{2}\,\vec{n}\cdot\vec{\sigma} \quad ,$$

we obtain for the three elementary rotations

$$R^x(\varphi) = \begin{pmatrix} \cos\frac{\varphi}{2} & i\sin\frac{\varphi}{2} \\ i\sin\frac{\varphi}{2} & \cos\frac{\varphi}{2} \end{pmatrix}, \quad R^y(\varphi) = \begin{pmatrix} \cos\frac{\varphi}{2} & \sin\frac{\varphi}{2} \\ -\sin\frac{\varphi}{2} & \cos\frac{\varphi}{2} \end{pmatrix}, \quad R^z(\varphi) = \begin{pmatrix} e^{i\frac{\varphi}{2}} & 0 \\ 0 & e^{-i\frac{\varphi}{2}} \end{pmatrix}.$$

The most common rotations are those where $\varphi = \pm\pi/2$. Using the notation for the Pauli eigenstates

$$|0\rangle = \begin{pmatrix} 1 \\ 0 \end{pmatrix}, \qquad |+\rangle = \tfrac{1}{\sqrt{2}}\begin{pmatrix} 1 \\ 1 \end{pmatrix}, \qquad |\circlearrowright\rangle = \tfrac{1}{\sqrt{2}}\begin{pmatrix} 1 \\ i \end{pmatrix},$$
$$|1\rangle = \begin{pmatrix} 0 \\ 1 \end{pmatrix}, \qquad |-\rangle = \tfrac{1}{\sqrt{2}}\begin{pmatrix} 1 \\ -1 \end{pmatrix}, \qquad |\circlearrowleft\rangle = \tfrac{1}{\sqrt{2}}\begin{pmatrix} 1 \\ -i \end{pmatrix},$$

the actions of these rotations for $\varphi = \pi/2$ on each state are

$$X_{\pi/2} = R^x(\tfrac{\pi}{2}) = \tfrac{1}{\sqrt{2}}\begin{pmatrix} 1 & i \\ i & 1 \end{pmatrix}: \quad \begin{aligned} &|0\rangle \mapsto |\circlearrowright\rangle, \quad |+\rangle \mapsto e^{i\frac{\pi}{4}}|+\rangle, \quad |\circlearrowright\rangle \mapsto i|1\rangle \\ &|1\rangle \mapsto i|\circlearrowleft\rangle, \quad |-\rangle \mapsto e^{-i\frac{\pi}{4}}|-\rangle, \quad |\circlearrowleft\rangle \mapsto |0\rangle \end{aligned}$$

$$Y_{\pi/2} = R^y(\tfrac{\pi}{2}) = \tfrac{1}{\sqrt{2}}\begin{pmatrix} 1 & 1 \\ -1 & 1 \end{pmatrix}: \quad \begin{aligned} &|0\rangle \mapsto |-\rangle, \quad |+\rangle \mapsto |0\rangle, \quad |\circlearrowright\rangle \mapsto e^{i\frac{\pi}{4}}|\circlearrowright\rangle \\ &|1\rangle \mapsto |+\rangle, \quad |-\rangle \mapsto -|1\rangle, \quad |\circlearrowleft\rangle \mapsto e^{-i\frac{\pi}{4}}|\circlearrowleft\rangle \end{aligned}$$

$$Z_{\pi/2} = R^z(\tfrac{\pi}{2}) = e^{i\frac{\pi}{4}}\begin{pmatrix} 1 & 0 \\ 0 & -i \end{pmatrix}: \quad \begin{aligned} &|0\rangle \mapsto e^{i\frac{\pi}{4}}|0\rangle, \quad |+\rangle \mapsto e^{i\frac{\pi}{4}}|\circlearrowleft\rangle, \quad |\circlearrowright\rangle \mapsto e^{i\frac{\pi}{4}}|+\rangle \\ &|1\rangle \mapsto e^{-i\frac{\pi}{4}}|1\rangle, \quad |-\rangle \mapsto e^{i\frac{\pi}{4}}|\circlearrowright\rangle, \quad |\circlearrowleft\rangle \mapsto e^{i\frac{\pi}{4}}|-\rangle \end{aligned}$$

Using this list, the inverse rotations for $\varphi = -\pi/2$ can be found by reading the arrows "$\mapsto$" from right to left.

E. Effective Hamiltonians for Josephson-inductive coupling

Auxiliary functions

```
expandto[expr_, var_List, order_] :=
 Module[{t}, Normal@Series[expr /. (# → # t & /@ var), {t, 0, order}] /. t → 1]
dropconstants[varpattern_] := DeleteCases[#, term_ /; ! MemberQ[term, varpattern, Infinity]] &
twolevelapproximation = {Cos[φi_] → 1/2 σxi, Sin[φi_] → 1/2 σyi};
pauli = {σxn_^e_ → σxn^Mod[e,2], σyn_^e_ → σyn^Mod[e,2]};
```

Steps of the derivation in [YTN03]

```
eliminatecoupling[U_, order_] :=
 Module[{current, eliminateφ0, Uwithoutφ0, Ufinal},
  (*from (9) to (11)*)
  current = expandto[∂φ0 U, {φ0}, 1];
  eliminateφ0 = Solve[0 == current, {φ0}] // First // First;
  (*from (11) to (12)*)
  Uwithoutφ0 = expandto[U /. eliminateφ0, {η1, η2}, order];
  Ufinal = (Uwithoutφ0 // TrigExpand) /. twolevelapproximation /. pauli // FullSimplify // Expand //
    dropconstants[σxi_ | σyi_]
 ]
```

Before the variable transformation

```
U = Sum[(-2 EJ0 ηi (Cos[φi] + Cos[φ0 - φi + ϕex])), {i, 2}] - EJ0 Cos[φ0]
```

$$-2\,EJ_0\,\eta_1\,(\cos(\varphi_0-\varphi_1+\phi ex)+\cos(\varphi_1))-2\,EJ_0\,\eta_2\,(\cos(\varphi_0-\varphi_2+\phi ex)+\cos(\varphi_2))+EJ_0\,(-\cos(\varphi_0))$$

```
eliminatecoupling[U, 1] /. ϕex → 0
eliminatecoupling[U, 2] /. ϕex → π
```

$$-2\,EJ_0\,\eta_1\,\sigma x_1-2\,EJ_0\,\eta_2\,\sigma x_2$$

$$-EJ_0\,\eta_1\,\eta_2\,\sigma y_1\,\sigma y_2$$

After the variable transformation

```
U = Sum[(-4 EJ0 ηi Cos[φi] Cos[φ0/2 - ϕex/2]), {i, 2}] - EJ0 Cos[φ0]
```

$$-4\,EJ_0\,\eta_1\cos(\varphi_1)\cos\left(\frac{\phi ex}{2}-\frac{\varphi_0}{2}\right)-4\,EJ_0\,\eta_2\cos(\varphi_2)\cos\left(\frac{\phi ex}{2}-\frac{\varphi_0}{2}\right)+EJ_0\,(-\cos(\varphi_0))$$

```
eliminatecoupling[U, 1] /. ϕex → 0
eliminatecoupling[U, 2] /. ϕex → π
```

$$-2\,EJ_0\,\eta_1\,\sigma x_1-2\,EJ_0\,\eta_2\,\sigma x_2$$

$$-EJ_0\,\eta_1\,\eta_2\,\sigma x_1\,\sigma x_2$$

F. Graphical user interface and visualizations

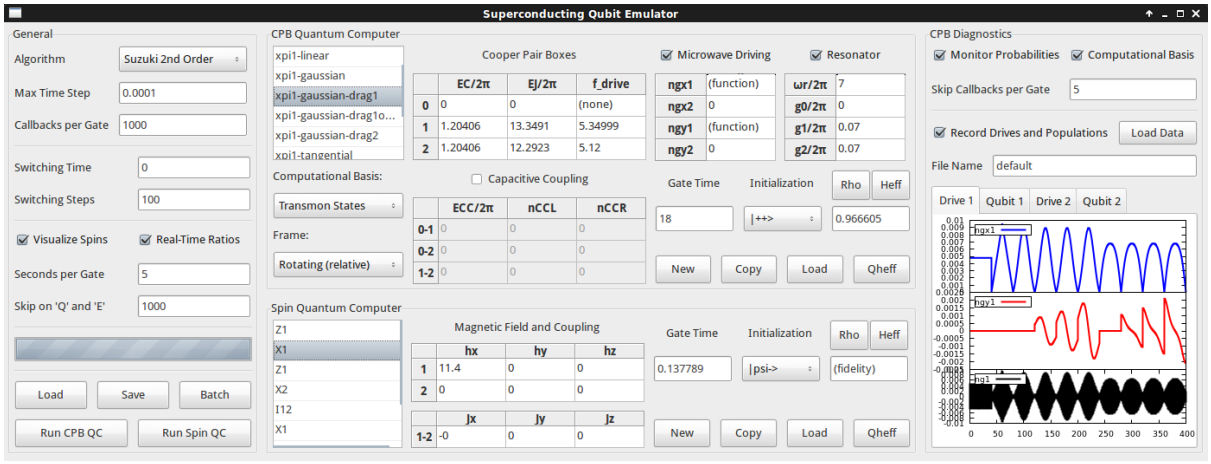

Figure F.1.: Screenshot of the graphical user interface.

On the left side of the interface shown in Fig. F.1, general settings such as the algorithm and the time step to solve the TDSE can be chosen (cf. section 4.1). Setups can be loaded, saved and run by clicking the corresponding buttons, and a progress bar shows the progress of the current simulation. In the middle, programs for the CPB model (top) and the spin model (bottom) as defined in chapter 3 can be configured. Each gate in both lists is defined by its parameters in the Hamiltonian shown in the corresponding grids, and the value "(function)" indicates an explicit time dependence on the corresponding parameter. Drop-down menus to select the computational basis and a rotating frame are beneath the CPB gates. Next to the initial states, real-time evaluations of the gate fidelity given by Eq. (5.6) and the effective Hamiltonian fidelity given by Eq. (5.9) are shown. The procedure from section 4.4 can be triggered with the "Qheff" button. On the right, specific diagnostics such as state populations and applied voltages can be monitored. The program also supports running complete sets of experiments by using the "Batch" button, which was done to generate the data shown in Fig. 5.5../../software/sqe/drives/plots/fidelity-40ns-1.

The settings above the progress bar can be used to trigger the animations on the Bloch sphere shown in Fig. F.2. Each scene is rendered in a three-dimensional space. The user can move the camera through the scene using the mouse and the keyboard. A light on top of the camera illuminates the scene. Additional information such as the gate name, the fidelity, and the spin coordinates are printed in green, and a coordinate system is rendered on the bottom left of the screen.

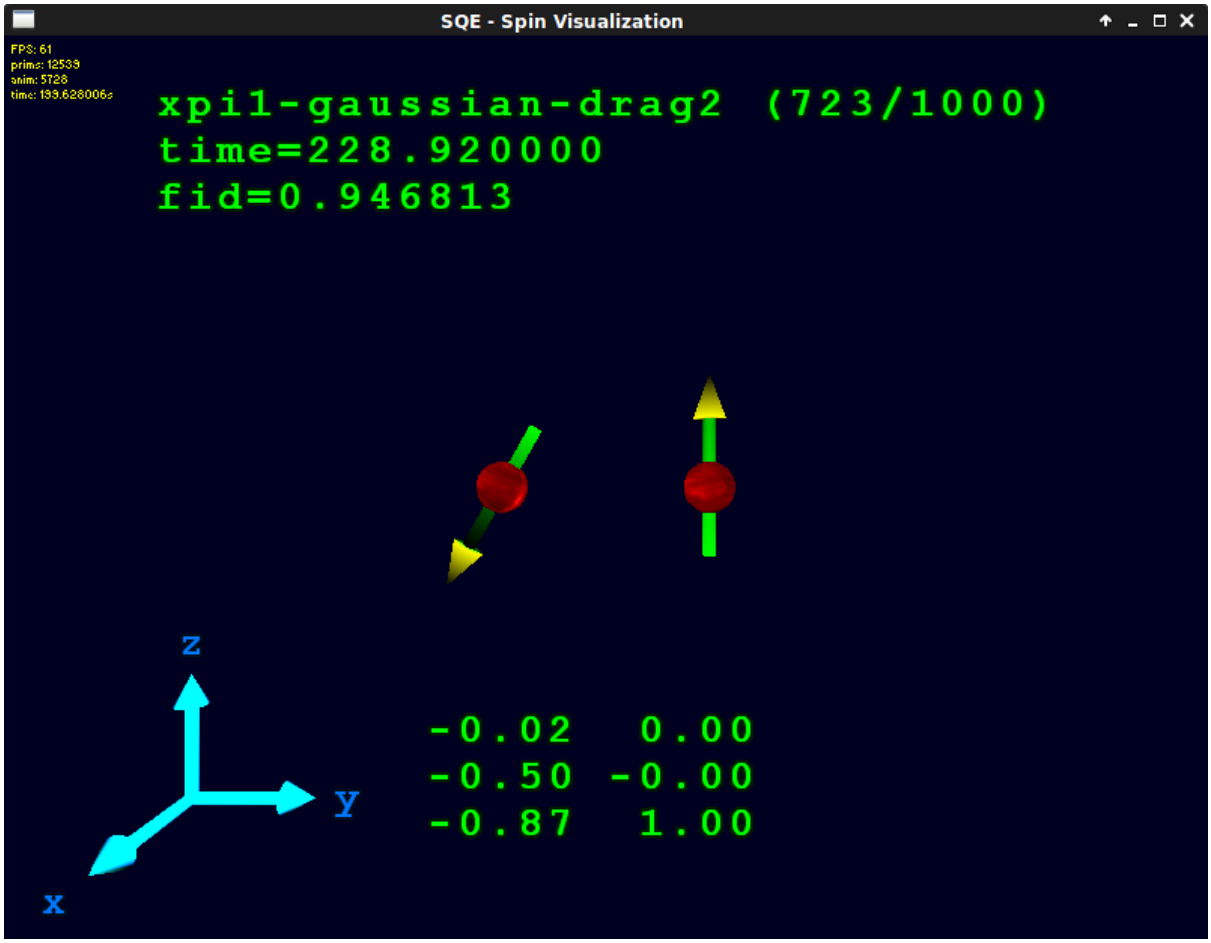

Figure F.2.: Visualization of the spins on the Bloch sphere during the operation $X_\pi^1 |00\rangle$ with a Gaussian pulse and DRAG corrections to second order (see section 5.2.1). Below the arrows representing the spins, the expectation values $\langle \sigma_i^{x/y/z} \rangle$ of the Pauli operators are printed. The axes correspond to the coordinate system rendered on the bottom left. Above the arrows, diagnostic information such as the gate title, the time of the animation, and the fidelity is shown. At the time depicted in this screenshot, we see that the fidelity of the final state $|10\rangle$ is already close to 95%, even though the left spin still has $\langle \sigma_1^y \rangle = -0.5 \neq 0$. The gate and the time displayed on the screen can be selected from the keyboard, and camera and light sources are controllable using the mouse.

Bibliography

[08] *IEEE Standard for Floating-Point Arithmetic*. Microprocessor Standards Committee of the IEEE Computer Society. 3 Park Avenue, New York, NY 10016-5997, USA: The Institute of Electrical and Electronics Engineers, Inc., 2008, 1 (cit. on pp. 36, 85).

[ABB+99] E. Anderson, Z. Bai, C. Bischof, S. Blackford, J. Demmel, J. Dongarra, J. Du Croz, A. Greenbaum, S. Hammerling, A. McKenney, and D. Sorensen. *LAPACK Users' Guide: Third Edition*. Software, Environments, and Tools. Society for Industrial and Applied Mathematics, 1999 (cit. on p. 37).

[ADS01] J. Anglin, P. Drummond, and A. Smerzi. "Exact quantum phase model for mesoscopic Josephson junctions". *Phys. Rev. A* 64 (2001), 063605 (cit. on p. 11).

[AES82] V. Ambegaokar, U. Eckern, and G. Schön. "Quantum Dynamics of Tunneling between Superconductors". *Phys. Rev. Lett.* 48 (1982), 1745 (cit. on p. 12).

[AS64] M. Abramowitz and I. A. Stegun. *Handbook of Mathematical Functions with Formulas, Graphs, and Mathematical Tables*. ninth Dover printing, tenth GPO printing. New York: Dover, 1964 (cit. on pp. 25, 44).

[BCS57] J. Bardeen, L. N. Cooper, and J. R. Schrieffer. "Theory of Superconductivity". *Phys. Rev.* 108 (1957), 1175 (cit. on p. 5).

[BDL11] S. Bravyi, D. P. DiVincenzo, and D. Loss. "Schrieffer-Wolff transformation for quantum many-body systems". *Annals of Physics* 326 (2011), 2793 (cit. on p. 51).

[BF04] H. Bruus and K. Flensberg. *Many-Body Quantum Theory in Condensed Matter Physics: An Introduction*. Oxford Graduate Texts. OUP Oxford, 2004 (cit. on p. 36).

[BHW+04] A. Blais, R.-S. Huang, A. Wallraff, S. M. Girvin, and R. J. Schoelkopf. "Cavity quantum electrodynamics for superconducting electrical circuits: An architecture for quantum computation". *Phys. Rev. A* 69 (2004), 062320 (cit. on pp. 27, 74).

[Bis10] L. S. Bishop. "Circuit Quantum Electrodynamics". PhD thesis. Yale University, 2010 (cit. on p. 13).

[BK15] S. Benjamin and J. Kelly. "Superconducting qubits: Solving a wonderful problem". *Nat. Mater.* 14 (2015), 561 (cit. on pp. 2, 28).

[BKD04] G. Burkard, R. H. Koch, and D. P. DiVincenzo. "Multilevel quantum description of decoherence in superconducting qubits". *Phys. Rev. B* 69 (2004), 064503 (cit. on pp. 2, 13).

[BKM+13] R. Barends, J. Kelly, A. Megrant, D. Sank, E. Jeffrey, Y. Chen, Y. Yin, B. Chiaro, J. Mutus, C. Neill, P. O'Malley, P. Roushan, J. Wenner, T. C. White, A. N. Cleland, and J. M. Martinis. "Coherent Josephson Qubit Suitable for Scalable Quantum Integrated Circuits". *Phys. Rev. Lett.* 111 (2013), 080502 (cit. on p. 28).

[BKM+14] R. Barends, J. Kelly, A. Megrant, A. Veitia, D. Sank, E. Jeffrey, T. C. White, J. Mutus, A. G. Fowler, B. Campbell, Y. Chen, Z. Chen, B. Chiaro, A. Dunsworth, C. Neill, P. O'Malley, P. Roushan, A. Vainsencher, J. Wenner, A. N. Korotkov, A. N. Cleland, and J. M. Martinis. "Superconducting quantum circuits at the surface code threshold for fault tolerance". *Nature* 508 (2014), 500 (cit. on p. 28).

[BS40] F. Bloch and A. Siegert. "Magnetic Resonance for Nonrotating Fields". *Phys. Rev.* 57 (1940), 522 (cit. on pp. 70, 75).

[BV07] S. M. Barnett and J. A. Vaccaro. *The Quantum Phase Operator: A Review*. Series in Optics and Optoelectronics. Taylor & Francis, 2007 (cit. on p. 9).

[BVJ+98] V. Bouchiat, D. Vion, P. Joyez, D. Esteve, and M. H. Devoret. "Quantum coherence with a single Cooper pair". *Physica Scripta* 1998 (1998), 165 (cit. on p. 18).

[Cal14] A. O. Caldeira. *An Introduction to Macroscopic Quantum Phenomena and Quantum Dissipation*. Cambridge University Press, 2014 (cit. on p. 8).

[CCE+06] G. Chen, D. A. Church, B. G. Englert, C. Henkel, B. Rohwedder, M. O. Scully, and M. S. Zubairy. *Quantum Computing Devices: Principles, Designs, and Analysis*. Chapman & Hall/CRC Applied Mathematics & Nonlinear Science. CRC Press, 2006 (cit. on p. 5).

[CCG+11] J. M. Chow, A. D. Córcoles, J. M. Gambetta, C. Rigetti, B. R. Johnson, J. A. Smolin, J. R. Rozen, G. A. Keefe, M. B. Rothwell, M. B. Ketchen, and M. Steffen. "Simple All-Microwave Entangling Gate for Fixed-Frequency Superconducting Qubits". *Phys. Rev. Lett.* 107 (2011), 080502 (cit. on pp. 3, 57, 73, 79).

[CDG+10] J. M. Chow, L. DiCarlo, J. M. Gambetta, F. Motzoi, L. Frunzio, S. M. Girvin, and R. J. Schoelkopf. "Optimized driving of superconducting artificial atoms for improved single-qubit gates". *Phys. Rev. A* 82 (2010), 040305 (cit. on pp. 3, 67, 73, 81).

[CF12] G. Costa and G. Fogli. *Symmetries and Group Theory in Particle Physics: An Introduction to Space-Time and Internal Symmetries*. Lecture Notes in Physics. Springer Berlin Heidelberg, 2012 (cit. on p. 50).

[CGC+12] J. M. Chow, J. M. Gambetta, A. D. Córcoles, S. T. Merkel, J. A. Smolin, C. Rigetti, S. Poletto, G. A. Keefe, M. B. Rothwell, J. R. Rozen, M. B. Ketchen, and M. Steffen. "Universal Quantum Gate Set Approaching Fault-Tolerant Thresholds with Superconducting Qubits". *Phys. Rev. Lett.* 109 (2012), 060501 (cit. on pp. 3, 67, 70).

[CGC+13] A. D. Córcoles, J. M. Gambetta, J. M. Chow, J. A. Smolin, M. Ware, J. Strand, B. L. T. Plourde, and M. Steffen. "Process verification of two-qubit quantum gates by randomized benchmarking". *Phys. Rev. A* 87 (2013), 030301 (cit. on pp. 3, 78, 83).

[CGM+14] J. M. Chow, J. M. Gambetta, E. Magesan, D. W. Abraham, A. W. Cross, B. R. Johnson, N. A. Masluk, C. A. Ryan, J. A. Smolin, S. J. Srinivasan, and M. Steffen. "Implementing a strand of a scalable fault-tolerant quantum computing fabric". *Nat. Commun.* 5 (2014), 4015 (cit. on pp. 3, 67, 73).

[Che07] G. Chen. *Quantum Computing Devices: Principles, Designs, and Analysis*. Chapman and Hall/CRC Applied Mathematics and Nonlinear Science Series. Chapman & Hall/CRC, 2007 (cit. on pp. 8, 16).

[Cho10] J. M. Chow. "Quantum Information Processing with Superconducting Qubits". PhD thesis. Yale University, 2010 (cit. on p. 74).

[CKQ+16] Z. Chen, J. Kelly, C. Quintana, R. Barends, B. Campbell, Y. Chen, B. Chiaro, A. Dunsworth, A. G. Fowler, E. Lucero, E. Jeffrey, A. Megrant, J. Mutus, M. Neeley, C. Neill, P. J. J. O'Malley, P. Roushan, D. Sank, A. Vainsencher, J. Wenner, T. C. White, A. N. Korotkov, and J. M. Martinis. "Measuring and Suppressing Quantum State Leakage in a Superconducting Qubit". *Phys. Rev. Lett.* 116 (2016), 020501 (cit. on pp. 67, 70, 73, 86, 87).

[CMS+15] A. Corcoles, E. Magesan, S. J. Srinivasan, A. W. Cross, M. Steffen, J. M. Gambetta, and J. M. Chow. "Demonstration of a quantum error detection code using a square lattice of four superconducting qubits". *Nat. Commun.* 6 (2015), 6979 (cit. on pp. 3, 28, 67, 73).

[CN68] P. Carruthers and M. M. Nieto. "Phase and Angle Variables in Quantum Mechanics". *Rev. Mod. Phys.* 40 (1968), 411 (cit. on pp. 9, 10).

[Cot02] A. Cottet. "Implementation of a quantum bit in a superconducting circuit". PhD thesis. Université Paris VI, 2002 (cit. on p. 26).

[CSM+15] J. M. Chow, S. J. Srinivasan, E. Magesan, A. D. Córcoles, D. W. Abraham, J. M. Gambetta, and M. Steffen. "Characterizing a four-qubit planar lattice for arbitrary error detection". *Proc. SPIE* 9500 (2015). Ed. by E. Donkor, A. R. Pirich, and M. Hayduk, 95001G (cit. on pp. 3, 28).

[DBE95] D. Deutsch, A. Barenco, and A. Ekert. "Universality in Quantum Computation". *Proceedings of the Royal Society of London A: Mathematical, Physical and Engineering Sciences* 449 (1995), 669 (cit. on p. 33).

[DBK+00] D. P. DiVincenzo, D. Bacon, J. Kempe, G. Burkard, and K. B. Whaley. "Universal quantum computation with the exchange interaction". *Nature* 408 (2000), 339 (cit. on pp. 3, 33).

[DeR87] H. De Raedt. "Product formula algorithms for solving the time dependent Schrödinger equation". *Computer Physics Reports* 7 (1987), 1 (cit. on pp. 2, 37, 38, 40, 47).

[Dev97] M. Devoret. "Quantum Fluctuations in Electrical Circuits". *Fluctuations Quantiques/Quantum Fluctuations*. Ed. by S. Reynaud, E. Giacobino, and J. Zinn-Justin. 1997, 351 (cit. on pp. 13, 15).

[DiV00] D. P. DiVincenzo. "The Physical Implementation of Quantum Computation". *Fortschritte der Physik* 48 (2000), 771 (cit. on p. 1).

[DiV95] D. P. DiVincenzo. "Two-bit gates are universal for quantum computation". *Phys. Rev. A* 51 (1995), 1015 (cit. on pp. 3, 33).

[DKD+15a] H. De Raedt, M. I. Katsnelson, H. C. Donker, and K. Michielsen. "Quantum theory as a description of robust experiments: application to Stern-Gerlach and Einstein-Podolsky-Rosen-Bohm experiments". *Proc. SPIE* 9570 (2015), 957002 (cit. on p. 11).

[DKD+15b] H. De Raedt, M. I. Katsnelson, H. C. Donker, and K. Michielsen. "Quantum theory as a description of robust experiments: Derivation of the Pauli equation". *Annals of Physics* 359 (2015), 166 (cit. on p. 11).

[DKM14] H. De Raedt, M. I. Katsnelson, and K. Michielsen. "Quantum theory as the most robust description of reproducible experiments". *Annals of physics* 347 (2014), 45 (cit. on pp. 1, 11).

[DKM16] H. De Raedt, M. I. Katsnelson, and K. Michielsen. "Quantum theory as plausible reasoning applied to data obtained by robust experiments". *Philosophical Transactions of the Royal Society A: Mathematical, Physical and Engineering Sciences* 374 (2016), 20150233 (cit. on p. 11).

[DKR+16] H. C. Donker, M. I. Katsnelson, H. D. Raedt, and K. Michielsen. "Logical inference approach to relativistic quantum mechanics: Derivation of the Klein-Gordon equation". *Annals of Physics* 372 (2016), 74 (cit. on p. 11).

[DM06] H. De Raedt and K. Michielsen. "Computational Methods for Simulating Quantum Computers". *Handbook of Theoretical and Computational Nanotechnology, Vol. 3: Quantum and molecular computing, quantum simulations, Chapter 1, pp. 1-48, M. Rieth and W. Schommers eds., American Scientific Publisher, Los Angeles* (2006) (cit. on pp. 35, 36, 38, 43, 48).

[DMD+07] K. De Raedt, K. Michielsen, H. De Raedt, B. Trieu, G. Arnold, M. Richter, T. Lippert, H. Watanabe, and N. Ito. "Massively parallel quantum computer simulator". *Computer Physics Communications* 176 (2007), 121 (cit. on pp. 43, 87).

[DMH+02] H. De Raedt, K. Michielsen, A. Hams, S. Miyashita, and K. Saito. "Quantum spin dynamics as a model for quantum computer operation". *The European Physical Journal B - Condensed Matter and Complex Systems* 27 (2002), 15 (cit. on pp. 36, 80).

[DMP+07] J. W. Demmel, O. A. Marques, B. N. Parlett, and C. Vömel. *Performance and Accuracy of LAPACK's Symmetric Tridiagonal Eigensolvers*. Tech. rep. 183. LAPACK Working Note, 2007 (cit. on p. 37).

[DP14] A. De and L. P. Pryadko. "Dynamically corrected gates for qubits with always-on Ising couplings: Error model and fault tolerance with the toric code". *Phys. Rev. A* 89 (2014), 032332 (cit. on p. 73).

[ESA84] U. Eckern, G. Schön, and V. Ambegaokar. "Quantum dynamics of a superconducting tunnel junction". *Phys. Rev. B* 30 (1984), 6419 (cit. on p. 12).

[Fey82] R. P. Feynman. "Simulating physics with computers". *Int. J. Theor. Phys.* 21 (1982), 467 (cit. on p. 28).

[FLS65] R. P. Feynman, R. B. Leighton, and M. L. Sands. *The Feynman Lectures on Physics*. The Feynman Lectures on Physics v. 3. Addison-Wesley Publishing Company, 1965 (cit. on pp. 11, 91).

[GAC+05] N. Gebhardt, T. Alten, A. F. Celis, and J. Goewert. *Irrlicht Engine - A free open source 3d engine*. http://irrlicht.sourceforge.net/. 2005 (cit. on p. 50).

[GAL+12] P. C. de Groot, S. Ashhab, A. Lupaşcu, L. DiCarlo, F. Nori, C. J. P. M. Harmans, and J. E. Mooij. "Selective darkening of degenerate transitions for implementing quantum controlled-NOT gates". *New J. Phys.* 14 (2012), 073038 (cit. on pp. 3, 77).

[Gam13] J. M. Gambetta. *Control of Superconducting Qubits*. Lecture Notes of the 44th IFF Spring School. Ed. by David DiVincenzo. Schriften des Forschungszentrums Juelich. 2013 (cit. on pp. 26, 27, 66–68, 73, 74, 78, 83).

[GCS15] J. M. Gambetta, J. M. Chow, and M. Steffen. "Building logical qubits in a superconducting quantum computing system" (2015). arXiv:1510.04375 (cit. on pp. 1–3, 26, 28, 87).

[Gie00] F. Gieres. "Mathematical surprises and Dirac's formalism in quantum mechanics". *Reports on Progress in Physics* 63 (2000), 1893 (cit. on pp. 10, 93).

[Gir11] S. M. Girvin. "Circuit QED: superconducting qubits coupled to microwave photons". *Les Houches, Session XCVI* (2011), 22 (cit. on pp. 15, 24, 27).

[GJ10] G. Guennebaud and B. Jacob. *Eigen v3*. http://eigen.tuxfamily.org. 2010 (cit. on p. 37).

[GK05] C. Gerry and P. Knight. *Introductory Quantum Optics*. Cambridge University Press, 2005 (cit. on p. 13).

[GMM+11] J. M. Gambetta, F. Motzoi, S. T. Merkel, and F. K. Wilhelm. "Analytic control methods for high-fidelity unitary operations in a weakly nonlinear oscillator". *Phys. Rev. A* 83 (2011), 012308 (cit. on pp. 3, 67, 69, 70, 86).

[GS03] S. J. Gustafson and I. M. Sigal. *Mathematical Concepts of Quantum Mechanics*. Universitext (Berlin. Print). Springer, 2003 (cit. on pp. 10, 93).

[IBM16] IBM. *Quantum Experience*. 2016. URL: `http://www.research.ibm.com/quantum` (cit. on pp. 3, 28, 66).

[JC63] E. Jaynes and F. Cummings. "Comparison of quantum and semiclassical radiation theories with application to the beam maser". *Proc. IEEE* 51 (1963), 89 (cit. on p. 74).

[JJ07] D. James and J. Jerke. "Effective Hamiltonian theory and its applications in quantum information". *Canadian Journal of Physics* 85 (2007), 625 (cit. on p. 51).

[Jos62] B. D. Josephson. "Possible new effects in superconductive tunnelling". *Physics Letters* 1 (1962), 251 (cit. on pp. 2, 6, 91).

[Jos74] B. D. Josephson. "The discovery of tunnelling supercurrents". *Rev. Mod. Phys.* 46 (1974), 251 (cit. on p. 6).

[KBD+83] K. Kraus, A. Böhm, J. Dollard, and W. Wootters. *States, Effects, and Operations Fundamental Notions of Quantum Theory*. Vol. 190. Lecture notes in physics. Springer-Verlag Berlin, 1983 (cit. on pp. 52, 86).

[KBF+15] J. Kelly, R. Barends, A. G. Fowler, A. Megrant, E. Jeffrey, T. C. White, D. Sank, J. Y. Mutus, B. Campbell, Y. Chen, Z. Chen, B. Chiaro, A. Dunsworth, I.-C. Hoi, C. Neill, P. J. J. O'Malley, C. Quintana, P. Roushan, A. Vainsencher, J. Wenner, A. N. Cleland, and J. M. Martinis. "State preservation by repetitive error detection in a superconducting quantum circuit". *Nature* 519 (2015), 66 (cit. on pp. 1, 3, 28, 85).

[KQC+16] D. Kafri, C. Quintana, Y. Chen, A. Shabani, J. M. Martinis, and H. Neven. "Tunable inductive coupling of superconducting qubits in the strongly nonlinear regime" (2016). arXiv:1606.08382 (cit. on p. 87).

[KYG+07] J. Koch, T. M. Yu, J. Gambetta, A. A. Houck, D. I. Schuster, J. Majer, A. Blais, M. H. Devoret, S. M. Girvin, and R. J. Schoelkopf. "Charge-insensitive qubit design derived from the Cooper pair box". *Phys. Rev. A* 76 (2007), 042319 (cit. on pp. 2, 24–27, 61, 66).

[Lan13] N. K. Langford. "Circuit QED - Lecture Notes" (2013). arxiv:1310.1897 (cit. on pp. 5, 8, 9).

[LCP08] J. Li, K. Chalapat, and G. S. Paraoanu. "Entanglement of superconducting qubits via microwave fields: Classical and quantum regimes". *Phys. Rev. B* 78 (2008), 064503 (cit. on pp. 57–59, 61, 74).

[LL35] F. London and H. London. "The Electromagnetic Equations of the Supraconductor". *Proceedings of the Royal Society A: Mathematical, Physical and Engineering Sciences* 149 (1935), 71 (cit. on p. 5).

[Llo93] S. Lloyd. "A Potentially Realizable Quantum Computer". *Science* 261 (1993), 1569 (cit. on p. 33).

[LM92] D. Loss and K. Mullen. "Commutation relations for periodic operators". *Journal of Physics A: Mathematical and General* 25 (1992), L235 (cit. on p. 10).

[Mar04] J. M. Martinis. "Superconducting qubits and the physics of Josephson junctions". *Les Houches* 79 (2004), 487 (cit. on p. 91).

[MCG+07] J. Majer, J. M. Chow, J. M. Gambetta, J. Koch, B. R. Johnson, J. A. Schreier, L. Frunzio, D. I. Schuster, A. A. Houck, A. Wallraff, A. Blais, M. H. Devoret, S. M. Girvin, and R. J. Schoelkopf. "Coupling superconducting qubits via a cavity bus". *Nature* 449 (2007), 443 (cit. on pp. 27, 74).

[Mey07] C. D. Meyer. *Matrix Analysis and Applied Linear Algebra*. Cambridge University Press, 2007 (cit. on p. 96).

[MFM+16] D. C. McKay, S. Filipp, A. Mezzacapo, E. Magesan, J. M. Chow, and J. M. Gambetta. "A universal gate for fixed-frequency qubits via a tunable bus" (2016). arxiv:1604.03076 (cit. on p. 87).

[MG14] J. M. Martinis and M. R. Geller. "Fast adiabatic qubit gates using only σ_z control". *Phys. Rev. A* 90 (2014), 022307 (cit. on pp. 28, 87).

[MGR+09] F. Motzoi, J. M. Gambetta, P. Rebentrost, and F. K. Wilhelm. "Simple Pulses for Elimination of Leakage in Weakly Nonlinear Qubits". *Phys. Rev. Lett.* 103 (2009), 110501 (cit. on pp. 2, 67, 69).

[MKG+09] V. E. Manucharyan, J. Koch, L. I. Glazman, and M. H. Devoret. "Fluxonium: Single Cooper-Pair Circuit Free of Charge Offsets". *Science* 326 (2009), 113 (cit. on p. 87).

[ML03] C. Moler and C. V. Loan. "Nineteen Dubious Ways to Compute the Exponential of a Matrix, Twenty-Five Years Later". *SIAM Rev.* 45 (2003), 3 (cit. on p. 43).

[NC11] M. A. Nielsen and I. L. Chuang. *Quantum Computation and Quantum Information: 10th Anniversary Edition*. New York, NY, USA: Cambridge University Press, 2011 (cit. on pp. 1, 32, 49, 50, 52).

[Nie02] M. A. Nielsen. "A simple formula for the average gate fidelity of a quantum dynamical operation". *Physics Letters A* 303 (2002), 249 (cit. on p. 59).

[OBK+15] P. J. J. O'Malley, R. Babbush, I. D. Kivlichan, J. Romero, J. R. McClean, R. Barends, J. Kelly, P. Roushan, A. Tranter, N. Ding, B. Campbell, Y. Chen, Z. Chen, B. Chiaro, A. Dunsworth, A. G. Fowler, E. Jeffrey, A. Megrant, J. Y. Mutus, C. Neill, C. Quintana, D. Sank, A. Vainsencher, J. Wenner, T. C. White, P. V. Coveney, P. J. Love, H. Neven, A. Aspuru-Guzik, and J. M. Martinis. "Scalable Quantum Simulation of Molecular Energies" (2015). arxiv:1512.06860 (cit. on p. 28).

[Par06] G. S. Paraoanu. "Microwave-induced coupling of superconducting qubits". *Phys. Rev. B* 74 (2006), 140504 (cit. on pp. 3, 51, 57–59).

[PK02] J. P. Palao and R. Kosloff. "Quantum Computing by an Optimal Control Algorithm for Unitary Transformations". *Phys. Rev. Lett.* 89 (2002), 188301 (cit. on p. 87).

[PRN+14] V. Paulisch, H. Rui, H. K. Ng, and B.-G. Englert. "Beyond adiabatic elimination: A hierarchy of approximations for multi-photon processes". *Eur. Phys. J. Plus* 129 (2014), 12 (cit. on p. 51).

[PTV+07] W. H. Press, S. A. Teukolsky, W. T. Vetterling, and B. P. Flannery. *Numerical Recipes 3rd Edition: The Art of Scientific Computing*. New York, NY, USA: Cambridge University Press, 2007 (cit. on p. 44).

[RBD05] C. Rigetti, A. Blais, and M. Devoret. "Protocol for Universal Gates in Optimally Biased Superconducting Qubits". *Phys. Rev. Lett.* 94 (2005), 240502 (cit. on pp. 57, 66).

[RBH01] J. M. Raimond, M. Brune, and S. Haroche. "Manipulating quantum entanglement with atoms and photons in a cavity". *Rev. Mod. Phys.* 73 (2001), 565 (cit. on p. 74).

[RD10] C. Rigetti and M. Devoret. "Fully microwave-tunable universal gates in superconducting qubits with linear couplings and fixed transition frequencies". *Phys. Rev. B* 81 (2010), 134507 (cit. on pp. 3, 57, 77).

[RD16a] S. Richer and D. DiVincenzo. "Circuit design implementing longitudinal coupling: A scalable scheme for superconducting qubits". *Phys. Rev. B* 93 (2016), 134501 (cit. on p. 87).

[RD16b] D. Ristè and L. DiCarlo. "Digital Feedback Control". *Superconducting Devices in Quantum Optics*. Ed. by H. R. Hadfield and G. Johansson. Cham: Springer International Publishing, 2016, 187 (cit. on p. 87).

[Rei14] H. Reinhard. “On Heisenberg’s Uncertainty Principle and the CCR”. 48 (2014), 447 (cit. on p. 93).

[Rei15] D. J. Reilly. “Engineering the quantum-classical interface of solid-state qubits”. *Npj Quantum Information* 1 (2015), 15011 (cit. on pp. 2, 28).

[RGP+12] C. Rigetti, J. M. Gambetta, S. Poletto, B. L. T. Plourde, J. M. Chow, A. D. Córcoles, J. A. Smolin, S. T. Merkel, J. R. Rozen, G. A. Keefe, M. B. Rothwell, M. B. Ketchen, and M. Steffen. “Superconducting qubit in a waveguide cavity with a coherence time approaching 0.1 ms”. *Phys. Rev. B* 86 (2012), 100506 (cit. on p. 75).

[Ric13] S. Richer. “Perturbative analysis of two-qubit gates on transmon qubits”. Master’s thesis. RWTH Aachen, 2013 (cit. on p. 77).

[Rig09] C. T. Rigetti. “Quantum Gates for Superconducting Qubits”. PhD thesis. Yale University, 2009 (cit. on pp. 50, 75).

[RPH+15] D. Ristè, S. Poletto, M.-Z. Huang, A. Bruno, V. Vesterinen, O.-P. Saira, and L. DiCarlo. “Detecting bit-flip errors in a logical qubit using stabilizer measurements”. *Nat. Commun.* 6 (2015), 6983 (cit. on p. 28).

[SBM+16] S. Sheldon, L. S. Bishop, E. Magesan, S. Filipp, J. M. Chow, and J. M. Gambetta. “Characterizing errors on qubit operations via iterative randomized benchmarking”. *Phys. Rev. A* 93 (2016), 012301 (cit. on pp. 28, 67, 70, 73).

[SDE+13] R. Schutjens, F. A. Dagga, D. J. Egger, and F. K. Wilhelm. “Single-qubit gates in frequency-crowded transmon systems”. *Phys. Rev. A* 88 (2013), 052330 (cit. on p. 73).

[Sho94] P. W. Shor. “Algorithms for quantum computation: discrete logarithms and factoring”. *Proceedings of the 35th Annual Symposium on the Foundations of Computer Science* (1994), 124 (cit. on p. 1).

[SM99] A. Sørensen and K. Mølmer. “Quantum Computation with Ions in Thermal Motion”. *Phys. Rev. Lett.* 82 (1999), 1971 (cit. on p. 74).

[SMC+16] S. Sheldon, E. Magesan, J. M. Chow, and J. M. Gambetta. “Procedure for systematically tuning up crosstalk in the cross resonance gate” (2016). arXiv:1603.04821 (cit. on pp. 2, 3, 28, 57, 73, 77–79, 81, 83).

[SMK77] M. Suzuki, S. Miyashita, and A. Kuroda. “Monte Carlo Simulation of Quantum Spin Systems. I”. *Progress of Theoretical Physics* 58 (1977), 1377 (cit. on p. 38).

[SMO+15] Y. Salathé, M. Mondal, M. Oppliger, J. Heinsoo, P. Kurpiers, A. Poto čnik, A. Mezzacapo, U. Las Heras, L. Lamata, E. Solano, S. Filipp, and A. Wallraff. “Digital Quantum Simulation of Spin Models with Circuit Quantum Electrodynamics”. *Phys. Rev. X* 5 (2015), 021027 (cit. on p. 74).

[Str04] F. W. Strauch. “Theory of Superconducting Phase Qubits”. PhD thesis. Digital Repository at the University of Maryland: University of Maryland, 2004 (cit. on pp. 6, 9, 11, 12).

[Sur15] B. Suri. “Transmon qubits coupled to superconducting lumped element resonators”. PhD thesis. Digital Repository at the University of Maryland: University of Maryland, 2015 (cit. on p. 13).

[Suz91] M. Suzuki. "General theory of fractal path integrals with applications to many-body theories and statistical physics". *Journal of Mathematical Physics* 32, 400 (1991), 400 (cit. on p. 38).

[SW66] J. R. Schrieffer and P. A. Wolff. "Relation between the Anderson and Kondo Hamiltonians". *Phys. Rev.* 149 (1966), 491 (cit. on p. 51).

[TCM+16] M. Takita, A. Córcoles, E. Magesan, B. Abdo, M. Brink, A. Cross, J. M. Chow, and J. M. Gambetta. "Demonstration of weight-four parity measurements in the surface code architecture" (2016). arXiv:1605.01351 (cit. on pp. 3, 28, 66, 73).

[TK84] H. Tal-Ezer and R. Kosloff. "An accurate and efficient scheme for propagating the time dependent Schrödinger equation". *J. Chem. Phys.* 81 (1984), 3967 (cit. on p. 44).

[War15] M. Ware. "Flux-tunable superconducting transmons for quantum information processing". PhD thesis. Syracuse University, 2015 (cit. on pp. 3, 74, 78).

[Wol15] Wolfram Research, Inc. *Mathematica, Version 10.3*. Champaign, Illinois. 2015 (cit. on p. 63).

[WS06] G. Wendin and V. S. Shumeiko. "Superconducting Quantum Circuits, Qubits and Computing". *Handbook of Theoretical and Computational Nanotechnology, Vol. 3: Quantum and molecular computing, quantum simulations, pp. 1-48, M. Rieth and W. Schommers eds., American Scientific Publisher, Los Angeles* (2006) (cit. on pp. 5, 8).

[WS65] P. Wallace and M. Stavn. "Quasi-spin treatment of Josephson tunneling between superconductors". *Canadian Journal of Physics* 43 (1965), 411 (cit. on pp. 6, 91).

[WSB+04] A. Wallraff, D. I. Schuster, A. Blais, L. Frunzio, R.-. S. Huang, J. Majer, S. Kumar, S. M. Girvin, and R. J. Schoelkopf. "Strong coupling of a single photon to a superconducting qubit using circuit quantum electrodynamics". *Nature* 431 (2004), 162 (cit. on p. 27).

[YTN03] J. Q. You, J. S. Tsai, and F. Nori. "Controllable manipulation and entanglement of macroscopic quantum states in coupled charge qubits". *Phys. Rev. B* 68 (2003), 024510 (cit. on pp. 20, 61–63).

[YWY+08] T. Yamamoto, M. Watanabe, J. Q. You, Y. A. Pashkin, O. Astafiev, Y. Nakamura, F. Nori, and J. S. Tsai. "Spectroscopy of superconducting charge qubits coupled by a Josephson inductance". *Phys. Rev. B* 77 (2008), 064505 (cit. on pp. 20, 22, 47, 51, 61, 62).

[ZG00] S.-B. Zheng and G.-C. Guo. "Efficient Scheme for Two-Atom Entanglement and Quantum Information Processing in Cavity QED". *Phys. Rev. Lett.* 85 (2000), 2392 (cit. on p. 74).

Acknowledgments

First and foremost I would like to express my deepest gratitude towards Kristel Michielsen and Hans De Raedt. I really appreciate your patient guidance and your invaluable support throughout my studies. The discussions with you have always been a pleasure to me, making it very evident to realize the fundamental difference between reality as our perception of nature, and a physical theory such as quantum theory as one of our possible descriptions of it. I would also like to give special thanks to Fengping Jin for spending many an afternoon with me digging down to the very roots of both fundamental and computational issues.

Many thanks to David DiVincenzo for taking the time to acquaint me with the many different techniques in recent technology and providing me with very interesting resources. I would also like to thank Jay Gambetta and Firat Solgun from IBM for providing me with information about some of their most recent experimental setups.

One who really deserves special credit is my girlfriend Madita Nocon who has been studying and working beside me for many years. Thanks a lot for always presenting me with very distinguished views and unfailingly asking exactly the right questions to further my ideas. My deep acknowledgment also goes to my family and the family of my girlfriend who constantly inquired about my work and helped me managing my life. Specifically, I want to thank my cousin Christopher Busch from New Zealand for proofreading parts of the thesis and providing helpful comments on language issues. Last but not least, I would like to acknowledge my friends and fellow students Marco Hufnagel and Bernhard Klemt who had to endure many engaged discussions and friendly conversations that were not always related solely to science.

Eidesstattliche Versicherung

Willsch, Dennis
Name, Vorname

311069
Matrikelnummer (freiwillige Angabe)

Ich versichere hiermit an Eides Statt, dass ich die vorliegende Arbeit/Bachelorarbeit/ Masterarbeit* mit dem Titel

Simulation of quantum computer hardware based on superconducting circuits

selbständig und ohne unzulässige fremde Hilfe erbracht habe. Ich habe keine anderen als die angegebenen Quellen und Hilfsmittel benutzt. Für den Fall, dass die Arbeit zusätzlich auf einem Datenträger eingereicht wird, erkläre ich, dass die schriftliche und die elektronische Form vollständig übereinstimmen. Die Arbeit hat in gleicher oder ähnlicher Form noch keiner Prüfungsbehörde vorgelegen.

Aachen,
Ort, Datum

Unterschrift

*Nichtzutreffendes bitte streichen

Belehrung:

§ 156 StGB: Falsche Versicherung an Eides Statt

Wer vor einer zur Abnahme einer Versicherung an Eides Statt zuständigen Behörde eine solche Versicherung falsch abgibt oder unter Berufung auf eine solche Versicherung falsch aussagt, wird mit Freiheitsstrafe bis zu drei Jahren oder mit Geldstrafe bestraft.

§ 161 StGB: Fahrlässiger Falscheid; fahrlässige falsche Versicherung an Eides Statt

(1) Wenn eine der in den §§ 154 bis 156 bezeichneten Handlungen aus Fahrlässigkeit begangen worden ist, so tritt Freiheitsstrafe bis zu einem Jahr oder Geldstrafe ein.

(2) Straflosigkeit tritt ein, wenn der Täter die falsche Angabe rechtzeitig berichtigt. Die Vorschriften des § 158 Abs. 2 und 3 gelten entsprechend.

Die vorstehende Belehrung habe ich zur Kenntnis genommen:

Aachen,
Ort, Datum

Unterschrift